VIDEO-BASED NEARSHORE DEPTH INVERSION USING WDM METHOD

BY

R. W. HAMPSON, J. T. KIRBY AND J. H. MACMAHAN

RESEARCH REPORT NO. CACR-08-02
FALL 2008

CENTER FOR APPLIED COASTAL RESEARCH

Ocean Engineering Laboratory
University of Delaware
Newark, Delaware 19716

ACKNOWLEDGEMENT

This project was funded by the Delaware Sea Grant Program, Project Number SG0709 R/ETE-6 and by the Delaware Department of Natural Resources and Environmental Control (DNREC) who purchased the cameras. Also, the Sea Colony Hotel, Bethany Beach, DE who allowing us to install cameras on their roof.

TABLE OF CONTENTS

LIST OF FIGURES

LIST OF TABLES

ABSTRACT

A new remote sensing method for estimating nearshore water depths from video imagery has been developed and applied as part of an ongoing field study at Bethany Beach, Delaware. The new method applies Donelan et al's Wavelet Direction Method (WDM) to compact arrays of pixel intensity time series extracted from video images. The WDM generates a non-stationary time series of the wavenumber and wave direction at different frequencies that can be used to create frequency-wavenumber and directional spectra. The water depth is estimated at the center of each compact array by fitting the linear dispersion relation to the frequency-wavenumber spectrum. Directional spectral results show good correlation to directional spectral results obtained from a slope array located just offshore of Bethany Beach. Additionally, depth estimations from the WDM are compared to depth measurements taken with a kayak survey system at Bethany Beach. Continuous measurements of the bathymetry at Bethany Beach are needed for inputs to fluid dynamics and sediment transport models to study the morphodynamics in the nearshore zone and can be used to monitor the success of the recent beach replenishment project along the Delaware coast.

Chapter 1

INTRODUCTION

The morphodynamics of the coastal zone are controlled by fluid motions and the resulting sediment response. Of primary importance to humans are changes in the coastal zone associated with the response of morphologic features and sediments to the overlaying waves and currents (*Holman and Stanley*, 2007). Problems such as beach erosion or sedimentation of an inlet are heightened by human development along the coast and have created a need for a better understanding of the dynamic coastal zone. Continuous bathymetry measurements are essential for coastal engineers to determine appropriate responses to a variety of coastal zone management problems. Additionally, bathymetry measurements are needed by scientists as critical inputs to sediment transport models that can be used to study and predict the response of sediments to fluid motions. Since the nearshore is a highly energetic region, the bathymetry may change on time scales as short as hours due to large storms or longer than years due to continual erosion. The spatial scales of bathymetric changes range from tens to hundreds of meters with morphological features taking on very complex forms (*Wright and Short*, 1984).

Due to the varying time and spatial scales of bathymetric changes, bathymetry measurements should ideally be made at corresponding time and space scales in order to gain insight into the nearshore morphodynamics and for assimilation into models. Conventional survey techniques may be too costly and impractical to carry out on the time and space scales required. Therefore, remote sensing methods have gained popularity as alternatives for measuring the bathymetry (*Plant et al.*, 2008). Both direct and inverse remote

sensing methods exist for water depth estimation. Direct methods such as hyperspectral (*Adler-Golden et al.*, 2005), multispectral (*Lyzenga et al.*, 2006) and light detection and ranging (LIDAR) (*Irish*, 2005) have been developed that rely on water penetration from light at various wavelengths. However, these methods are often either too costly or provide insufficient spatial resolution for continuous nearshore bathmetry measurements. Inverse remote sensing methods that rely on the interactions between ocean surface dynamics and the underlying bathymetry may be applied to both radar and optical images at a lower cost than direct methods in the nearshore.

This study presents a new video-based depth inversion technique capable of estimating nearshore water depths and the directional spectrum. Historically, video-based depth inversion procedures in the nearshore have been based on depth-dependent changes in the speed of propagating waves. Previous approaches to celerity based estimation procedures as well as the outline for the present field study is given in the remainder of this chapter.

1.1 Depth Inversion Techniques Based on Depth-Dependent Wave Celerity

As wind waves propagate toward shore over decreasing water depths, their wave celerity decreases. This phenomena is apparent through the dispersion relation which relates wave celerity to water depth and wave period. Therefore, if it is possible to measure the wave celerity and wave period of shoaling waves, then the water depth can be inferred. Remote sensing methods as early as the 1940's used the dispersion relation to calculate the water depth from time-lapse images of the ocean surface taken by planes (*Williams*, 1946). At the time, the wave celerity was estimated by measuring the distance a wave had traveled during the time between images. Since then a variety of approaches have been taken to determine the wave celerity, or equivalently, wavenumber in remotely sensed images and will be reviewed in this section.

1.1.1 Spatial Lag Methods

Spatial lag methods are direct descendants of William's original method because they still, in essence, determine the spatial lag or the distance a wave has traveled between successive images. The spatial lag is typically measured through lag-correlation functions which determine the spatial offset yielding the highest correlation between two successive images (*Dalrymple et al.*, 1998). In order to utilize the linear dispersion relation, either the wave period or wavenumber must be known in addition to the spatial lag. In some cases the wavenumber is calculated as the dominant wavenumber in the wavenumber spectrum and in other cases the wave period is chosen as the peak period of the power spectrum (*Bell*, 1999).

One drawback to spatial lag methods is that the bathymetry underlying an image is non-homogeneous. Therefore, the lag-correlation must be calculated by subdividing the entire image into smaller windows. Selecting the size of the windows creates a dilemma between having high spatial resolution of celerity estimates resulting from smaller windows versus high accuracy of cross-correlation functions resulting from larger windows (*Misra et al.*, 2003). Misra et al. found that by using least squares estimation instead of cross-correlation functions to determine the spatial lag, errors in the estimation of the celerity from smaller window sizes could be reduced by two orders of magnitude. As a result it may be possible to obtain good spatial resolution and high accuracy from using least squares estimation. Few attempts have been made to compare spatial lag methods to field data but synthetic results have shown promise.

The concept of identifying local displacements and velocities in fluid motion has been well developed in laboratory flow visualization applications such as particle image velocimetry (PIV) (*Kean and Adrian*, 1992). PIV techniques are founded on the principle that the spatial offset between similar patterns in images can be determined from the maximum correlation between subsections of images. This technique has been applied to velocity measurements in the swash zone by *Holland et al.* (2001) with comparable results

to previous remote sensing measurements of the swash zone. PIV has also been applied to wave celerity measurements in the shoaling region by *DeMunda* (2006) with some success. Unfortunately, Demunda's study did not have recent bathymetry measurements to compare his results too. Therefore, the results only show qualitatively the applicability of PIV techniques to measuring the wave celerity. Demunda found the PIV technique to work well on days with even lighting and clearly visible monochromatic waves. However, the PIV results during high wave conditions were unreliable.

1.1.2 Spectral Energy Methods

Sequences of images of the sea surface can be used to determine the wavenumbers and corresponding frequencies of the waves in the image. The maximum energy in three-dimensional space-time energy spectrums can be used to select the dominant wavenumbers and frequency in the sea (*Dugan et al.*, 2000). Once the dominant wavenumbers and frequency are extracted from the image then the depth can be inferred from the linear dispersion relationship. RMS errors as low as 0.5 to 1 meters were obtained by *Dugan et al.* (2000) by applying a non-linear least squares fit between the observed space-time energy spectrum and a modeled space-time spectrum. The modeled space-time spectrum is based on the dispersion relationship and is parameterized by depth and surface current.

An advantage of this method is that wave-current dispersion affects are included. Additionally, only the water surface needs to be visible, so it can be applied to murky waters where water penetration techniques such as LIDAR can't be used. A major disadvantage of the method is that spatial homogeneity is assumed in the image or subsection of the image in which the 2-D Fourier transform is taken. Therefore, only one depth measurement can be inferred from an image resulting in very poor spatial resolution. An image could be broken into smaller subsections similarly to spatial lag methods, however the accuracy of the wavenumber spectrum is dependent on the spatial extent and resolution of the image. As a result this method is not applicable to determining complex bathymetry in the nearshore but may be useful for larger scale studies.

1.1.3 Time Delay Methods

Instead of measuring the spatial lag for a fixed change in time the time lag is measured for a fixed distance between sensors. In contrast to spatial lag methods, time delay methods utilize intensity time series from an array of pixels in the video images. The idea of using pixel intensity time series from video images to measure wave celerity was first introduced by *Lippmann and Holman* (1991). The time lag between two sensors, or in this case pixel locations, can be computed in the time domain through correlation functions. However, often the equivalent phase delay between two sensors is computed in the fourier domain through co-variance functions. For an array of sensors the co-variance matrix can be computed which contains the phase delay at discrete frequencies between all possible locations in the array. *Lippmann and Holman* (1991) used the phase delay between two sensors to determine the time lag and subsequent wave celerity. However, in the case of cross-shore and alongshore arrays the cross-shore and alongshore wavenumber can be calculated directly as the gradient in the phase of the waves (*McGregor et al.*, 1998).

One such method using cross-shore and alongshore arrays of pixel intensity time series was developed by *Stockdon and Holman* (2000). After determining the co-variance matrix for an array of sensors, variations in the co-variance matrix were isolated at a given frequency using complex empirical orthogonal functions (CEOF). The variations in the co-variance matrix contained by the first mode of the CEOF can be used to calculate the smoothed phase gradient along the array. Results from this method were promising, as an RMS error of 0.91 meters was obtained over 30 days of continues bathymetry measurement. Depth predictions at the ends of this array are not as reliable because the center of the array will dominate the first mode of the CEOF.

Improved bathymetry results have recently been achieved by *Plant et al.* (2008) by applying a non-linear inversion method to the estimation of the phase delay in arrays of sensors. The non-linear inversion method minimizes the weighted squared error between

iterations of the modeled and observed covariance matrix. A more robust solution is obtained in this method with RMS wavenumber errors ranging from 0.068 to 0.02 m^{-1} by using phase delay information at a range of frequencies instead of just the dominant frequency. One distinct advantage arise that error predictions are provided by Plant's method which are necessary for quality control. Additionally, Plant's method was found to be tolerant to noise and other sampling deficiencies.

1.2 Outline for Present Study

Presently there is a video-based remote sensing system being used in part of an ongoing field study at Bethany Beach, Delaware (Figure 1.1). This remote sensing system consists of 5 video cameras located on a building overlooking the beach 30 meters above sea level and 100 meters away from the shoreline as shown by Figures 1.2 and 1.3. The five video cameras provide a panoramic view of the nearshore coastal zone (Figure 1.4). Quantitative information about the sea surface is extracted from each video image by employing a widely accepted camera model developed by *Holland et al.* (1997) and the Argus group (*Holman and Stanley*, 2007). The camera model provides a relationship between pixel locations and real world coordinates allowing video camera images to be converted into geo-rectified images (Figure 1.5). Figure 1.6 shows an example of a geo-rectified, panoramic view of the shoreline obtained by merging together each geo-rectified camera image.

The video cameras are capable of recording a variety of images and data sets. Currently the video cameras record snapshots, timex images, variance images, video files, and pixel intensity time series (Figure 1.7). A timex image is a series of snapshots averaged over time. Similarly, variance images record the intensity variation over time. The timex and variance images shown in Figure 1.7 were taken over 1 minute. The pixel intensity time series record the variation in brightness at a single pixel in a video file over over time. The red dots in Figure 1.7 correspond to the image location where a pixel time series is recorded. All 5 cameras record snapshot, timex and variance images once every

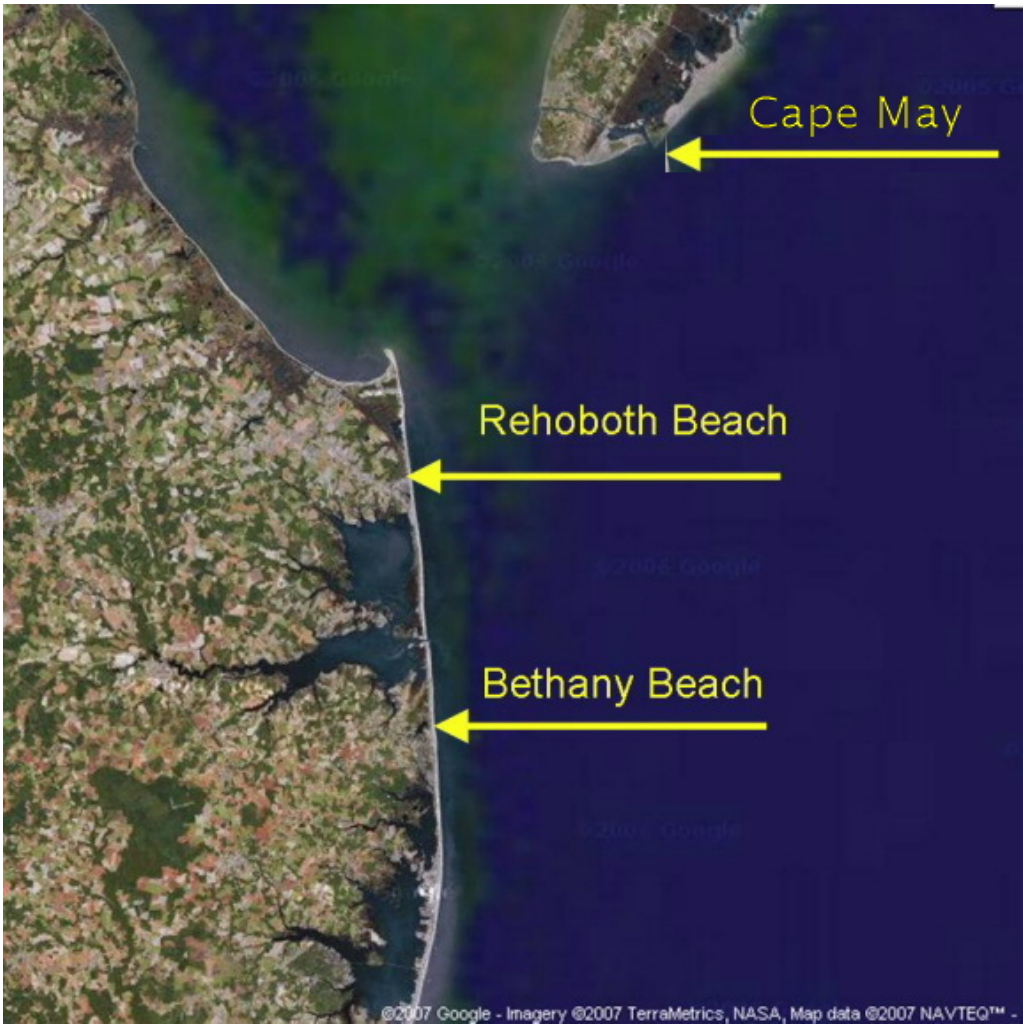

Figure 1.1: Location of Field Study at Bethany Beach, Delaware

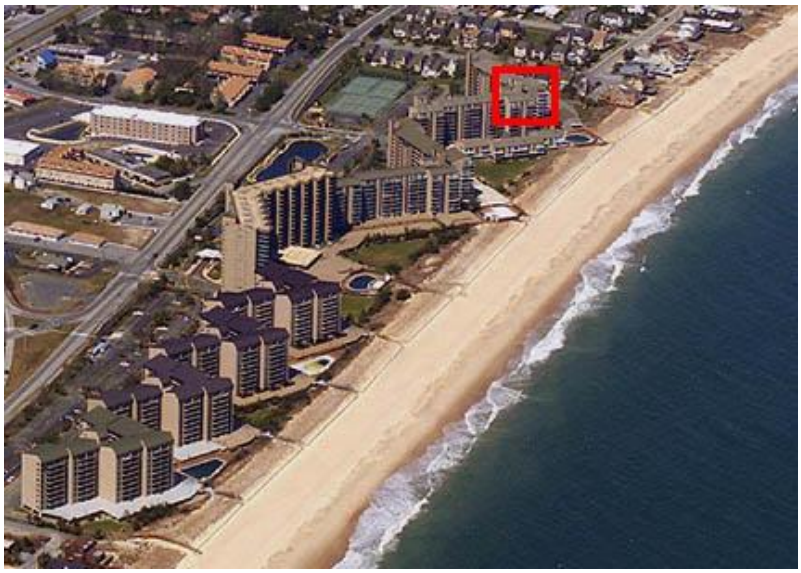

Figure 1.2: An aerial view of the Sea Colony Towers in Bethany Beach, De. The location of the video observation system is inside the red box.

Figure 1.3: Video observation system located on top of Sea Colony Towers

(a) Cam 1

(b) Cam 2

(c) Cam 3

(d) Cam 4

(e) Cam 5

Figure 1.4: View from all 5 cameras. Together the five cameras provide a panoramic view of the shoreline.

(a) Raw image

(b) Geo-rectified image

Figure 1.5: Raw video image and the corresponding geo-rectified image using the camera model developed by *Holland et al.* (1997). Taken on Nov. 9th, 2006 at 17:33:58

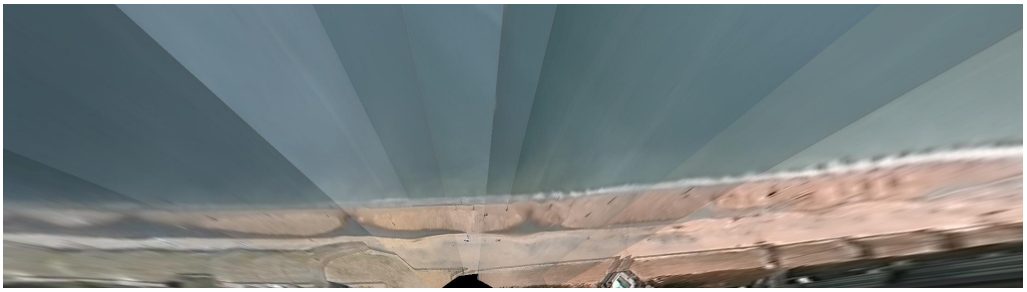

Figure 1.6: Panoramic view of the shoreline from all 5 Timex camera images.

hour. However, only camera 3 is set to record video files and pixel intensity time series. Data was collected from July 2006 to October 2008 and the system has subsequently been un-installed. During operation each of the image types were transferred to University of Delaware and subsequently shown on the Bethany Beach SANDCAM website (http://sandcam.coastal.udel.edu/beth/index.html).

As part of the ongoing study at Bethany Beach, a water depth estimation procedure that can be applied to the video cameras is required. The estimation procedure needs to be capable of providing continuous and accurate bathymetry measurements at a variety of time scales and small enough spatial scales to resolve interesting morphologic features in the nearshore. The remaining chapters provide the theoretical background for a new depth inversion technique based on the Wavelet Directional Method (WDM) (*Donelan et al.*, 1996), as well as the results from application of the new depth inversion to video-camera observation system at Bethany Beach, DE.

(a) Snapshot

(b) Timex

(c) Variance

(d) Video

(e) Pixel Intensity Time Series

Figure 1.7: The video observation system records snapshots, timex images, variance images, video files, and pixel intenisty time series hourly.

Chapter 2

INCIDENT WAVE CONDITIONS: DIRECTIONAL SPECTRUM ESTIMATORS

Of equal importance to bathymetry measurements in studying the morphodynamics in the coastal zone are incident wave conditions. For most studies it is not sufficient to describe the incident wave conditions with just a power spectrum because waves in the ocean are propagating with both a range of frequencies and directions. Therefore, a directional wave spectrum which describes the distribution of wave energy at both a range of frequencies and directions is required. In the field study at Bethany Beach there is a slope array located just offshore at nominal water depth of 10 meters and approximately 800 meters north of the video camera location (Figure 2.1).

The slope array at Bethany Beach is operated by the US Army Corps of Engineers and consists of three pressure sensors arranged in an equilateral triangle with 1.83 meter spacing (Figure 2.2). Hourly raw pressure time series, 1024 seconds long, sampled at 1 Hz, are taken by the slope array and transferred to the University of Delaware. After processing the pressure data, the incident wave conditions in the ocean can be described by the directional spectrum. Presently the hourly directional spectrum and power spectrum calculated from the slope array data are updated on the Bethany Beach SANDCAM website (http://sandcam.coastal.udel.edu/beth/index.html). The coordinate system for this study is shown in Figure 2.3, where north-south corresponds to alongshore direction and east-west corresponds to the cross-shore direction. The easting and northing datum of the coordinate system is located just in front of camera 3 on the beach. The orientation of the

Figure 2.1: Aerial view of Bethany Beach, De. The location of the slope array is shown with a red cross, and the location of the video-observation system is shown with a red box.

Bethany Beach slope array is shown in Figure 2.2. Details regarding the transformation of pressure measurements to heave, pitch and roll data is given in Section 2.6.1.

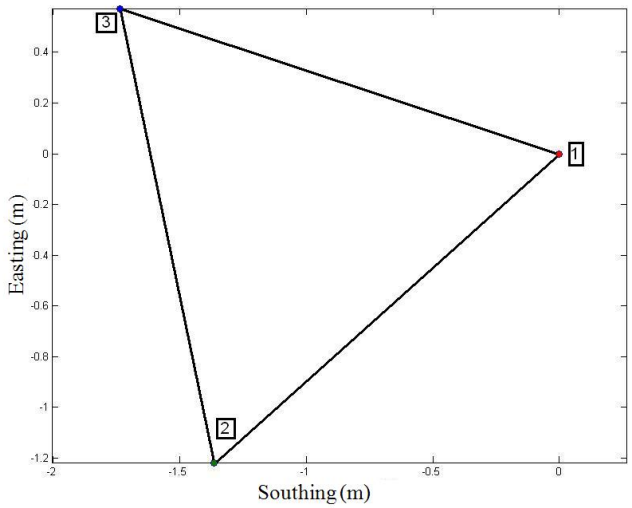

Figure 2.2: Orientation of slope array located just offshore of Bethany Beach, Delaware at a nominal depth of 10 meters

2.1 General Properties of a Random Sea State

Since the sea surface elevation $\eta(x, y, t)$ may be represented by a summation of wave components at a range of frequencies and directions as

$$\eta(x, y, t) = \sum_{n=1}^{N} \int_{0}^{2\pi} a(\omega_n, \theta) e^{i(\omega_n t - k(\omega_n)\cos(\theta)x - k(\omega_n)\sin(\theta)y)} d\theta \tag{2.1}$$

where $a(\omega, \theta)$ is the complex amplitude, ω is the radial wave frequency, θ is the wave propagation direction, and $k(\omega)$ is the wavenumber. The directional spectrum $S(\omega, \theta)$ can then be defined as

$$S(\omega, \theta) d\omega d\theta = \frac{1}{2} |a(\omega, \theta)|^2 \tag{2.2}$$

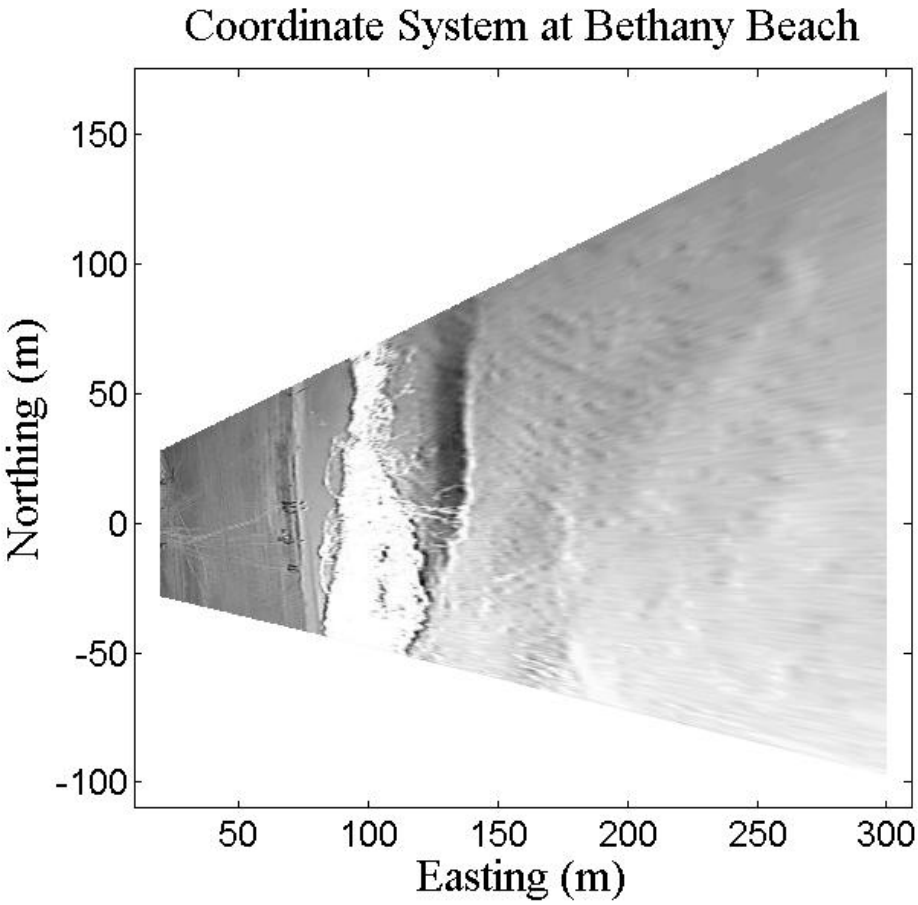

Figure 2.3: Coordinate system for study, where north-south corresponds to alongshore direction and east-west corresponds to the cross-shore direction.

Since the total energy of the waves at a given location should be the same whether it is described by a one-dimensional power spectrum or a two-dimensional directional spectrum the following condition must be satisfied

$$\int_0^{2\pi} S(\omega,\theta)d\theta = S(\omega) \tag{2.3}$$

For convenience the directional spectrum is often defined as

$$S(\omega,\theta) = S(\omega)G(\omega,\theta) \tag{2.4}$$

where $G(\omega,\theta)$ is the directional spreading function which describes how the energy of the sea surface at a given frequency is distributed among a range of directions. Applying the condition of energy conservation at given frequency yields

$$\int_0^{2\pi} G(\omega,\theta)d\theta = 1 \tag{2.5}$$

Since the 1960's, a variety of methods have been developed to estimate the directional spectrum from arrays of instruments and wave-rider buoys. This chapter will focus on three methods for determining the directional spectrum from wave-rider buoys or equivalently slope arrays. The three methods used in this study are the Direct Fourier Transform Method (DFTM) developed by *Longuet-Higgins et al.* (1962), the Maximum Likelihood Method (MLM) developed by *Capon* (1960), and the Wavelet Directional Method (WDM) developed by *Donelan et al.* (1996).

2.2 The Heave-Pitch-Roll Compact Array

The three quantities measured by the buoy or slope array are denoted η, η_x, η_y. From linear wave theory the three quantities η, η_x, η_y may be written in terms of the complex wave amplitude $a(\omega,\theta)$ as

$$\eta(t) \;=\; \sum_{n=1}^{N}\int_0^{2\pi} a(\omega_n,\theta)e^{i(\omega_n t)}d\theta \tag{2.6}$$

$$\eta_x(t) = \sum_{n=1}^{N} \int_0^{2\pi} -ik\cos(\theta)a(\omega_n,\theta)e^{i(\omega_n t)}d\theta \tag{2.7}$$

$$\eta_y(t) = \sum_{n=1}^{N} \int_0^{2\pi} -ik\sin(\theta)a(\omega_n,\theta)e^{i(\omega_n t)}d\theta \tag{2.8}$$

From the definitions of η, η_x, η_y the cross-spectrum, Φ_{ij}, can be computed for all possible combinations of the water surface measurements. The cross-spectra are labeled by the subscripts 1,2,3 which have been used to represent η, η_x, η_y respectively

$$\begin{aligned}
\Phi_{11}(\omega) &= \int_0^{2\pi} S(\omega,\theta)d\theta \\
\Phi_{12}(\omega) &= -i\int_0^{2\pi} k\cos(\theta)S(\omega,\theta)d\theta \\
\Phi_{13}(\omega) &= -i\int_0^{2\pi} k\sin(\theta)S(\omega,\theta)d\theta \\
\Phi_{21}(\omega) &= i\int_0^{2\pi} k\cos(\theta)S(\omega,\theta)d\theta \\
\Phi_{22}(\omega) &= \int_0^{2\pi} k^2\cos^2(\theta)S(\omega,\theta)d\theta \\
\Phi_{23}(\omega) &= \int_0^{2\pi} k^2\cos(\theta)\sin(\theta)S(\omega,\theta)d\theta \\
\Phi_{31}(\omega) &= i\int_0^{2\pi} k\sin(\theta)S(\omega,\theta)d\theta \\
\Phi_{32}(\omega) &= \int_0^{2\pi} k^2\cos(\theta)\sin(\theta)S(\omega,\theta)d\theta \\
\Phi_{33}(\omega) &= \int_0^{2\pi} k^2\sin^2(\theta)S(\omega,\theta)d\theta
\end{aligned} \tag{2.9}$$

It is conventional in spectral analysis to refer to the real and imaginary parts of the cross-spectra as the co-spectra, $C_{ij}(\omega)$, and quadrature-spectra, $Q_{ij}(\omega)$. The relationship between the cross-spectra and the co and quad is given by

$$\Phi_{ij}(\omega) = C_{ij}(\omega) - iQ_{ij}(\omega) \tag{2.10}$$

2.3 Direct Fourier Transform Method

Longuet-Higgins et al. (1962) developed a method for determining the directional spectrum of a sea from a heave, pitch, and roll buoy. The DFTM assumes that the directional spectrum may be expanded as a Fourier series in θ at each radial frequency.

$$S(\omega,\theta) = \frac{1}{2}A_0(\omega) + \sum_{n=1}^{\infty} A_n(\omega)\cos(n\theta) + \sum_{n=1}^{\infty} B_n(\omega)\sin(n\theta) \tag{2.11}$$

where

$$\begin{aligned} A_0(w) &= \frac{1}{\pi}\int_0^{2\pi} S(\omega,\theta)d\theta & (2.12)\\ A_n(w) &= \frac{1}{\pi}\int_0^{2\pi} S(\omega,\theta)\cos(n\theta)d\theta & (2.13)\\ B_n(w) &= \frac{1}{\pi}\int_0^{2\pi} S(\omega,\theta)\sin(n\theta)d\theta & (2.14) \end{aligned}$$

Comparing (2.12-2.14) to (2.9), it is apparent that 5 coefficients of the Fourier series can be determined as

$$\begin{aligned} A_0(\omega) &= \frac{1}{\pi}C_{11}(\omega)\\ A_1(\omega) &= \frac{1}{k\pi}Q_{12}(\omega)\\ B_1(\omega) &= \frac{1}{k\pi}Q_{13}(\omega)\\ A_2(\omega) &= \frac{1}{k^2\pi}(C_{22}(\omega) - C_{33}(\omega))\\ B_2(\omega) &= \frac{2}{k^2\pi}C_{23}(\omega) \end{aligned} \tag{2.15}$$

and the resulting directional spectrum estimate of $S(\omega,\theta)$ is

$$S_1(\omega,\theta) = \frac{1}{2}A_0(\omega) + A_1\cos(\theta) + B_1\sin(\theta) + A_2\cos(2\theta) + B_2\sin(2\theta) \tag{2.16}$$

This may be a fair approximation of the infinite series if the the higher order terms are relatively small. Since the lower order Fourier coefficients have longer wavelengths, it should be expected that the parametric method will have difficulty in matching sharp changes in the directionally spreading function and thus provide poor directional resolution. The partial sum $S_1(\omega, \theta)$ is a smoothed average of the actual directional spectrum (*Longuet-Higgins et al.*, 1962). One downfall of the partial sum $S_1(\omega, \theta)$ is that it may predict negative values for directional spectrum. Since energy is a positive quantity an alternative approximation to $S(\omega, \theta)$ is

$$S_2(\omega,\theta) = \frac{1}{2}A_0(\omega)+\frac{2}{3}(A_1(\omega)\cos(\theta)+B_1(\omega)\sin(\theta))+\frac{1}{6}(A_2(\omega)\cos(2\theta)+B_2(\omega)\sin(2\theta)) \tag{2.17}$$

$S_2(\omega, \theta)$ ensures that the estimation of $S(\omega, \theta)$ is positive, however, it is inherently smoother too. Throughout the remainder of this study the directional estimate of $S_2(\omega, \theta)$ will be used for the DFTM.

2.4 Maximum Likelihood Method

Oltman-Shay and Guza (1984) applied a data-adaptive directional spectral estimator, called the Maximum Likelihood Method (MLM), to point measurements such as the pitch-roll buoy and slope array. Oltman-Shay and Guza wanted to create a high resolution estimator for point measurements that did not rely on a priori assumptions about the shape of the directional spectrum. A similar high-resolution estimator had already been developed for spatial arrays by *Capon* (1960) and *Davis and Regier* (1977), called the Maximum Likelihood Estimator (MLE). Oltman-Shay et al extended Capon's high-resolution estimator to point measurements of η, η_x, and η_y. A rigorous derivation can also be found in *Isobe et al.* (1984).

Similarly to the DFTM estimator, the MLM estimator relies on the cross-spectrum to compute the directional spectrum. However, Capon's method is an estimate of the

most likely complex amplitude, $\tilde{a}(\omega, \theta)$, of a single plane wave embedded in noise. For a point array system the complex amplitude estimate is a linear combination of the Fourier coefficients of η, η_x, η_y (denoted by F_1,F_2,F_3) given by

$$\tilde{a}(\omega, \theta) = \sum_{n=1}^{3} w_n(\omega, \theta) F_n(\omega) \tag{2.18}$$

where $w_n(\omega, \theta)$ are complex weighting functions. Therefore, a variance or spectral estimate would be given by

$$\tilde{S}(\theta) = \tilde{a}(\theta)\tilde{a}^*(\theta) \tag{2.19}$$

$$\tilde{S}(\theta) = \sum_{n=1}^{3}\sum_{m=1}^{3} w_n(\theta) w_m^*(\theta) F_n F_m^* \tag{2.20}$$

$$\tilde{S}(\theta) = \sum_{n=1}^{3}\sum_{m=1}^{3} w_n(\theta) w_m^*(\theta) \Phi_{nm} \tag{2.21}$$

where the frequency dependence has been dropped. Theoretically the cross-spectra matrix Φ_{nm} has the form of

$$\Phi_{ij} = \int_0^{2\pi} S(\alpha) G_i G_j^* d\alpha \tag{2.22}$$

where

$$G_1 = 1, G_2 = ik\cos\alpha, G_3 = ik\sin\alpha \tag{2.23}$$

The wavenumber, k, may be calculated for given frequency directly from the cross-spectra by

$$k(\omega) = \frac{g}{\omega^2}\left(\frac{C_{22} + C_{33}}{C_{11}}\right)^{\frac{1}{2}} \tag{2.24}$$

In the MLM estimator it is assumed the wave spectrum consists of a plane wave of variance $S(\alpha)$ embedded in noise $S_N(\alpha)$. The wave spectrum can be written as

$$S(\alpha) = \delta(\alpha - \theta)S(\theta) + S_N(\alpha) \tag{2.25}$$

where $\delta(\alpha - \theta)$ is equal to one at zero and zero at all other values. If this assumed wave spectrum form is inserted into the cross-spectral matrix, then the variance estimate can be given as

$$\tilde{S}(\theta) = S(\theta)W(\theta, \theta) + \int_0^{2\pi} W(\theta, \alpha)S_N(\alpha)d\alpha \tag{2.26}$$

where $W(\theta, \alpha)$ can be thought of as a window function. The window function is given by

$$W(\theta, \alpha) = \sum_{n=1}^{3} \sum_{m=1}^{3} w_n(\theta)w_m^*(\theta)G_n(\alpha)G_m(\alpha) \tag{2.27}$$

It is clear from looking at the variance estimate that if there is no noise, $S_N = 0$, then the estimate is an exact estimate of the variance if $W(\theta, \theta)$ is equal to 1. Therefore, this estimator requires that $W(\theta, \theta)$ be equal to 1. This constraint makes this estimator a maximum likelihood estimate. It can also be seen from the variance estimate that minimizing the convolution of $W(\theta, \alpha)$ and $S_N(\alpha)$ minimizes the error in the estimate. Since $S(\theta)$, $W(\theta, \alpha)$, and $S_N(\alpha)$ are all positive values minimizing the convolution is the same as minimizing the variance estimate, $\tilde{S}(\theta)$, itself. Solving the minimization problem subject to the maximum likelihood constraint yields the final result for the estimator

$$\tilde{S}(\theta) = \{\sum_{n=1}^{3} \sum_{m=1}^{3} \Phi_{nm}^{-1} G_m(\theta)G_n^*(\theta)\}^{-1} \tag{2.28}$$

where Φ_{nm}^{-1} is the inverse of the 3 x 3 cross-spectral matrix at a given frequency. It should be noted that this maximum likelihood estimate is performed at each frequency, and yields the directional spreading of the energy for each individual frequency in the power spectrum. In applications it was found that the MLM is sensitive to errors in the cross-spectra resulting from noisy signals. Therefore, it was necessary to create numerical stability by smoothing the spectral estimates using Welch's method.

2.5 Wavelet Directional Method

The Wavelet Directional Method (WDM) was developed by *Donelan et al.* (1996) as an alternative to conventional directional spectral analysis methods. Conventional methods such as the DFTM and MLM calculate a directional spectrum from the phase differences contained within the cross-spectra between sensors. The cross-spectra between two sensors essentially contains the time-averaged phase lag between two sensors. However, the WDM utilizes wavelets to compute the phase lag at each time in the data series. Therefore, the WDM yields time and frequency localized estimates of the wavenumber and wave direction. The time localization provided in the WDM makes it a powerful tool for analyzing non-stationary data where conventional spectral methods have had trouble.

The first step in the WDM is to compute the wavelet transform, $W_j(v_0, \tau)$ of the water surface elevation time series, $\eta(t)$, at each location, in the compact array. The wavelet transform of $\eta(t)$ is given as

$$W(v_0, \tau) = \int_t^{t+T} \eta(t)\psi^*(t - \tau, v_0)dt \tag{2.29}$$

where v_0 is the scale frequency of the wavelet, τ is time shift of the wavelet, and ψ is the wavelet. For this study the Morlet wavelet (Figure 2.4) was selected because it provides a good balance between frequency and time localization. The Morlet wavelet is given by (following *Krogstad et al.* (2006))

$$\psi(t - \tau, v_0) = \frac{\sqrt{2\pi|v_0|}}{\pi^{\frac{1}{4}}\sqrt{\sigma_0}} e^{[i2\pi v_0(t-\tau)]} e^{[-\frac{(2\pi v_0(t-\tau))^2}{2\sigma_0^2}]} \tag{2.30}$$

where σ_0 controls how quickly the wavelet decays. Details regarding the wavelet transform and analyzing wavelet are provided in Appendix A.3. In practice it is faster to compute the Wavelet transform in Fourier space, therefore, in this study the Wavelet transform was computed as

$$W(v_0, \tau) = \int \hat{\eta}(\omega)\hat{\psi}^*(\omega, v_0)e^{iw\tau}d\omega \tag{2.31}$$

where Morlet wavelet is given by

$$\hat{\psi}(\omega, v_0) = \frac{1}{\pi^{\frac{1}{4}}} \sqrt{\frac{\sigma_0}{|v_0|}} e^{[-\frac{\sigma_0^2}{|v_0|} \frac{(\frac{\omega}{2\pi} - v_0)^2}{2}]} \tag{2.32}$$

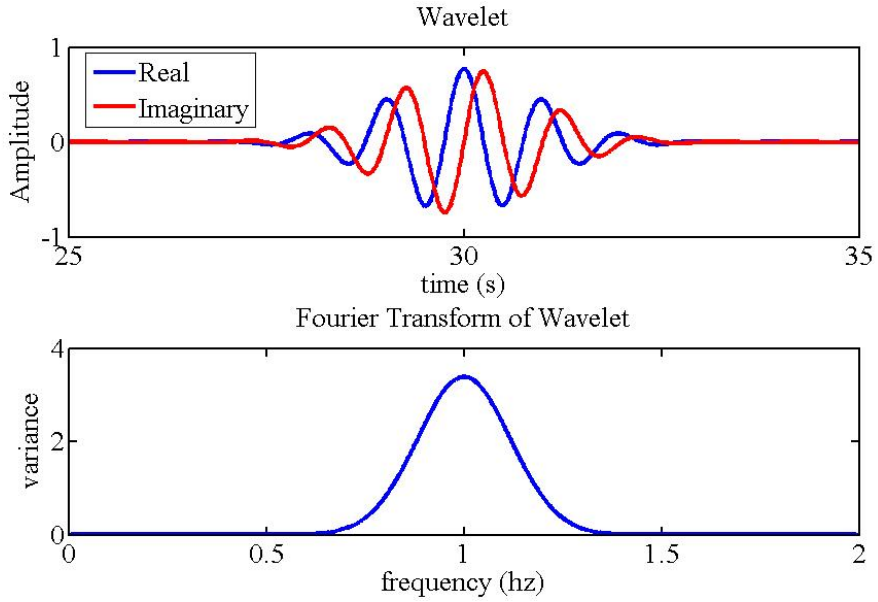

Figure 2.4: Morlet Wavelet and its Fourier transform

Taking the wavelet transform of the water surface elevation breaks down the signal into energy and phase information at a range of scale frequencies, v_0, and times, τ. The wavelet transform can be thought of as a filtered wave signal such that that at a given scale frequency the wavelet transform only contains the components of the sea surface corresponding to that scale frequency. However, the frequency localization is reduced in the wavelet transform at the expense of providing time localization. Therefore, the apparent filtered wave signal contains some energy from adjacent frequencies as well. This effect will be described later in an application of the WDM to the slope array.

The phase of the wavelet transform or filtered wave signal can be calculated directly from the real and imaginary parts of the wavelet transform. The real part of the

wavelet transform contains the even components of the wave signal and the imaginary part of the wavelet transform contains the odd components of the wave signal. The phase ϵ of the wavelet transform at a given scale frequency and time is computed as

$$\epsilon = \tan^{-1}\left(\frac{-Im(W)}{Re(W)}\right) \tag{2.33}$$

where the time and scale frequency dependence has been dropped. The phase shift,$\Delta\epsilon_{mn}$, between two sensors, m and n, can be determined from the phase of the wavelet transform as

$$\Delta\epsilon_{mn} = \epsilon_m - \epsilon_n \tag{2.34}$$

If the wavelets are assumed to propagate in the same manner as plane waves, the value of the wavelet coefficients at two spatially separated locations, x_m and x_n, is related by

$$W_m(v_0, \tau)e^{-i\mathbf{k}\cdot\mathbf{x}_m} = W_n(v_0, \tau)e^{-i\mathbf{k}\cdot\mathbf{x}_n} \tag{2.35}$$

where

$$\mathbf{k} = k_x\mathbf{i}_x + k_y\mathbf{i}_y \tag{2.36}$$

such that $\mathbf{k}$ is the unknown wavenumber vector of the propagating wavelet. Now at any pair of locations an equation relating the phase difference to the wavenumber can be written as

$$\Delta\epsilon_{mn} = \mathbf{k}\cdot\mathbf{x}_m - \mathbf{k}\cdot\mathbf{x}_n \tag{2.37}$$

Since the phase difference equation has two unknowns, k_x and k_y, only two equations are needed to solve for k_x and k_y. For an array of N sensors an equation exist for each unique pair of sensors, such that a set of R equations is generated where

$$R = \frac{N!}{(N-2)!2!} \tag{2.38}$$

The set of independent equations for an array of sensors is

$$\Delta\epsilon_{mn} = k_x(x_m - x_n) + k_y(y_m - y_n);\ m, n = 1\ldots,\ N \tag{2.39}$$

For a set of independent equations a least square solution for $\mathbf{k}$ is given by

$$\mathbf{k}^{LS} = (X^T X)^{-1}(X^T \Delta\Phi) \tag{2.40}$$

where

$$X = \begin{bmatrix} \Delta x_{12} & \Delta y_{12} \\ \Delta x_{13} & \Delta y_{13} \\ \vdots & \vdots \\ \Delta x_{mn} & \Delta y_{mn} \end{bmatrix} \tag{2.41}$$

$$\Delta\Phi = \begin{bmatrix} \Delta\epsilon_{12} \\ \Delta\epsilon_{13} \\ \vdots \\ \Delta\epsilon_{mn} \end{bmatrix} \tag{2.42}$$

After solving the set of independent equations a least squares solution for k_x and k_y is obtained. The set of independent equations is generated at each time and at each scale frequency. Therefore, at a given scale frequency and at each time there is one value obtained for the wavenumber vector yielding non-stationary time series of k_x and k_y. Calculation of the wavenumber, k, and wave direction, θ, is straight forward and given by

$$k^{LS} = \sqrt{k_x^2 + k_y^2} \tag{2.43}$$

$$\theta^{LS} = \tan^{-1}\frac{k_y}{k_x} \tag{2.44}$$

Directional spectrum plots are made by binning together the least squares estimates of the wave direction into histograms for each scale frequency. Similarly, frequency-wavenumber plots can be obtained by binning together the least squares estimate of the wavenumber at each scale frequency. In both cases more accurate spectral plots can be obtained by weighting each wavenumber or wave direction estimate by the modulus of the wavelet transform. This allows for the wavenumber and wave direction estimates to be weighted more when there are higher amounts of energy at the scale frequency corresponding to a stronger presence of waves at the scale frequency passing through the array.

2.6 Application to Bethany Beach Slope Array

An application of each of the three directional spectral estimators to the Bethany Beach slope array on September 7th, 2008, 15:00 GMT is given in this section to highlight the similarities and differences between the DFTM, MLM and WDM directional estimators. The sea surface conditions during this example consisted of fairly clean long period waves as shown in Figure 2.5. The power spectrum, Figure 2.6 generated by the slope array shows that the peak frequency of the waves is about 0.14 Hz, with a second peak in wave energy at f = 0.8 Hz.

2.6.1 Converting Slope Array Pressure Data to Heave, Pitch and Roll Data

The slope array at Bethany Beach consists of three bottom mounted pressure sensors arranged in an equilateral triangle (Figure 2.2). Slope arrays are commonly used in field and lab experiments to determine the directional spectrum and alongshore radiation stresses. Slope arrays may be advantageous to instruments that directly measure the surface elevation because they can be placed at the bottom of the ocean where they are not exposed to the harsh wave environment. Before the slope array can be used to determine the directional spectrum, the pressure data at each sensor must be converted to heave, pitch and roll data. The first step in obtaining the surface elevation, η, and surface slope

Figure 2.5: Wave conditions at Bethany Beach on September 7th, 2008, approximately 15:00 GMT

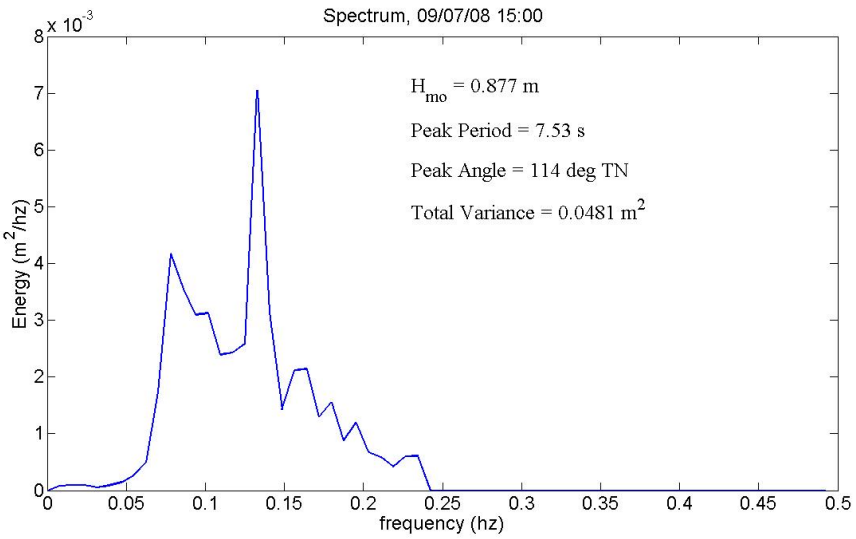

Figure 2.6: Power Spectrum obtained from slope array on September 7th, 2008, 15:00 GMT. The frequency resolution is 0.004 Hz with 16 degrees of freedom.

measurements, η_x and η_y, is to convert the pressure readings at each sensor to the surface elevation.

The transformation from a pressure time series to a surface elevation time series is obtained by applying linear wave theory and the unsteady Bernoulli equation (*Dean and Dalrymple*, 1991). The unsteady Bernoulli equation provides a relationship between the surface elevation and pressure

$$p = -\rho g z + \rho g K_p \eta \tag{2.45}$$

where p is the total pressure, ρ is the density of water, z is the elevation of the pressure sensor, g is the acceleration of gravity, η is the surface elevation, and K_p is the pressure response factor.

The transformation from a pressure time series to a water surfacec elevation time series is calculated in Fourier space because the pressure response factor is frequency dependent. The surface elevation, written in Fourier space is given by

$$\eta(t) = \sum_{n=1}^{N} F_\eta(n) e^{-i\omega_n t} \tag{2.46}$$

where $F_\eta(n)$ is the truncated Fourier series, ω_n is the angular frequency, and $k(\omega_n)$ is the wave number. The pressure response factor is given by

$$K_p(n) = \frac{\cosh(k_n d)}{\cosh(k_n h)} \tag{2.47}$$

where h is the water depth, and d is the depth of the sensor. If the hydrostatic pressure is removed from the pressure time series, and normalized by the density of water and gravity then the dynamic pressure, $\tilde{p}$, may be written as

$$\frac{\tilde{p}}{\rho g} = \sum_{n=1}^{N} K_p(n) F_\eta(n) e^{-i\omega_n t} \tag{2.48}$$

where $\tilde{p}/\rho g$ has units of length. Now the truncated Fourier series of the surface elevation may be written in terms of the Fourier transform of the normalized dynamic pressure signal, $F_{\tilde{p}}(n)$, and the pressure response factor by

$$F_\eta(n) = \frac{1}{K_p(n)} F_{\tilde{p}}(n) \tag{2.49}$$

The surface elevation time series, $\eta(t)$, can be recovered by taking the inverse Fourier Transform of $F_\eta(n)$

$$\eta(t) = \sum_{n=1}^{N} F_\eta(n) e^{-i\omega_n t} \tag{2.50}$$

This transformation allows for the surface elevation to be determined from a pressure signal. However, as kh becomes very large, K_p becomes very small and therefore any noise in the pressure signal will generate an apparent large surface signal at high frequencies. Therefore a cut-off frequency must be determined for each instrument, in which all contributions from the pressure spectrum above a certain frequency are ignored in computing the surface elevation. The cutoff frequency for this study is 0.25 hz. A sample of the

pressure to elevation transformation from one of the bottom mounted pressure sensors on the slope array data from September 7th, 2008, 15:00 GMT is shown in Figure 2.7. It is clear in Figure 2.7 that the dynamic pressure and water surface elevation are in phase as expected.

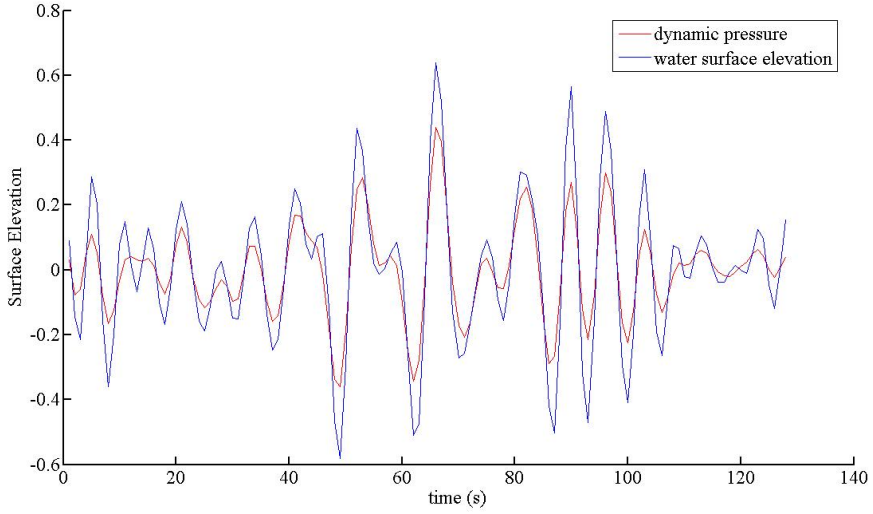

Figure 2.7: Pressure to elevation transformation from bottom mounted pressure sensor on Bethany Beach slope array from September 7th, 2008, 15:00 GMT

Obtaining η, η_x, and η_y at the center of a slope array is accomplished by fitting a plane to the three transformed elevation signals at each time, t (*Oltman-Shay and Guza*, 1984). The fitted plane can be thought of as a linear approximation of the sea surface directly above the slope array. The equation for a plane is given by

$$z = ax + by + c \tag{2.51}$$

where x and y are the alongshore and cross-shore spatial coordinates, z is the water surface elevation (η), and a is η_x, b is η_y, c is a constant. Each of the 3 pressure sensors in the array yield one equation and then the three equations can be solved using Cramer's Rule for the three unknowns (η_x , η_y, c)

$$\eta_1 = \eta_x x_1 + \eta_y y_1 + c$$

$$\eta_2 = \eta_x x_2 + \eta_y y_2 + c$$

$$\eta_3 = \eta_x x_3 + \eta_y y_3 + c \tag{2.52}$$

The set of linear equations is solved at each time step for (η_x, η_y, c). Figure 2.8 shows the resulting time series for η, η_x, and η_y and the center of the slope array on September 7th, 2008, 15:00 GMT.

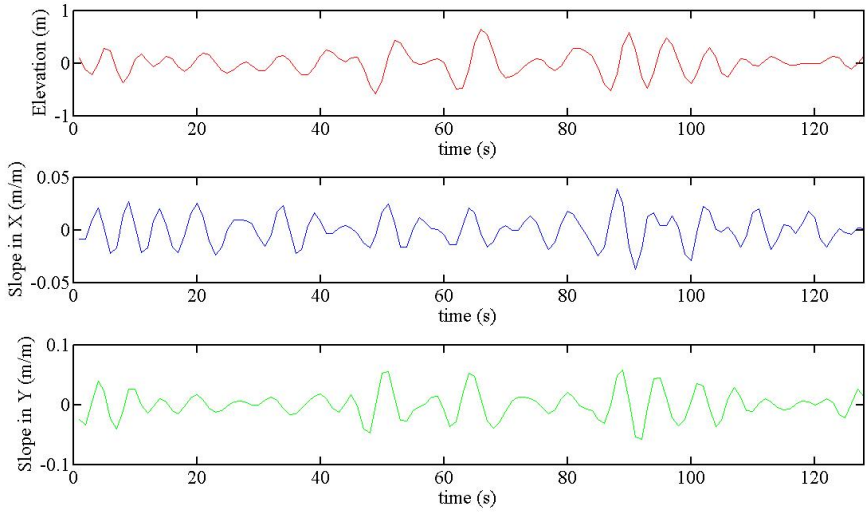

Figure 2.8: Time series results of η, η_x, and η_y from fitting a sea surface to the slope array data from slope array on September 7th, 2008, 15:00 GMT

2.6.2 DFTM and MLM Application Results

The first step in both the DFTM and MLM is to determine the cross-spectral matrix, $\Phi_{mn}(\omega)$, which contains the energy and phase information of the water surface at different frequencies. The power spectrum, obtained from the co-spectra of η ($C_{11}(\omega)$), shows the variance associated with waves at different frequencies in the ocean. Figure 2.6

shows the power spectrum at the slope array for September 7th, 2008, 15:00 GMT. Clearly the dominant wave frequency for this date is approximately equal to 0.14 Hz. However, there is also significant energy at about 0.08 Hz.

The cross-spectral results from the slope array on September 7th, 2008, 15:00 GMT, can be seen in Figure 2.9. Notice that the co-spectra ($C_{11}(\omega), C_{22}(\omega), C_{33}(\omega)$) for η, η_x, and η_y are all purely real, because each time series is perfectly in phase with itself. It is also clear that the spikes in each of the cross-spectral distributions occur at the same frequencies. However, the co-spectra and cross-spectra ($C_{22}(\omega), C_{33}(\omega), C_{23}(\omega)$) of η_x and η_y contain relatively more energy at higher frequencies than C_{11}. This result occurs because higher-frequency waves are shorter and therefore have larger slopes than the longer, low-frequency waves.

It is often a good idea to check whether or not the frequency wavenumber distribution generated by the sea surface approximations is in agreement with linear wave theory. The frequency wavenumber distribution can be computed from the cross-spectra as shown by equation 2.24. Figure 2.10 shows that the wavenumber distribution is indeed in good agreement with the linear dispersion relation. The wavenumbers calculated using equation 2.24 are the average wavenumbers at each frequency, and differ from the instantaneous wavenumbers calculated using the WDM. It was found that in instances when the MLM directional spectrum estimates were unstable the wavenumber distribution would have a great deal of scatter about the linear dispersion relation. It is not pratical to apply the MLM and DFTM to obtain the wavenumber distribution from video images because the relationship between the water surface elevation and slope is essential for accurate wavenumber estimations. Unfortunately, this relationship is not as coherent for the intensity time series as for pressure gage readings.

The directional spectrum results obtained from both the DFTM and MLM are in good agreement with each other. It can be seen in Figure 2.11 that the both the DFTM and MLM predict the dominant wave direction to be 110 degrees relative to true north.

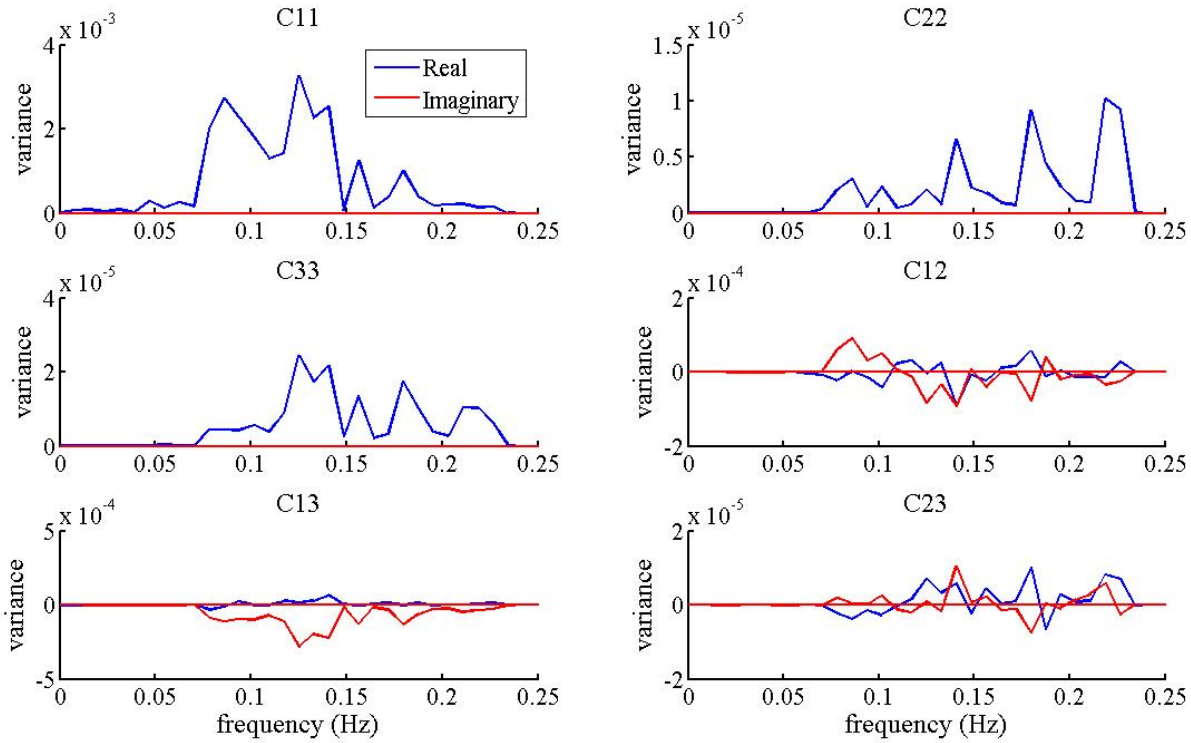

Figure 2.9: Cross-Spectra obtained from slope array on September 7th, 2008, 15:00 GMT

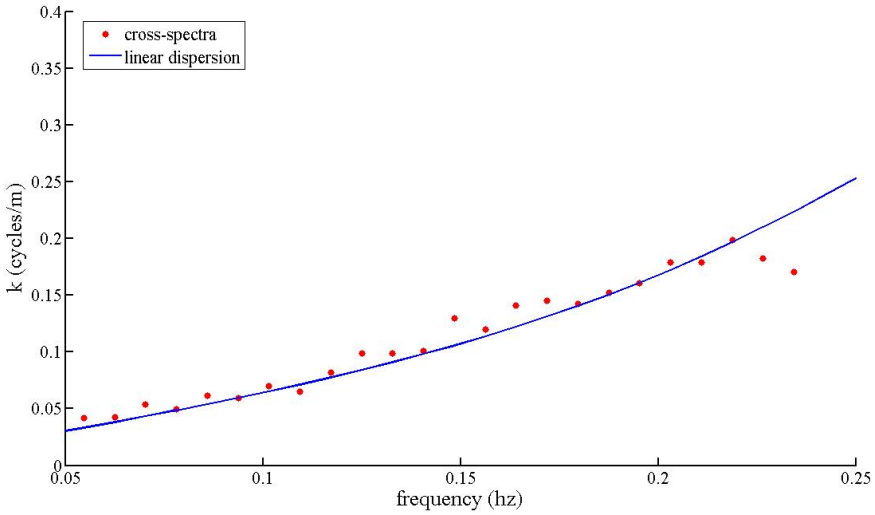

Figure 2.10: Comparison between the wavenumber, k, calculated directly from the cross-spectra using equation 2.24 and the wavenumbers calculated from linear wave theory. Results from September 7th, 2008, 15:00 GMT

However, the MLM provides significantly better directional resolution than the DFTM method which appears to have smeared the directional spreading estimate to a wider range of wave directions than the MLM. This result is better seen in Figure 2.12 where the direction spreading for both the DFTM and MLM are plotted at the dominant frequency. The MLM has been shown in previous studies by *Brissette and Tsanis* (1994) and *Isobe et al.* (1984) to provide better directional resolution than the DFTM.

2.6.3 WDM Application Results

The best way to provide insight into how the WDM works is to show what is happening at various steps throughout the WDM procedure. Therefore, an example of the application of the WDM to the slope array on September 7th, 2008, 15:00 GMT is given here. An important difference between the WDM and the DFTM and MLM is that the WDM operates at each time for the entire elevation time series, whereas the DFTM

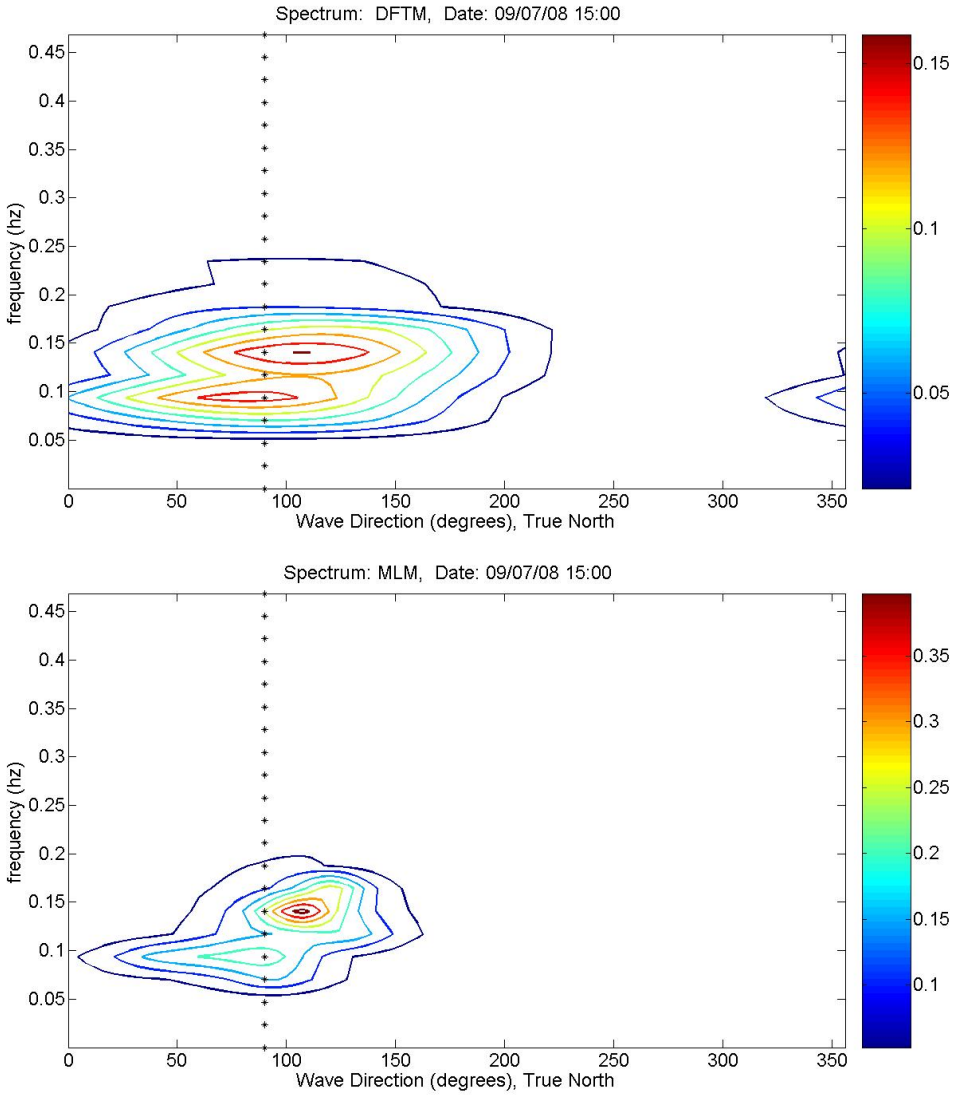

Figure 2.11: Directional spectrum at slope array using the DFTM and MLM on September 7th, 2008, 15:00 GMT

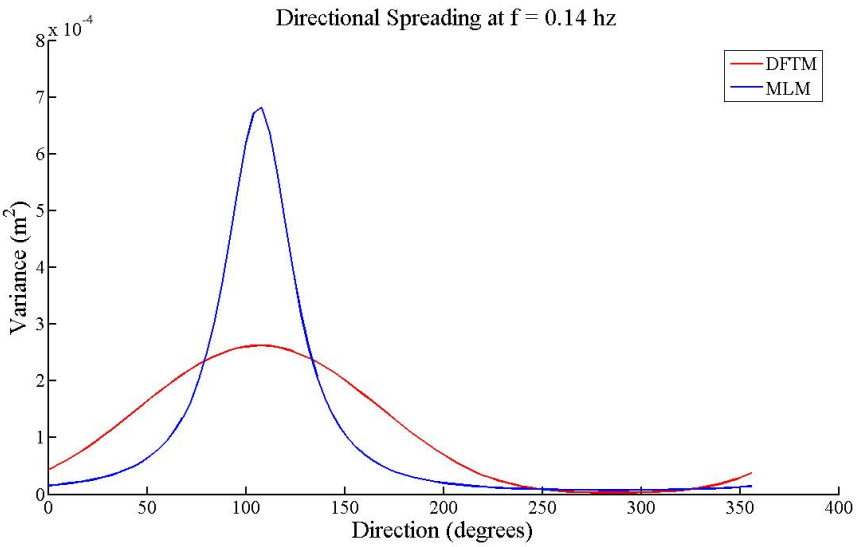

Figure 2.12: Directional spreading of DFTM and MLM estimates at the peak frequency, $f = 0.14Hz$, on September 7th, 2008, 15:00 GMT

and MLM operate on the cross-spectral matrices which are in essence a time averaged estimate of the phase lags between the sensors. Unlike the DFTM and MLM, numerical stability can not be increased by smoothing the Fourier transforms of the elevation time series such as Welch's method. This would result in a loss of all time localized phase information.

Even though the WDM operates on the entire elevation time series, only a subsection of the time series 100 seconds long will be shown here so that the details of the WDM can be discussed. The elevation time series, real part of wavelet transform, and modulus of the wavelet transform at sensor 2 of the slope array are shown in Figure 2.13. It is clear from the wavelet transform that the sea surface seems to be dominated by two distinct wave frequencies of 0.8 Hz and .14 Hz. The higher frequency wave can be seen to be propagating in the elevation time series from 0-20 seconds. However, from 40-70 seconds it appears that a lower frequency wave is propagating past the slope array. While it is hard to visibly discern this variation from looking at the elevation time series, it is clear

in the wavelet transform and modulus that at different times, waves of various frequencies are dominating the time series.

A wavelet power spectrum, $S_w(v_0)$, can be obtained by taking the time average of the modulus of the wavelet transform at each scale frequency

$$S_w(v_0) = \frac{1}{T}\sum_{\tau=0}^{T} W(v_0,\tau)W^*(v_0,\tau)d\tau \tag{2.53}$$

where T is the length of the time series. When the wavelet power spectrum is plotted on top of the Fourier power spectrum, Figure 2.14, the loss of frequency resolution in the wavelet analysis is clearly seen. The wavelet transform spectrum is in essence a smoothed version of the Fourier power spectrum.

The basis of the WDM is that the wavenumber and wave direction are calculated from the phase information contained within the wavelet transform at a given frequency and time. Therefore, in order to highlight the important steps in obtaining the wavenumber and wave direction estimates, the WDM procedure is shown at a single frequency, $f = 0.14Hz$, which is the dominant frequency. The wavelet transform contains both real and imaginary parts, which can be used to determine the phase of the wavelet transform or filtered wave. Figure 2.15 shows the real and imaginary parts of the wavelet transform for sensors 2 and 3 as well as their resulting phase time series. Sensors 2 and 3 in the slope array are oriented so that they are cross-shore from each other and are primarily measuring the cross-shore wavenumber k_x. Its clear in the phase lag plot in Figure 2.15 that there is a slowly varying phase lag between sensors 2 and 3. The phase lag is very small because sensors 2 and 3 are only 2 meters apart, and the wavelength of waves at the scale frequency of 0.14 Hz should be approximately 80 meters.

The relatively constant phase lag means intuitively that the wavenumber and wave direction estimates should also be steady. Indeed this is the case as Figure 2.15 shows the resulting wavenumber and wave direction time series estimates. Once again the wavenumber and wave direction time series have a slow drift present. The fluctuations in

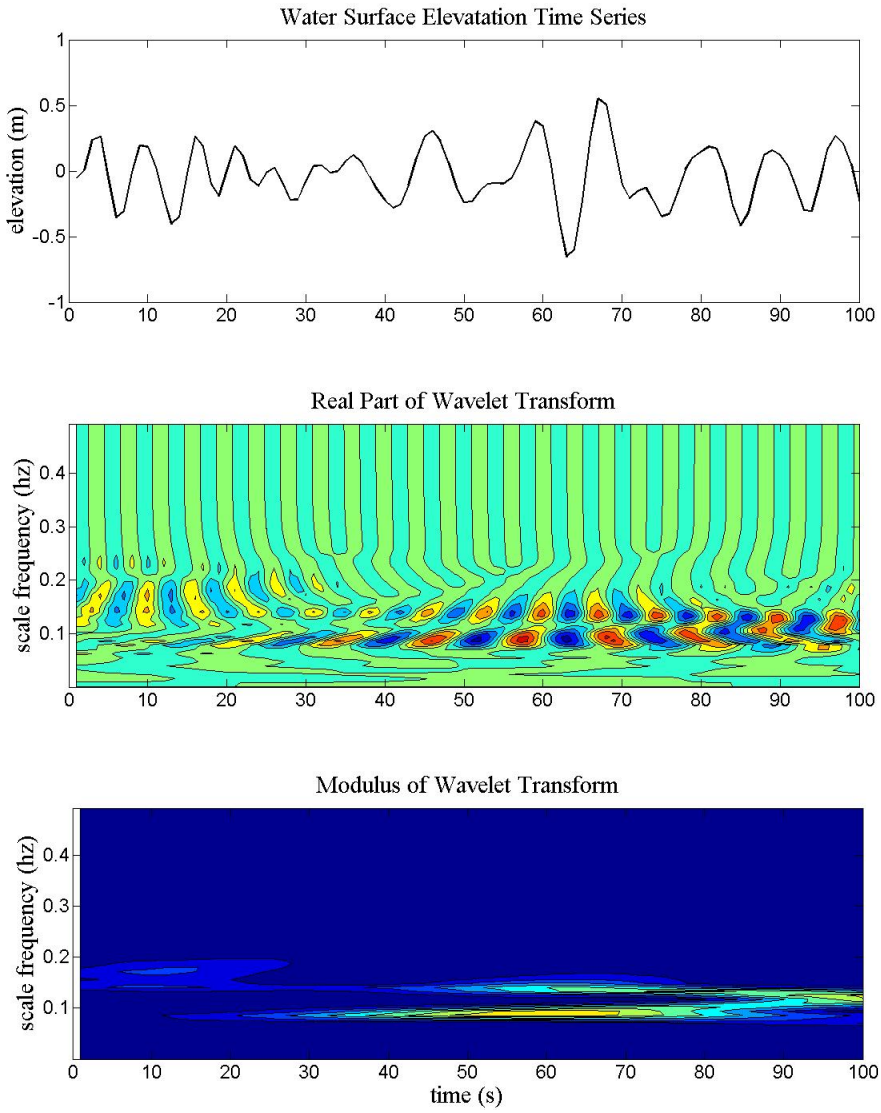

Figure 2.13: Surface elevation and its wavelet transform for WDM example. The wavelet transform and the modulus of the wavelet transform show the non-stationarity of the time signal. September 7th, 2008, 15:00 GMT.

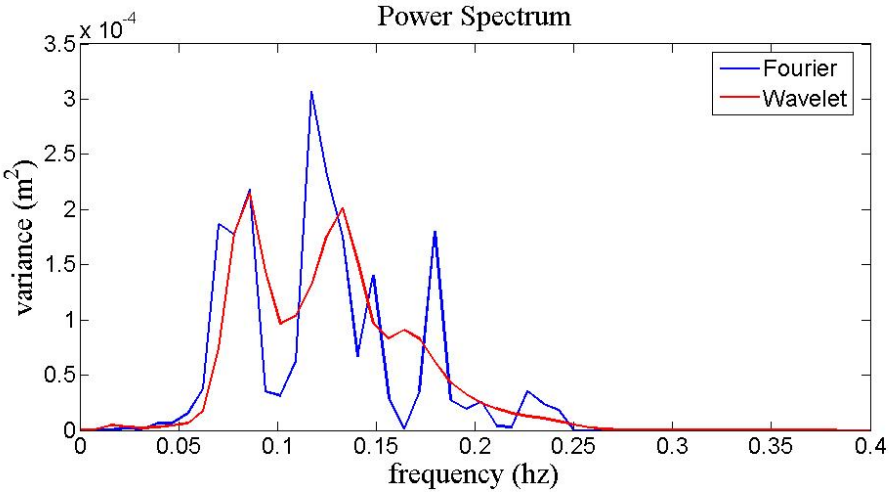

Figure 2.14: Comparison of the power spectrum and wavelet transform spectrum from September 7th, 2008, 15:00 GMT.

the phase lag and wavenumber are related to the frequency leakage inherent in the wavelet transform. The bottom panel of Figure 2.15 shows the phase gradient at sensor 3, where the phase gradient measures the frequency of the filtered waves. It is apparent in the phase gradient that the frequency of the wavelet transform is changing, and is not always equal to the scale frequency of the wavelet transform. This corresponds to waves at slightly higher or lower frequencies being picked up by the wavelet transform as a result of the imperfect frequency resolution. As a result, the wavenumber and wave direction estimates fluctuate according to the actual frequency of the waves contained in the wavelet transform.

The directional spectral estimate for the WDM obtained by binning together the variance-weighted wavenumber and wave direction time series at each scale frequency correspond well with the MLM and DFTM spectrums (Figures 2.16 and 2.11). The WDM spectrum predicts the same dominent frequencies and directions, however, the WDM appears to have finer resolution in wave direction. The increase in directional resolution can be more clearly seen in the directional spreading shown at various frequencies in

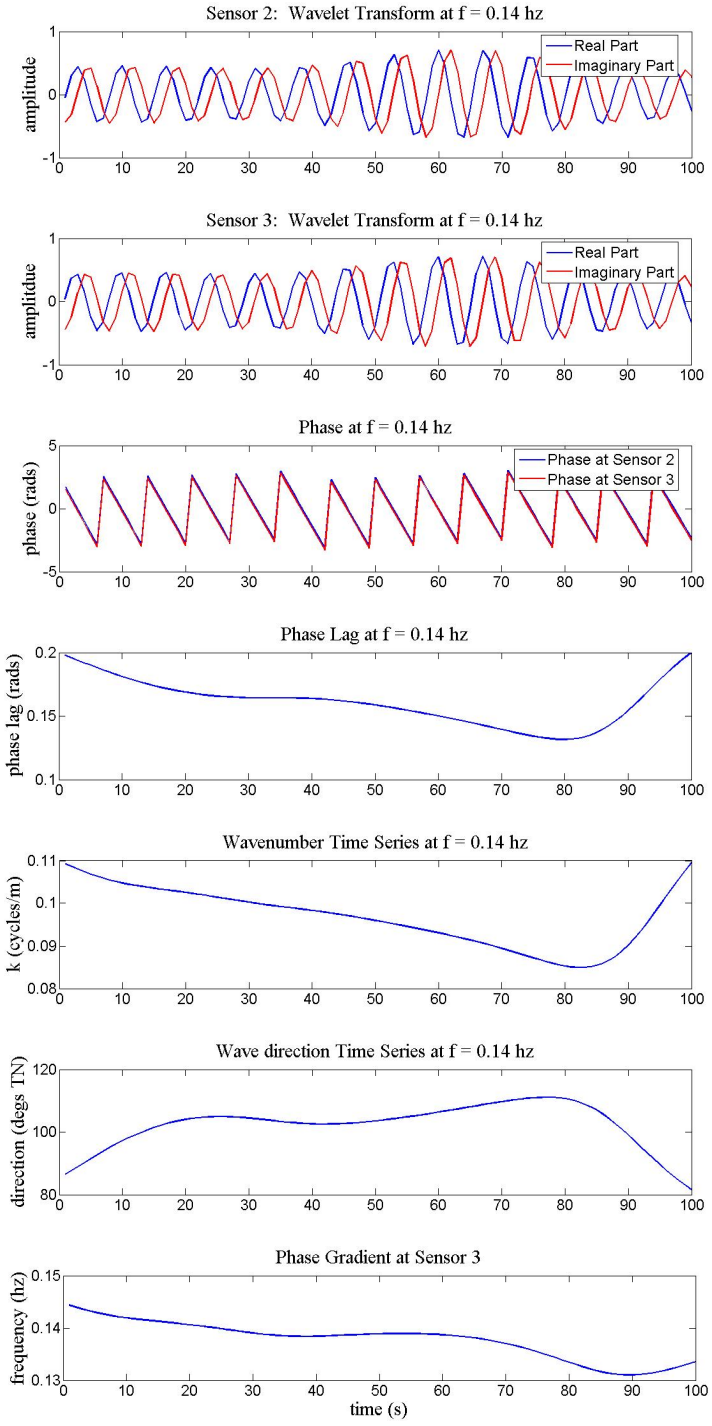

Figure 2.15: Application of WDM to slope array. Results are from September 7th, 2008, 15:00 GMT.

Figure 2.17. Additionally, the frequency-wavenumber spectrum computed for the WDM agrees well with linear wave theory, where the linear dispersion curve for the known water depth at the slope array is plotted on top of the spectrum (Figure 2.16).

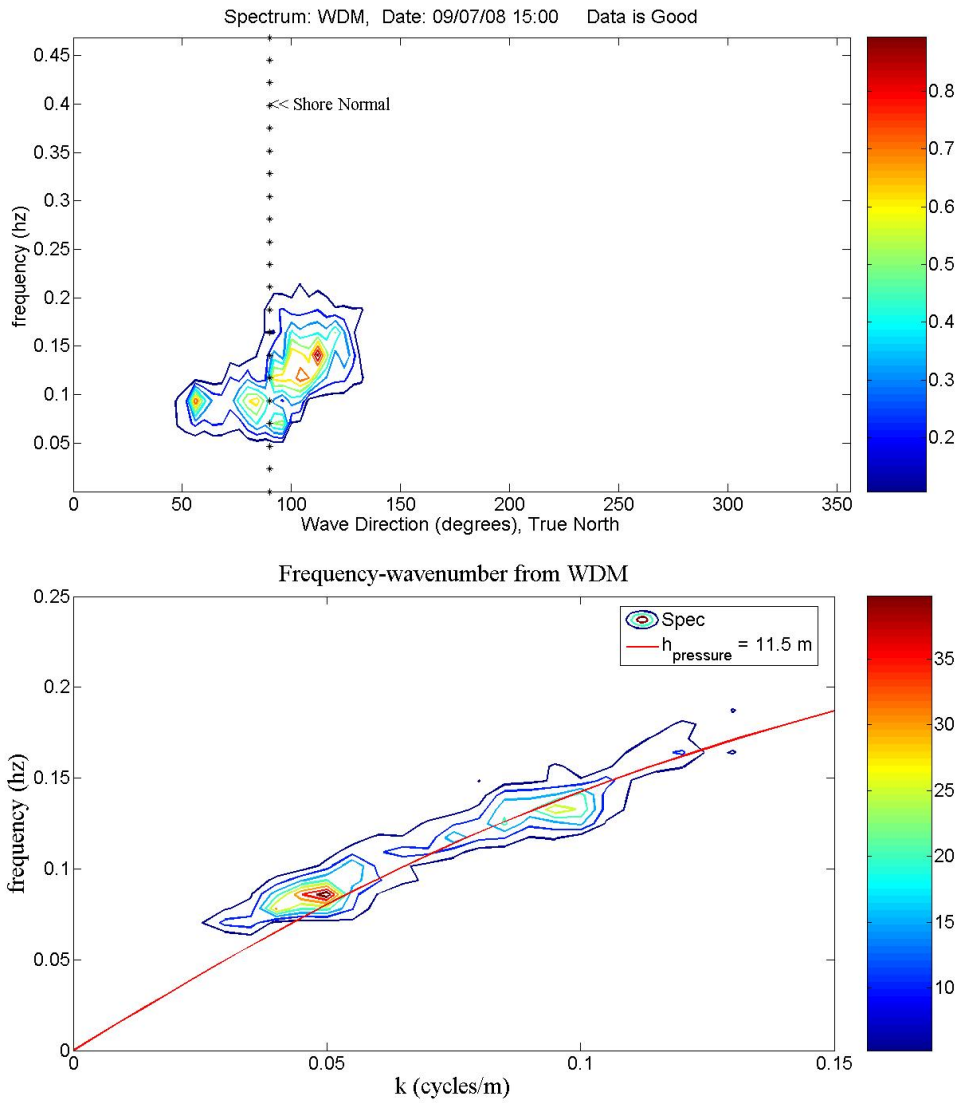

Figure 2.16: Directional spectrum and frequency-wavenumber spectrum estimates from application of WDM to the slope array. The linear dispersion curve for the known water depth at the slope array is plotted in red in the frequency-wavenumber spectrum. Results are from September 7th, 2008, 15:00 GMT

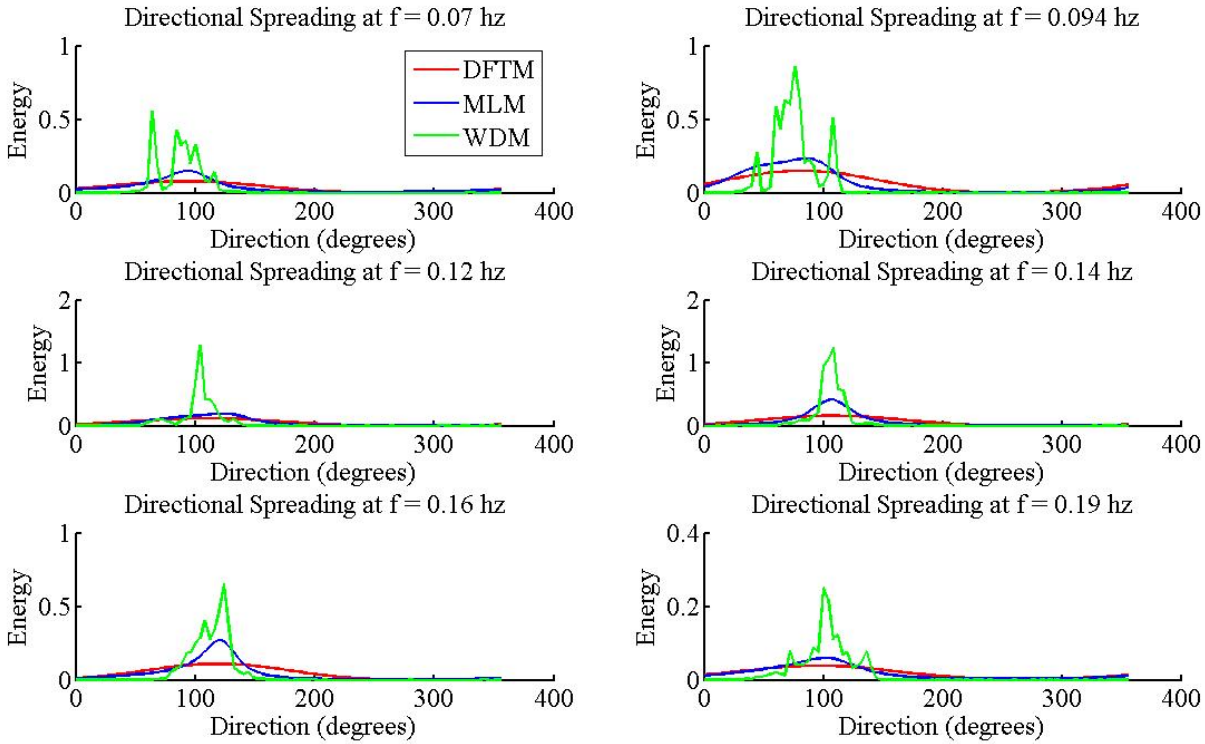

Figure 2.17: Comparison of directional spreading from DFTM, MLM and WDM on September 7th, 2008, 15:00 GMT

Chapter 3

DEVELOPMENT OF WDM DEPTH INVERSION

Predicting the water depth from time series imagery has been approached in a variety of ways as outlined in Chapter 1. Each method described in Chapter 1 has its own strengths and weaknesses. One depth inversion method might work well on dissipative beaches yet struggle on reflective beaches. Other depth inversion procedures might be suitable for large scale studies of the coastal zone where high spatial resolution is not required. For the present study at Bethany Beach, a depth inversion procedure suitable for steep beach profiles that provides high spatial resolution from time series imagery is desired. Here the theoretical framework for a new time-lag depth inversion procedure based on Donelan's wavelet directional method is given.

3.1 Using the Linear Dispersion Relation to Determine the Water Depth

It is well known among surfers that if a large storm is out at sea, they can expect forerunner long period waves to arrive at shore before the more energetic shorter period waves. The long period waves arrive first because they have a higher wave phase speed and wave group celerity. Therefore, the longer period waves disperse from the shorter period waves. A second phenomena of propagating surface gravity waves is the shortening of waves as they approach shallower water depths and begin to shoal. Both the dispersive nature of waves and the shortening of waves can be explained by the linear dispersion relation for small amplitude waves. The linear dispersion relation relates the wavelength, k, radial wave frequency, ω, and water depth, h, together as

$$\omega = \sqrt{gk \tanh kh} \tag{3.1}$$

where g is the gravitational constant. The dispersion relation can be re-arranged to show how the wave celerity, C, is dependent on the wave frequency and water depth as

$$C = \sqrt{\frac{g}{k} \tanh kh} \tag{3.2}$$

The decrease in wave celerity as the water becomes shallower can be more clearly seen in Figure 3.1 by plotting the wave celerity versus water depth for a range of frequencies. Re-arranging the dispersion relation again, it can be shown that the water depth can be computed from the wavenumber and wave frequency as

$$h = \frac{1}{k} \tanh^{-1} \left(\frac{\omega^2}{gk} \right) \tag{3.3}$$

or similarly from the wave celerity and wave frequency because the wave celerity and wavenumber are related by $C = \omega/k$. Therefore, solving for the wave celerity or wavenumber in addition to the wave frequency in depth inversion methods is essentially the same problem.

In deep water the particle orbits of wave do not reach the sea bed. Therefore, the propagation of deepwater waves is largely unaffected by the underlying bathymetry. The deep water approximation of the linear dispersion relation shows how the water depth can no longer be inverted from the dispersion relation.

$$\omega = \sqrt{gk} \tag{3.4}$$

This result places a limit on the maximum depth to which depth inversion techniques based on the dispersion relation will work. Similarly, the sensitivity of predicting the depth from the dispersion relation increases as the water depth increases because a small change in the wavelength will result in a large change in the water depth. In this study,

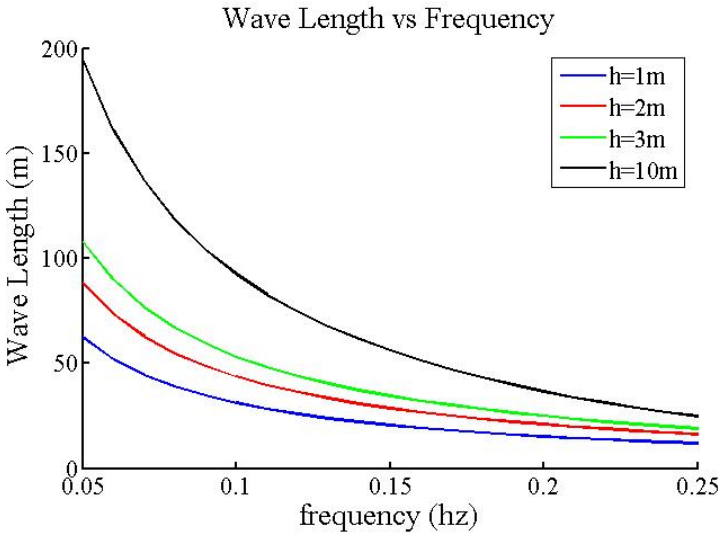

Figure 3.1: Wave Celerity versus water depth plot: Shows how the wave celerity decreases in shallower water

the range of energetic frequencies is from 0.08 Hz to 0.25 Hz. The 0.25 Hz waves are considered to be deep water waves at a water depth of approximately 14 meters, and the 0.08 Hz waves are considered to be deep water waves at water depth of approximately 100 meters.

Clearly the water depth can be predicted using the dispersion relation if the wavelength and wave period are known. However, the accuracy of using the linear dispersion relation is not as evident. More advanced solutions to the water wave boundary problem show the dispersive nature of waves are also related to the presence of currents and the nonlinearity of the waves. Due to the growing popularity of dispersion based remote sensing techniques, an investigation into the accuracy of applying the linear dispersion relation to depth inversion was performed by *Holland* (2001). Holland found that the linear dispersion relation could be used outside the surfzone with depth estimation errors on the order of 3-9%. Inside the surfzone, the nonlinearity of the waves cause water depth

estimates from using the linear dispersion relation to systematically overpredict the water depth. Errors inside the surfzone were found to sometimes exceed 50%. Methods to reduce the non-linear amplitude effects have been developed but are often difficult to implement in the field (*Grilli*, 1998).

3.2 Relating Pixel Intensity to Water Surface Elevation

Video images taken of the coastal zone record the amount of red, green, and blue light radiating toward the video camera. It is clear when looking at a video image of the coastal zone that an abundance of information is available. One of the most striking features apparent in a video image are the waves propagating toward shore (Figure 2.5). Waves are visible in an image because variations in the sea surface slope cause variations in the apparent brightness of the water. This phenomena is well known in physics and is called specular reflection of downwelling sky radiance (*Stockdon and Holman*, 2000). The front face of a steep wave appears darker because the steep slope of the wave causes reflection of light from a higher and darker altitude in the sky to be radiated toward the camera (*Lynch and Livingston*, 2001). A schematic showing how the scattering of light rays from ocean waves cause intensity variations in the reflected light visible by a camera is shown in Figure 3.2.

As a result of the specular reflection caused by ocean waves, valuable information about the sea surface conditions can be obtained from video images. Unfortunately, the intensity variations from a surface gravity wave are related to the magnitude of the slope of the wave and not the wave height. Therefore, it is not possible to determine the wave height directly from a single video image. However, the wave height is not necessary to determine the speed of propagating waves to the first order of linear wave theory. Only the spatial phase information such as the location of wave crests and troughs is required. The structure of the spatial phase information of the surface slope is the same as the wave elevation except that it is 90 degrees out of phase. As a result a time series from a single pixel in a video may serve as a valid proxy to an elevation gage if only the

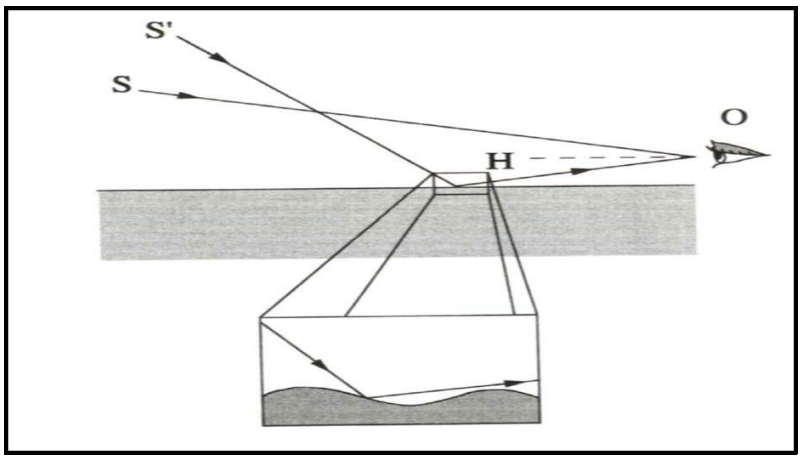

Figure 3.2: Specular reflection of downwelling sky radiance. In the presence of waves, the reflected light from the steep slope of the wave comes from a higher and darker altitude in the sky. Figure obtained from *Lynch and Livingston* (2001)

phase information of the waves are desired. A study by *Lippmann and Holman* (1991) proved that the wave speed could indeed be accurately determined from pixel intensity time series.

A comparison between an elevation time series calculated from the slope array at Bethany Beach and a pixel intensity time series from the video-observing system at Bethany Beach show that the periodicity is the same (Figure 3.3). Additionally the power spectrum of the pixel intensity time series and elevation time series are compared to show that the phase information in the pixel intensity and surface elevation time series are comparable (Figure 3.4). There appears to be more variance associated with very low frequencies and high frequencies in the intensity spectrum. The low frequency variance may be associated with varying brightness from the clouds or from discoloration of the water. The increase in the high-frequency variance is expected since the intensity spectrum is proportional to the sea surface slope spectral density, which places greater emphasis on the high-frequency part of the spectrum (*Walker*, 1994). This effect can be seen by the relation between the power spectrum, $S_{\eta\eta}(\omega)$, and sea surface slope spectrum, $S_{\eta_x\eta_x}(\omega)$,

by

$$S_{\eta\eta}(\omega) \propto \frac{1}{k^2(\omega)} S_{\eta_x\eta_x}(\omega) \tag{3.5}$$

where the high frequency components of $S_{\eta_x\eta_x}(\omega)$ become more important than the high frequency componenets of $S_{\eta\eta}(\omega)$.

3.3 Application of WDM to Pixel Arrays

Previous applications of the WDM have been to very small and compact wave gage arrays (*Donelan et al.* (1996); *Krogstad et al.* (2006)). The application of the WDM to larger compact arrays of pixel intensity measurements is straightforward. The configuration of the compact pixel array must be chosen from the video image such that it is small enough to provide good spatial resolution of depth measurements and avoid potential phase ambiguities. However, the pixel array must allow enough distance between pixels for the identification of significant phase lag. This topic, as well as how the water depth is calculated at the center of the pixel array from the frequency-wavenumber spectrum and an example of the application of the WDM procedure to the Bethany Beach video-observation system for September 7th at approximately 15:00 GMT are provided here.

3.3.1 Choosing a Compact Array

An advantage of remotely sensed images are that intensity time series can be obtained at each pixel in the image. Therefore, a wide range of options exist for compact array configuration. Unfortunately the spatial footprint for a given pixel in an image increases offshore, limiting the minimum distance between sensors. To illustrate this effect, uniformly spaced (in physical coordinates) cross-shore and alongshore arrays have been rectified and mapped to an image in Figure 3.5. If the offshore portion of the pixel array is blown up (Figure 3.5) it is evident that the pixel spacing between successive points in the cross-shore array, drastically decrease offshore.

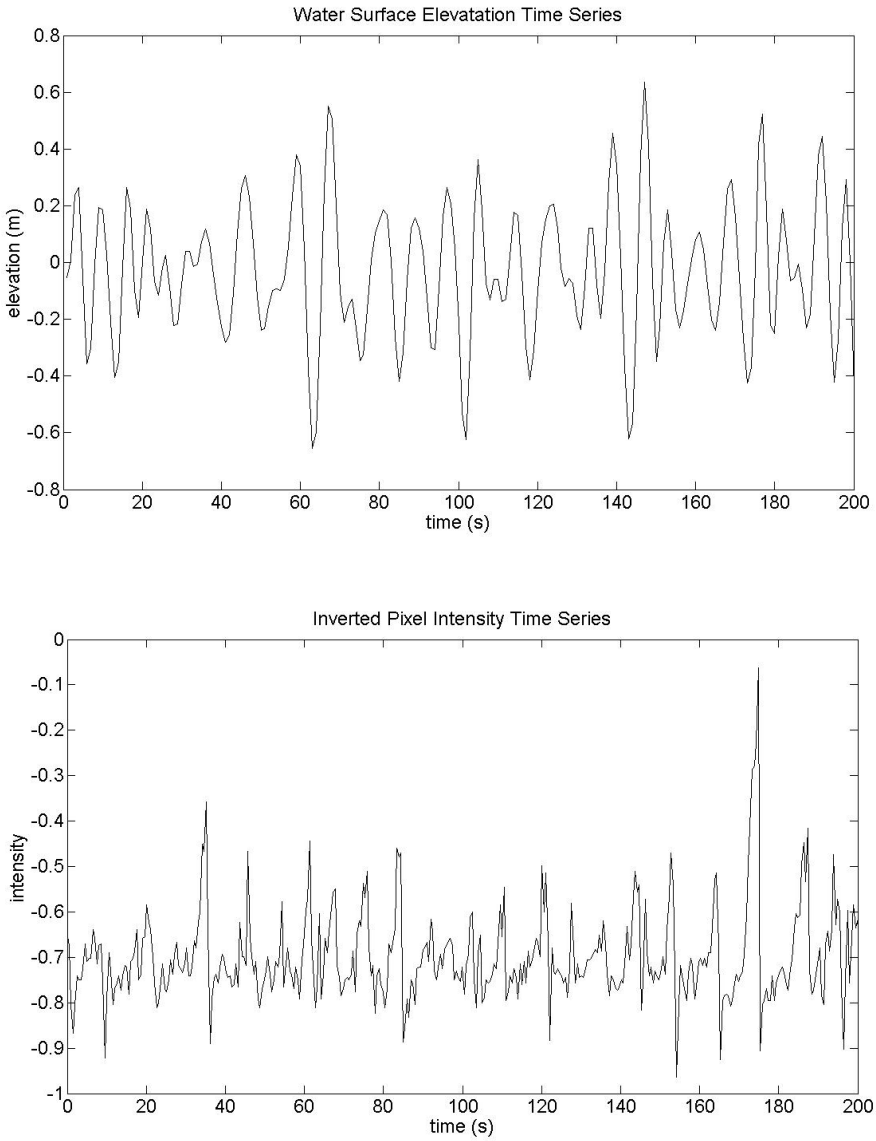

Figure 3.3: Comparison of water surface elevation time series to a pixel intensity time series. The elevation time series was obtained from the slope array and the pixel intensity time series was taken from the Bethany Beach observing system. Both time series were taken on September 7th at approximately 15:00 GMT. The wave conditions for this day are visible in Figure 2.5.

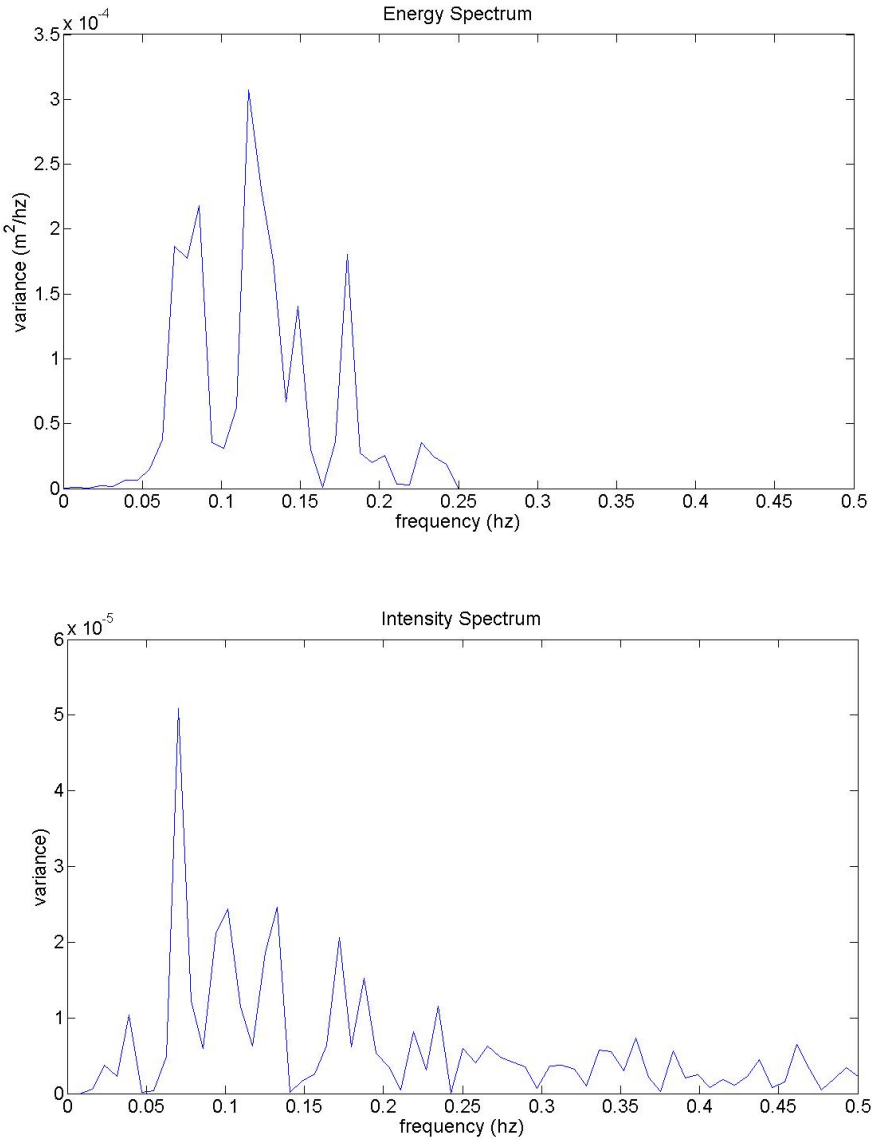

Figure 3.4: Comparison of water surface power spectrum and pixel intensity spectrum obtained from the slope array and video-observation system at Bethany Beach. Both time series were taken on September 7th at approximately 15:00 GMT.

Figure 3.5: Video image with the rectified arrays mapped to the image is shown in the top panel. The bottom panel shows an offshore portion of the pixel array blown up. Even though the real-world spacing between pixels in cross-shore array are constant, the pixel separation decreases offshore.

A separate spatial restraint imposed by the WDM on the pixel array is that the maximum separation distance between sensors, $\Delta \mathbf{x}_{mn}$, must be less than half the wavelength, L, expected to be resolved. This is in accordance with the Nyquist frequency limitation that states that the sampling rate must be at least $1/2$ as long as the shortest wavelength *Newland* (1993). For example, if the the maximum separation distance in the compact array is 10 meters than the minimum resolvable wavelength is 20 meters. Therefore, it is important to make sure the compact array has small enough spacing to resolve all the wavelengths of interest.

In this study a variety of different compact array configurations were tested. It is still unclear which array configuration is ideal for performing the WDM in remotely sensed images. Previous applications of the WDM to wave gage arrays used either triangular or pentagonal arrays. Based on previous studies, a similar shaped array, a hexagon with a central radius of 5 meters, was chosen as the array configuration (Figure 3.6).

3.3.2 Extension of WDM to Water Depth Estimation

The water depth is determined at the center of each pixel array by finding the best fit between the linear dispersion relation and the frequency-wavenumber spectrum calculated from the WDM. First, the weighted average wavenumber, k_{wa}, is computed from each wavenumber time series, $k^{LS}(f,t)$, generated by the WDM.

$$k_{wa}(f) = \frac{\sum_t k^{LS}(f,t) W(f,t) W^*(f,t)}{\sum_t W(f,t) W^*(f,t)} \tag{3.6}$$

Than a series of linear dispersion curves are generated for varying water depths, h.

$$\omega = \sqrt{gk \tanh kh} \tag{3.7}$$

The dispersion curve that minimizes the least square error, E^{LS}, between k_{wa} and the wavenumber from the dispersion curve, k_{disp}, over all frequencies is then selected as the water depth. The error between each k_{wa} and k_{disp} is weighted by the wavelet power

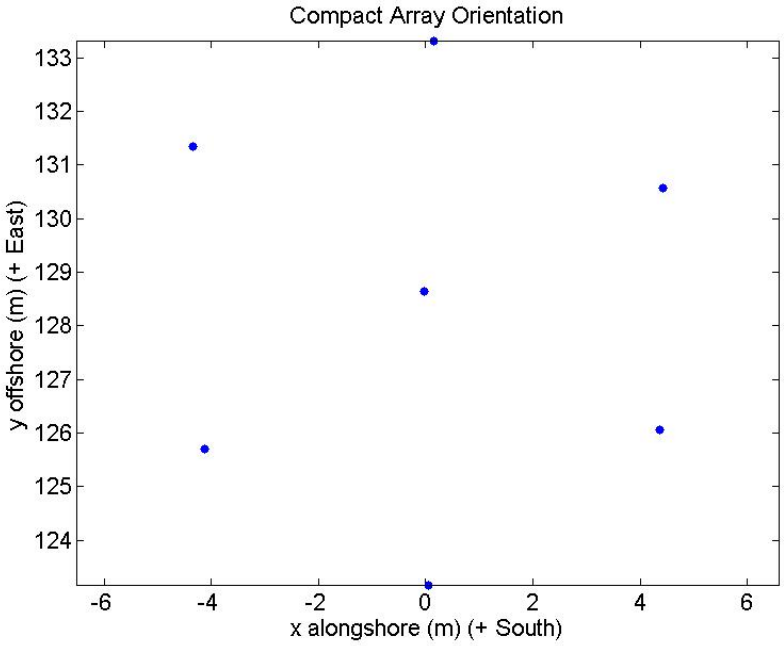

Figure 3.6: Compact array orientation used for the example on September 7th, 2008, approximately 15:00 GMT

spectrum, $S_w(f)$ in order to place more importance on the frequencies with large amounts of energy.

$$E^{LS} = \frac{\sum_f [k_{wa}(f) - k_{disp}(f)]^2 S_w(f)}{\sum S_w(f)} \tag{3.8}$$

The dispersion curve for the estimate water depth is shown with the frequency wavenumber spectrum in Figure 3.7.

In some instances it appears that the frequency-wavenumber spectrum is shifted toward lower wavenumbers (Figure 3.8), which may be a result of excluding nonlinear wave effects, which shift the frequency-wavenumber spectrum toward lower wavenumbers (*Holland*, 2001). If Stokes third order dispersion relation is calculated using the rms waveheight, H_{rms}, from the slope array, then errors from nonlinear wave effects can be reduced.

$$\omega^2 = \omega_0^2 \{1 + (\frac{kH}{2})^2 [\frac{5 + 2\cosh(2kh) + 2\cosh^2(2kh)}{8\sinh^4(kh)}]\} \tag{3.9}$$

Here the H_{rms} is used for the wave height, H. An example of how nonlinear wave effects can shift the frequency wavenumber spectrum is shown in Figure 3.8, from September 25th, 2008 15:00 GMT, where Stokes third order dispersion relation is plotted for the same water depth and wave numbers as the linear dispersion curve. The waves were very large on September 25th, and the H_{rms} wave height for this day was 2.48 m. Therefore, non-linear wave effects should be more pronounced and the shift in the frequency-wavenumber spectrum is more apparent in Figure 3.8

3.3.3 An application of the WDM depth inversion

An example of how the WDM can be extended to a compact pixel array is given in this section. The video data for this example was taken on September 7th, 2008, approximately 15:00 GMT. The incident wave conditions measured at the slope array for this example are shown in Figures 2.6 and 2.11 . The directional spectrum estimates from

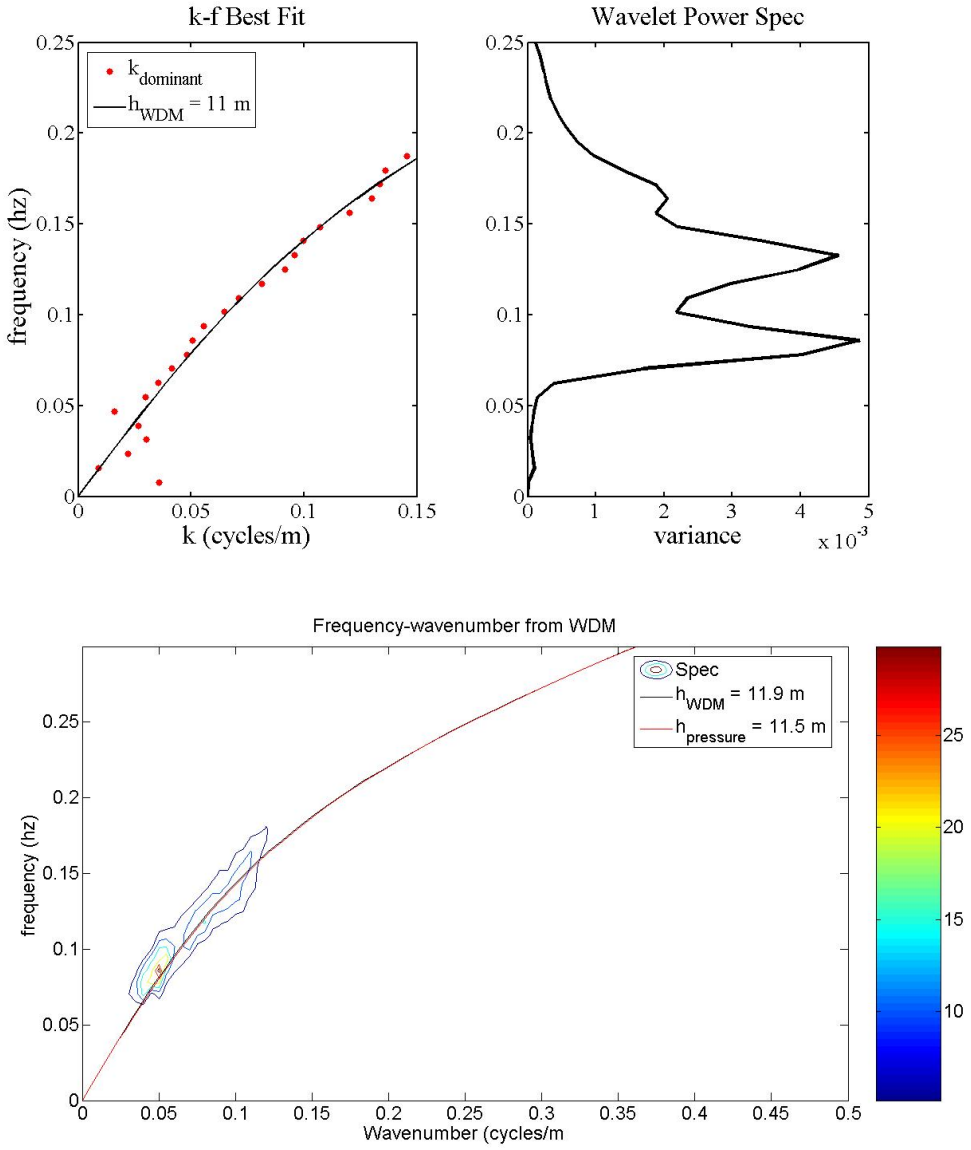

Figure 3.7: The top panel shows the best fit dispersion curve and the weighted average wavenumbers. The wavelet power spectrum is shown on the left, which is used to place more importance on the energetic frequencies. The bottom panel shows the best fit dispersion curve with the frequency-wavenumber spectrum.

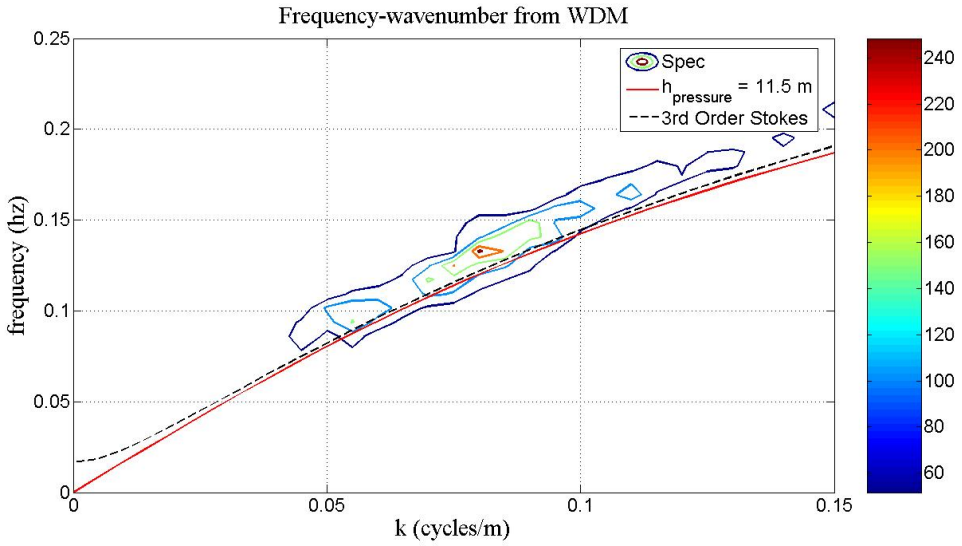

Figure 3.8: Example of nonlinear shift in the frequency-wavenumber spectrum resulting from large waves ($H_{rms} = 2.45m$)). The nonlinear 3rd order Stokes solution is given for the same water depth, 11.5, as the linear dispersion relation (red line). Example is from September 25th, 2008 15:00 GMT.

the slope array will be compared to the directional estimates obtained from the compact pixel arrays.

A convenient way to show the pixel intensity data of the sea surface is to create cross-shore time stacks, which show the pixel intensity time series along a cross-shore array. The top panel of Figure 3.9 shows the location of the pixel intensity time series. The resulting time stack is shown in the bottom panel of Figure 3.9, where each pixel intensity time series corresponds to a horizontal slice in the time stack. A distinct feature of the cross-shore time stack are the dark slanted lines representing the dark steep face of individual wave crests propagating toward shore (Figure 3.9). The slope of the dark lines corresponds to the wave celerity. As the waves approach shore the slope of the dark lines flattens out. This is expected since the celerity of waves decreases in shallower water. The white part of the time stack, located 100-120 meters offshore, corresponds to the white water generated from breaking waves.

The red box in Figure 3.9 contains one of the pixel intensity time series at the compact array, located just outside the surfzone, which is used in this example to show the inner workings of the WDM (Figures 3.10 and 3.11). The pixel intensity time series corresponding to the horizontal slice in the time stack enclosed by the red box is shown in top-panel of Figure 3.12. The wavelet transform and modulus of the pixel intensity time series clearly show the non-stationarity of the time series. It is evident in the wavelet transform that dominant frequency in the time series drifts between 0.02 hz and 0.08 hz. The large spike in both the pixel intensity time series and modulus corresponds to a very dark front face of wave propagating by the array at 175 seconds. This extremely dark front face corresponds to a large wave with a very steep front face. The cross-shore time stack suggests that this steep wave is part of one of the periodic low-frequency wave trains. However, the wavelet transform shows the presence of waves at higher frequencies at about 0.2 hz at this time. This is a result of the extremely dark intensity value causing anomomaly high wavelet transform values at higher frequencies.

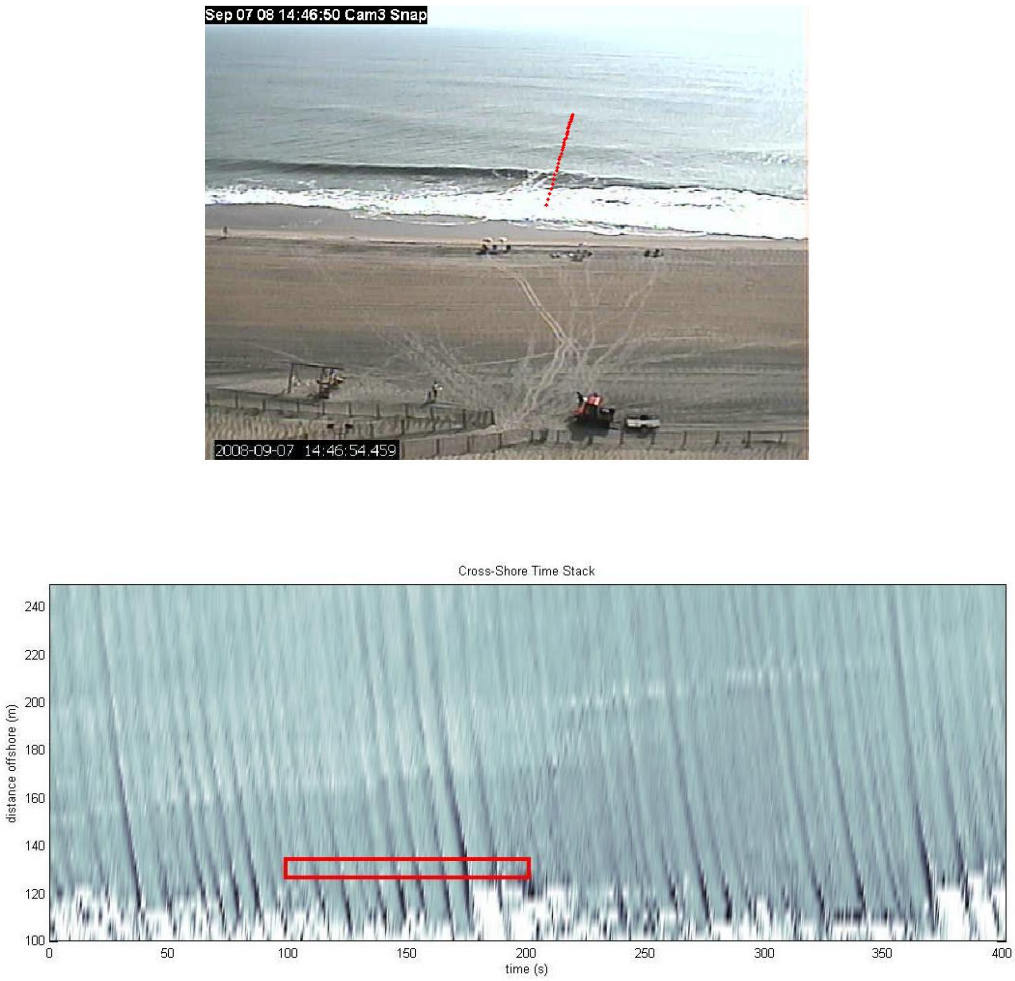

Figure 3.9: The top panel shows the location of pixel intensity time series use to make time stack are shown with red dots. Bottom panel shows the cross-shore time stack, the red box contains the pixel intensity time series shown later in this example. Images from September 7th, 2008, approximately 15:00 GMT

Figure 3.10: Image location of pixel array, shown with red dots, used in example.

The WDM steps in generating wavenumber and wave direction time series for the most energetic frequency of 0.08 hz is shown in Figure 3.13. Sensors 3 and 5 are cross-shore oriented with each other and are seperated by 10 meters. One noticable difference between the slope array example (Figure 2.15) and the compact pixel array example here is that the phase phase lag between the sensors is significantly larger. This result is expected since the distance between sensors in the compact pixel array is 5 times as large. As in the case of the slope array it is evident that there is a slow drift in the wavenumber and wave direction time series. The slow drift can be attributed to the shift in the actual frequency of the waves present in the time series. The mean phase gradient of all sensors in the compact array is plotted in the bottom panel of Figure 3.13, and shows how waves at slightly lower and high frequencies are contained in this frequency of the wavelet transform.

The directional spectrum results from the compact pixel array are show in right panel of Figure 3.14. The WDM spectrum estimate at the slope array has been shoaled

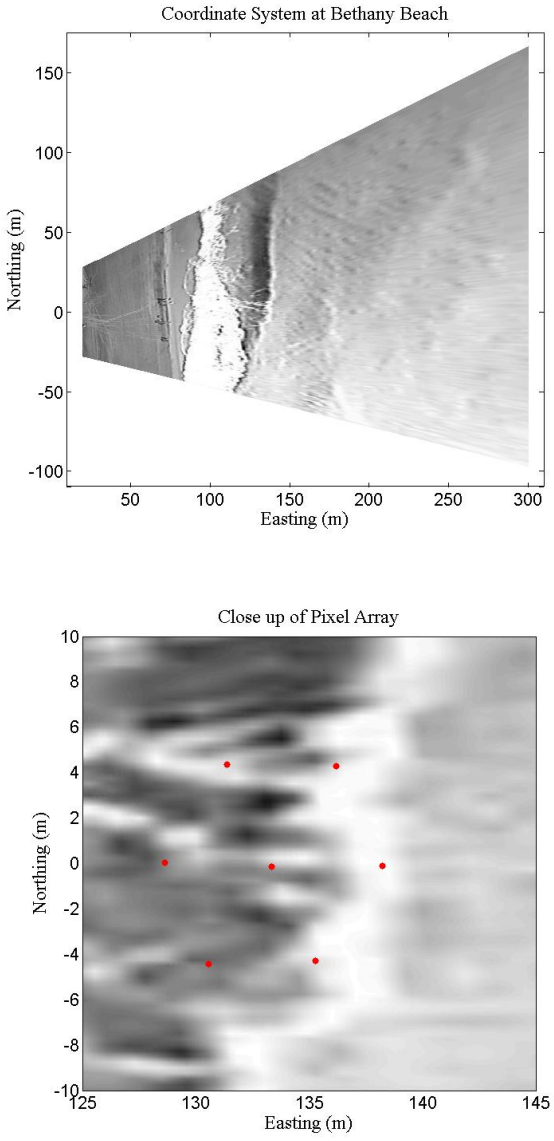

Figure 3.11: Geo-rectified image location of pixel array, shown with red dots, used in example. The bottom panel shows a close up of the pixel array.

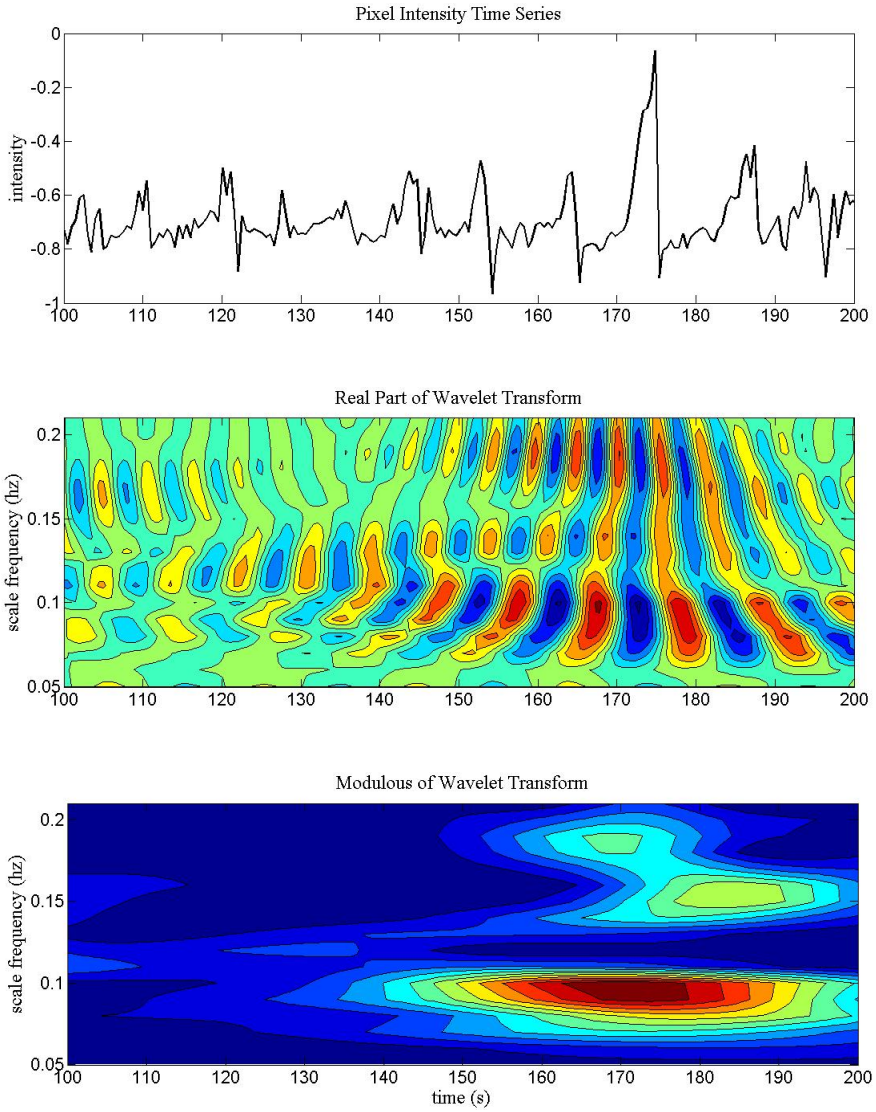

Figure 3.12: Pixel intensity time series and its wavelet transform for WDM example. The wavelet transform and the modulus of the wavelet transform show the non-stationarity of the time signal. September 7th, 2008, 15:00 GMT.

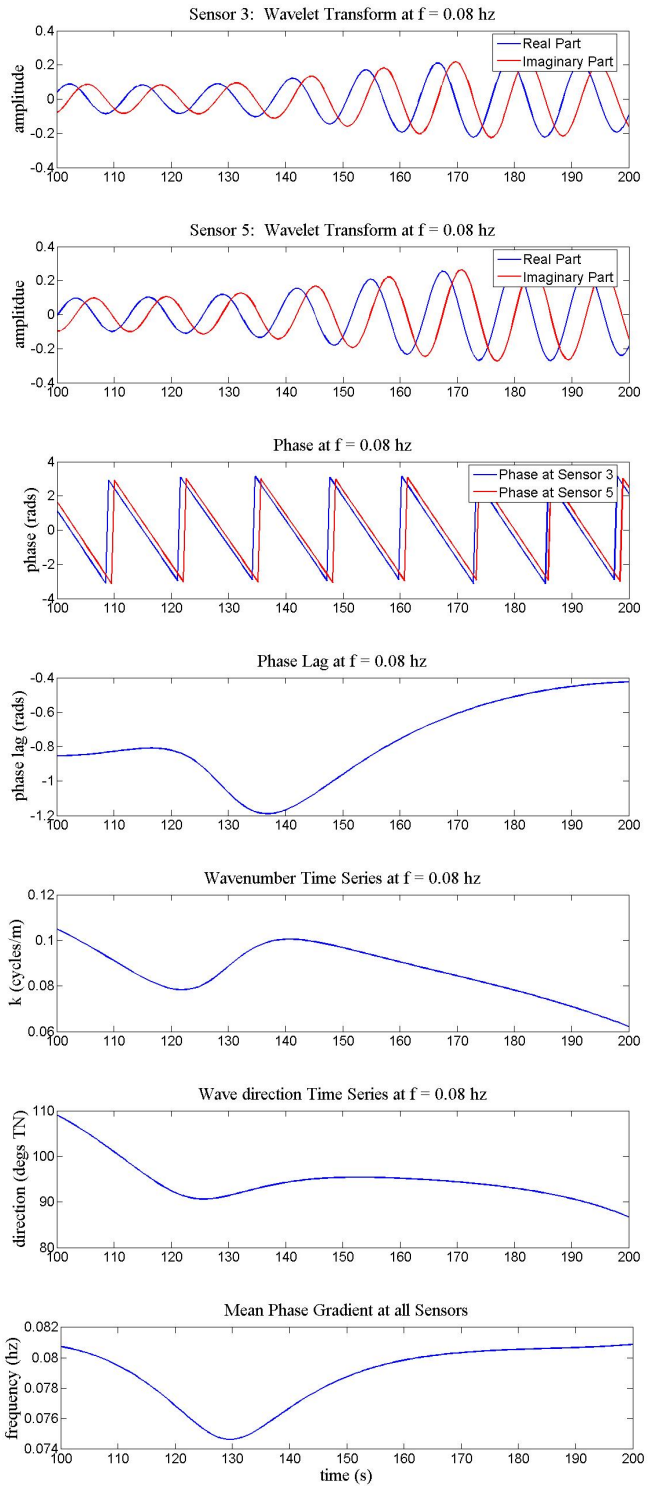

Figure 3.13: Application of WDM to pixel array. Results are from September 7th, 2008, 15:00 GMT.

and refracted to the estimated water depth at the compact pixel array to compare the accuracy of the compact pixel array directional spectrum. The directional distribution in energy shown for the compact pixel array compares favorably with the slope array spectrum. Both directional spectrums show the presence of the dominant wave train at 0.12 hz and 105 degrees true north. The frequency-wavenumber spectrum from the compact pixel array is shown in Figure 3.15, with the dispersion curve for the estimated water depth shown in black. The dispersion curve closely follows the frequency-wavenumber spectrum. Therefore, it is expected that the water depth is accurately estimated by linear wave theory at this location. The directional spectrum, frequency-wavenumber spectrum, and corresponding water depth can be estimated similarly at each location of the compact pixel arrays shown in Figure 3.16. This provides depth profiles as well as information about the transformation of waves from offshore to the surfzone.

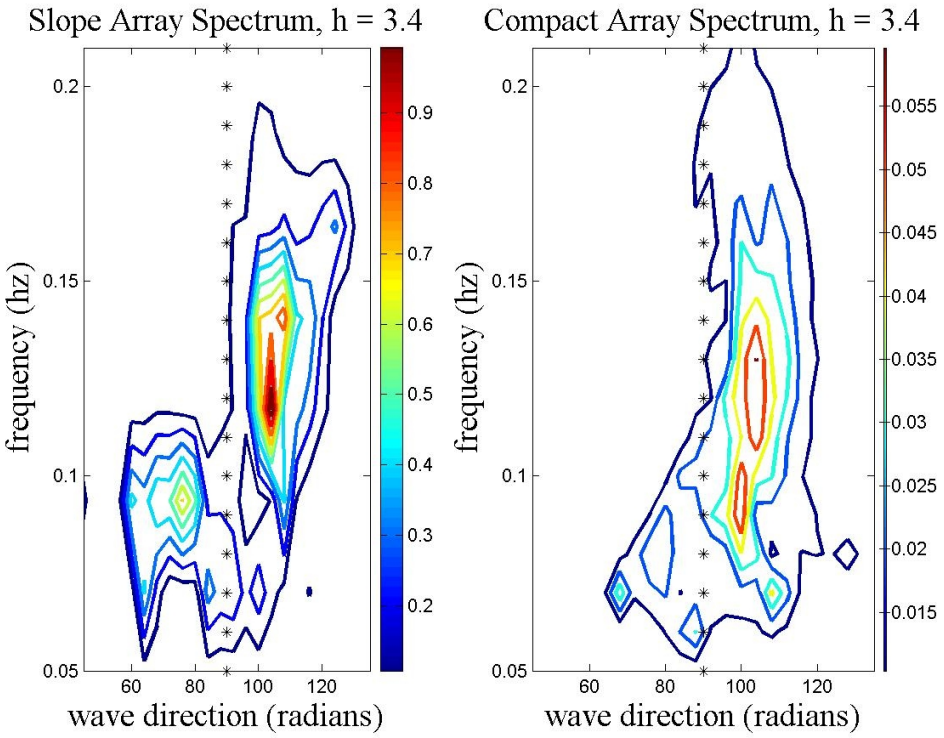

Figure 3.14: Comparison between refracted and shoaled slope array directional spectrum (left panel) and the WDM directional spectrum at the pixel array (right panel). Results are from September 7th, 2008, 15:00 GMT.

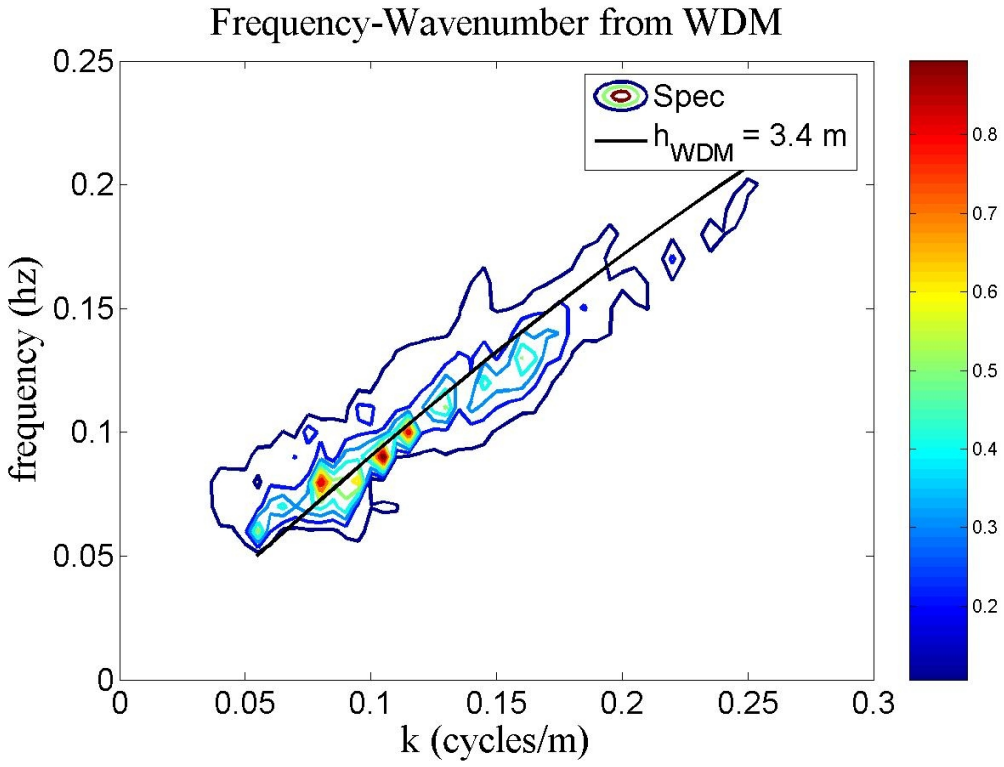

Figure 3.15: Frequency-wavenumber spectrum calculated from the pixel array on September 7th, 2008, 15:00 GMT. The best fit linear dispersion curve is shown in black.

Figure 3.16: Series of compact pixel arrays extending out into deeper water. Each compact pixel array can be used to estimate the directional spectrum and water depth.

Chapter 4

KAYAK SURVEYING SYSTEM

4.1 Introduction

Personal water craft (PWC) surveying systems have become a popular alternative to conventional survey methods due to their speed and maneuverability (*Beach et al.*, 1994). PWC surveying systems have been shown to yield accurate bathymetric measurements, with vertical errors < 5 cm (*Dugan et al.*, 1999). However, PWC surveying systems typically cost about $90,000 (*MacMahan*, 2001) and may be restricted from small lakes, lagoons, and areas where PWC's are prohibited. A low cost surveying system, that can be easily deployed in a variety of hard to reach places, has been developed by extending the PWC surveying concept to a kayak. For this study the kayak surveying system provides ground truth bathymetry at Bethany Beach, DE which is used to measure the performance of the video-based depth inversion.

4.2 Setup

The design of the kayak surveying system creates a completely detachable system, that can be easily transported and quickly reassembled in the field. In addition, the kayak surveying system allows for a single person to complete the entire survey process, from the transportation of the kayak system to the actual survey. The kayak surveying system reduces costs by using a less expensive hand held L1 GPS receiver (Mobile Mapper Pro, Table4.1), and a simple data acquisition system (PBX data logger, Table 4.1). Other key components of the survey system are a smart echosounder, which returns data in ASCII

format after power is applied, two removable water proof boxes, and an Ashtech L1 GPS antenna. The complete kayak system can be viewed in Figure 4.1, where (A) is the echosounder, (B) is the location of L1 antenna, (C) is water proof box containing battery and data logger, (D) is water proof box containing hand held GPS. The complete cost of the kayak system is approximately $6,500, a significant reduction from the $90,00 of the PWC survey system .

Table 4.1: Kayak Component List and Cost

Component	Cost ($)
Ocean Kayak Caper	550
Benthos PSA 916 Sonar Altimeter	2,200
Magellan Mobile Mapper Pro	1,750
Ashtech L1 Antenna	700
PBX Data Logger	600
Underwater Kinectics 609 Box	40
Otter Box 3500 Box	40

The echosounder draws 12v-24v of power and it as well as the data logger can be powered by a small 3.4 amp/hour battery. The data logger has two serial ports and simultaneously records the echosounder ASCII strings and GPS NMEA strings. An internal clock in the data logger provides a time stamp of when each data string was recieved and the GPS NMEA strings contain the GPS time, which allows the internal data logger time to be related to GPS time. Relating the GPS time to the internal clock in the data logger is important because it allows more accurate post-processed GPS data to be stiched back with the echosounder data.

4.3 Methods

The accuracy of the inexpensive GPS survey system was improved by correcting carrier phase information with a nearby base station (National Geodetic Surveys Continuously Operating Reference Stations [http://www.ngs.noaa.gov/]). *Saeki and Hori* (2006)

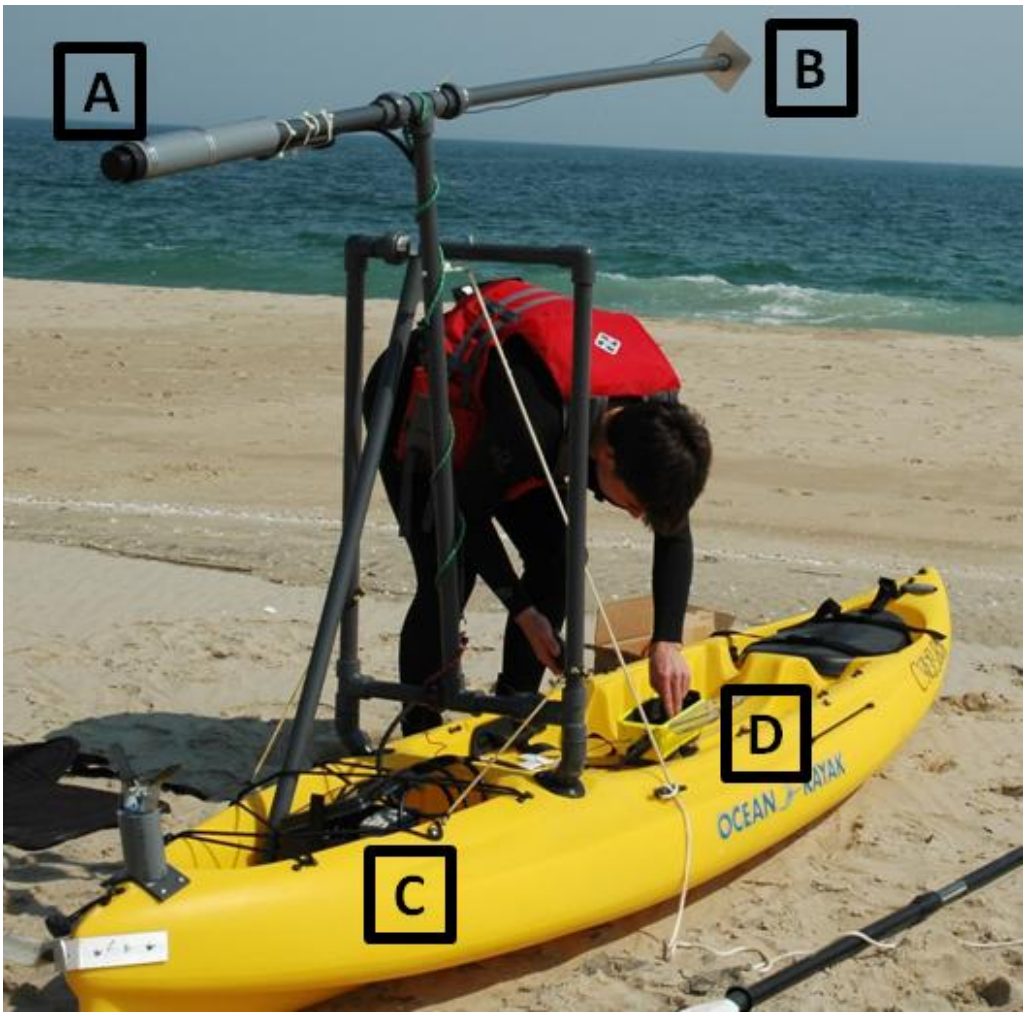

Figure 4.1: Kayak system: (A) echosounder, (B) patch antenna, (C) water proof box containing battery and data logger, (D) water proof box containing hand held GPS.

found that the weakest link of L1 GPS survey systems is the antenna. Originally, a small patch antenna, a little bigger than a quarter, was used in the kayak system. However, despite using a metallic multipathing plate, low-frequency fluctuations on the order of 30 cm in the vertical elevation were observed in stationary tests of the patch antenna and L1 receiver (Figure 4.3). In previous applications to static positioning systems, higher accuracy in vertical GPS measurements was obtained from patch antennas by time-averaging the signal (*Saeki and Hori*, 2006). For bathymetric measurements instantaneous GPS measurements are desired because the water surface elevation is changing due to tides and waves. Therefore, improved accuracy of the GPS measurements from time averaging is not applicable.

The shortcomings of the patch antenna were resolved by replacing the patch antenna with a more expensive and sophisticated Ashtech L1 antenna. The accuracy of the patch antenna and Ashtech antenna were evaluated by performing separate stationary tests with each antenna and the L1 receiver. For the stationary tests, the GPS antenna was mounted to a tripod for over 80 minutes and the vertical error of the antenna was measured as deviations from the mean of the signal. The maximum vertical errors from the patch antenna were 30 cm in comparison to 6 cm for the Ashtech antenna (Figure 4.3). The standard deviation of the errors using the patch antenna were reduced from 13.9 cm to 2.41 cm using the Ashtech antenna.

An additional dynamic GPS test was performed by mounting a survey grade GPS antenna and Ashtech antenna to a backpack (Figure 4.3) and walking up and down a dry beach profile. For the dynamic test the survey grade GPS was treated as the control elevation, yielding maximum vertical error estimates for the Ashtech antenna comparable to the stationary test of 8 cm (Figure 4.3). However, there was an increase in high frequency errors on the order of 2 cm due to the walking motion and differential tilting and bobbing of the two GPS antennas mounted to the backpack.

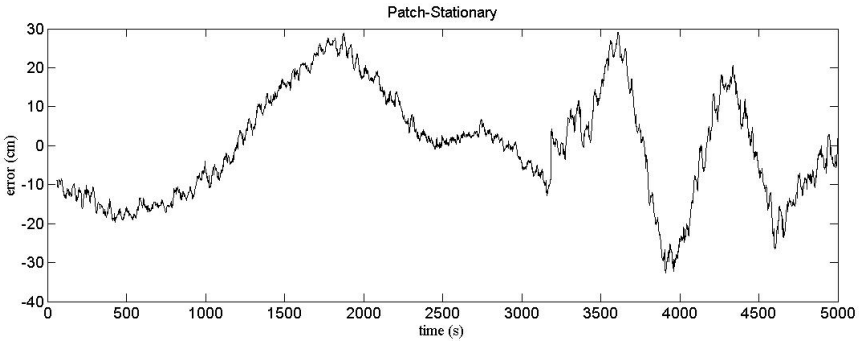

(a)

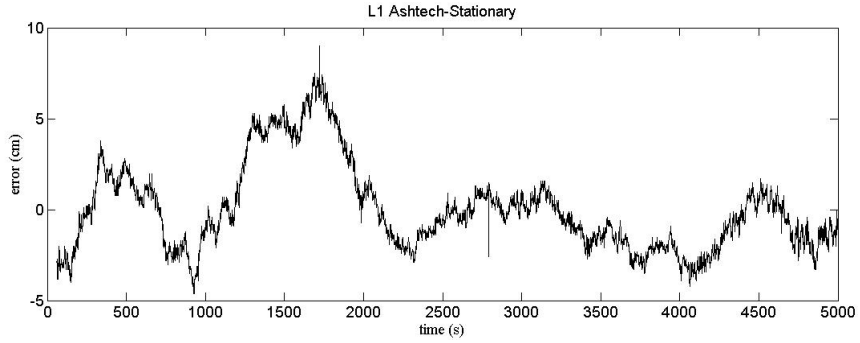

(b)

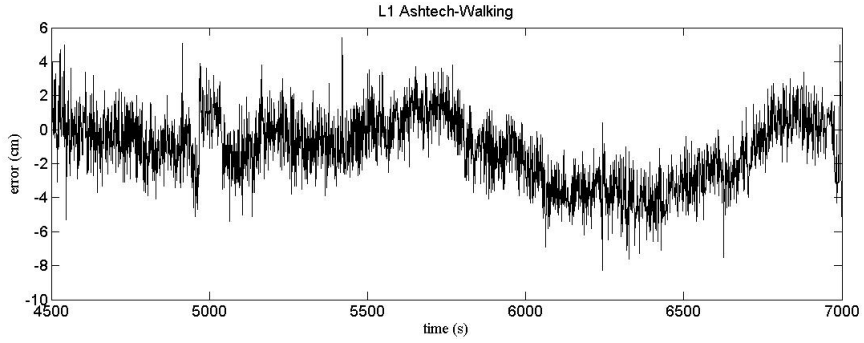

(c)

Figure 4.2: GPS test results from (a) stationary patch antenna, (b) stationary L1 Ashtech antenna, and (c) dynamic L1 Ashtech antenna. The vertical axis is the elevation error in cm.

Figure 4.3: Back pack with both GPS units mounted, which was used for the walking survey, and for dry beach and wading surveys.

4.4 Results

A cross-shore transect of the survey results from the kayak system are presented in Figure 4.4 for Bethany Beach, DE on October 1st, 2008. The blue line is the kayak bathymetry surveyed in meters relative to NAVD88 and the green line is a walking survey of the dry beach and shallow water taken on Oct 1st, 2008. There was about 20 meters of overlap between the walking and kayak survey. The overlap illustrates the good agreement between the two surveys. However, in this region of overlap the kayak systematically over predicts the bathymetry relative to the walking survey. The deeper bathymetry taken by the kayak can be attributed to slight errors in the echosounder measurements from the pitching and rolling of the kayak in waves, which has been removed in the past by including pitch-and-roll sensors in PWC systems. The red line in Figure 4.4 corresponds to a beach survey taken by DNREC in June, 2008. The DNREC survey was taken with a vessel-mounted survey system. The complete bathymetry map generated by the kayak and back pack is shown in Figure 4.5.

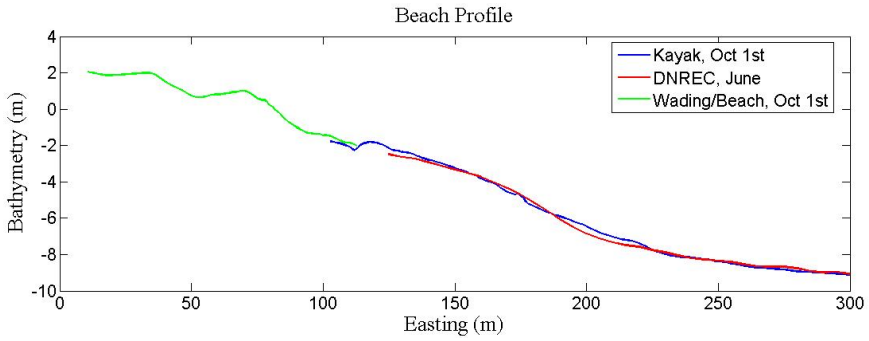

Figure 4.4: Beach survey results taken at Bethany Beach, DE on Oct 1st. The walking beach profile is plotted in green, the kayak beach profile is plotted in blue, and DNREC's beach profile taken during June is plotted in black.

Comparison between the kayak and DNREC beach profile show similar bathmetry measurements in shallow water and nearly identical bathymetric measurements offshore. It is expected that the bathymetry at Bethany Beach will have changed during the 3

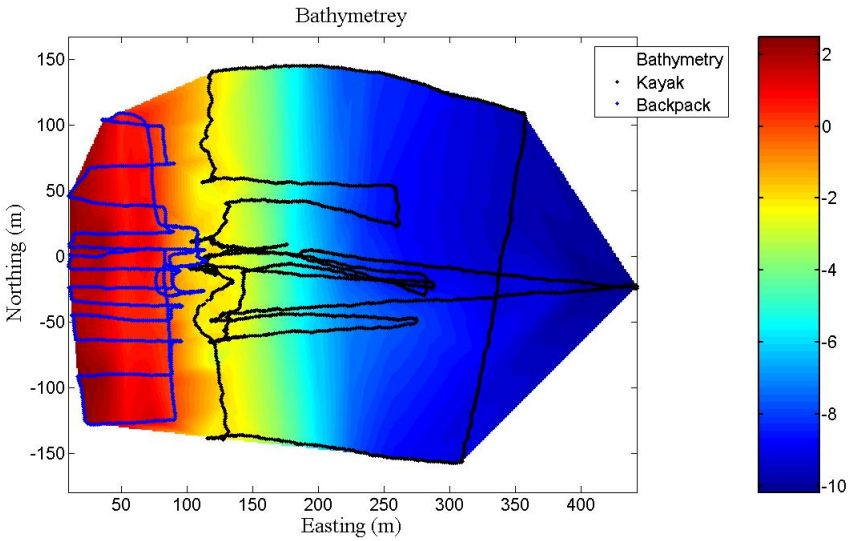

Figure 4.5: Bathymetry map from kayak and walking suvery on Oct 1st, 2008. The blue dots correspond to walking survey points and the black dots correspond to kayak survey points.

months separating the two surveys. However, in deeper water bathmetric changes are expected to be small unless there is an extreme wave event, and therefore the nearly identical bathemetric measurements offshore can be used to validate the kayak surveyor system. A reduction in bathymetry errors can be achieved by inclusion of a pitch-and-roll sensor, but this would increase costs and require a more sophisticated data acquisition system. Errors from pitching and rolling can be minimized by restricting depth measurements to times when the kayak is traveling in the same direction of the waves or by simply surveying during low wave conditions.

4.5 Summary

The extension of the PWC surveying system to an ocean kayak yielded a low cost, and extremely flexible surveying device. Costs were reduced by using a L1 GPS receiver and simple data acquisition system. Improved accuracy was obtained from the L1 GPS

system by using an L1 Ashtech antenna and post processing the GPS data using nearby base stations. The GPS system was shown to produce accurate elevation measurements with a standard deviation of 2.41 cm and bathymetric survey results from the kayak survey system compare favorable with walking surveys and a previous survey taken by a conventional survey system. The kayak surveying system provides a simple device for surveying hard to reach inland waters that may not be accessible by PWC's.

Chapter 5

FIELD RESULTS AT BETHANY BEACH

5.1 Setup for Field Study

There are three major components of the field study at Bethany Beach, DE; the video-observation system overlooking the shoreline at the field site, (Figure 1.3), the slope array, which is located just offshore of the field site at a nominal depth of 10 meters, and the kayak hydrographic surveyor. The combination of the three components allows for the performance of the video-based directional spectrum estimator and of the video-based depth inversion algorithm to be evaluated. The video-observation system generates intensity time series at a series of compact pixel arrays (Figure 3.16), which are used by the WDM to estimate the directional spectrum and beach profile. The directional spectrum estimated at the slope array can be shoaled and refracted, and then compared to the video-based directional spectrum. The kayak surveyor is used to generate bathymetry maps and beach profiles that are used to evaluate the performance of the video-based depth inversion.

The coordinate system used in the field study is shown in Figure 2.3, where the easting and northing are in Delaware State Plane Coordinates relative to a user defined spatial datum (Easting = 759845.02 m, Northing = 193594.10 m). The vertical coordinates are relative to NAVD88 datum. The GPS measurements used in the camera model for the video observation system were taken in Delaware State Plane coordinates. However, since the camera model maps each pixel in the image to a horizontal plane at a fixed elevation, the water surface elevation needs to be determined for the time of the image.

The water surface elevation is determined from the hydrostatic water depth measurements at the slope array. In order to compare the bathymetrys measured by the kayak surveyor and video camera, GPS measurements taken by the kayak surveyer are converted from WGS84 coordinates to Delaware state plane coordinates using Corpscon ((cor, 2004)).

In this chapter field results from two separate days, Sept 30th, 2008, and Oct 1st, 2008, are analyzed. The incident wave conditions for the two days can be seen from the snapshots taken by the video-observation system (Figure 5.1). The power spectrum and directional spectrum at the slope array, calculated using the different estimators, is shown in Figures 5.2 and 5.3. The wave conditions for Sept 30th and Oct 1st, consisted of a narrow banded spectrum with the dominent wave frequency and direction of 0.1 Hz, 85 degrees True North and 0.08 Hz, 80 degrees respectively. The cross-shore time stacks for both days show clearly visible wave trains propagating towards shore (Figure 5.4).

(a) Sept 30th, 15:45 GMT (b) Oct 1st, 19:47 GMT

Figure 5.1: Wave conditions as seen by the video cameras.

5.2 Performance of Video-Based WDM Directional Spectrum Estimator

The results from the video-base WDM directional spectrum estimator at an on-shore and offshore compact array location can be seen in Figures 5.5 and 5.6 for Sept 30th, 2008, 15:00 GMT and Oct 1st, 2008, 15:00 GMT. The refracted and shoaled directional spectrum estimates from the slope array using the WDM have been shown in

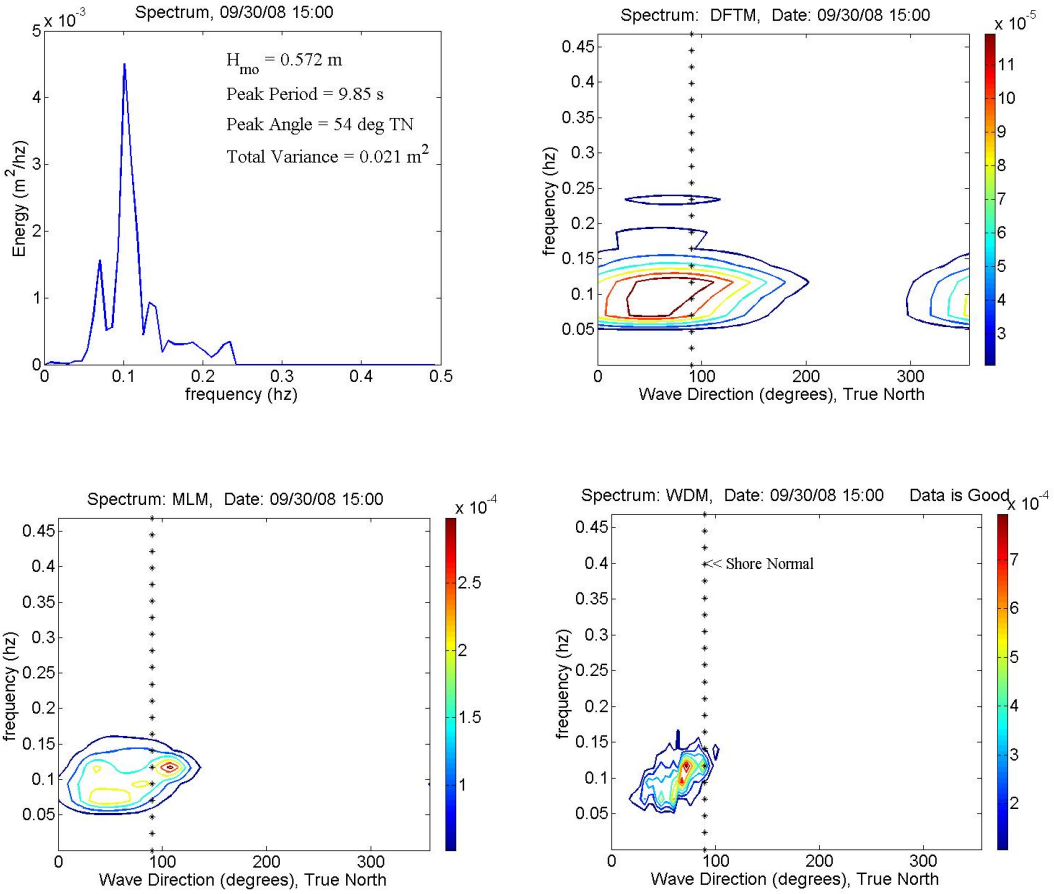

Figure 5.2: Spectrum estimates calculated at the slope array for September 30th, 2008, 15:00 GMT

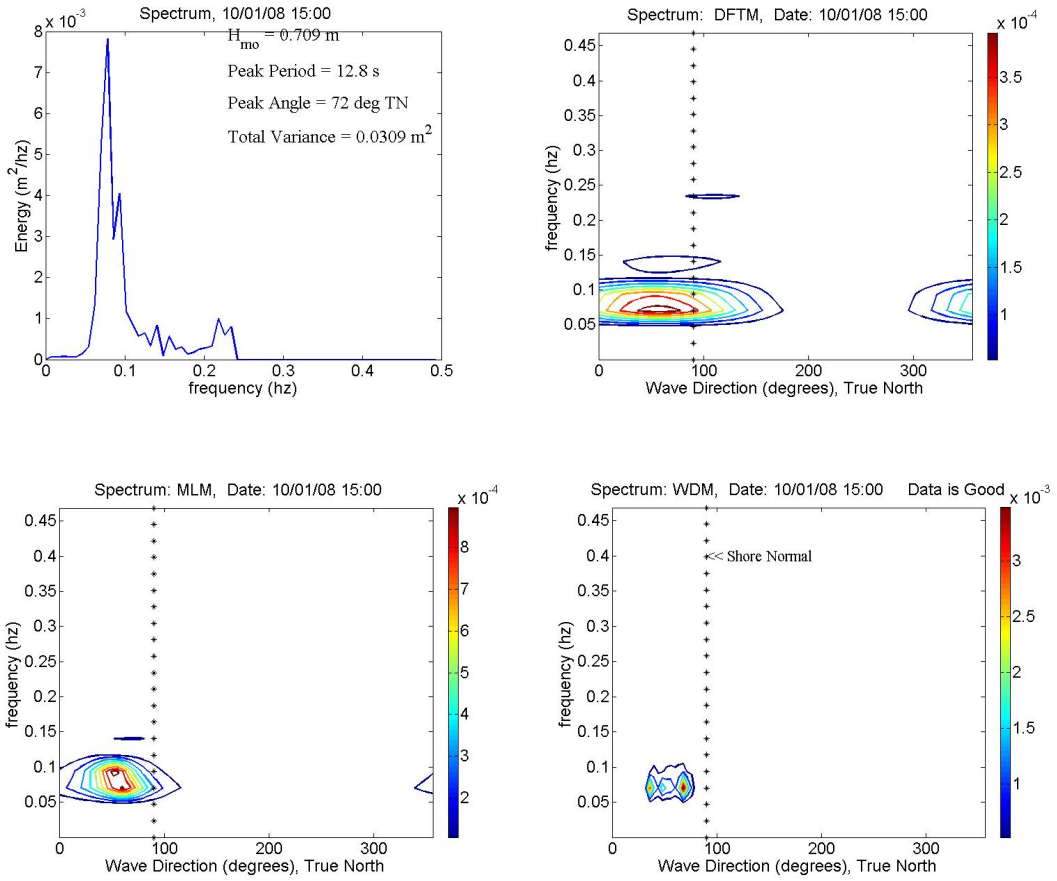

Figure 5.3: Spectrum estimates calculated at the slope array for Oct 1st, 2008, 15:00 GMT

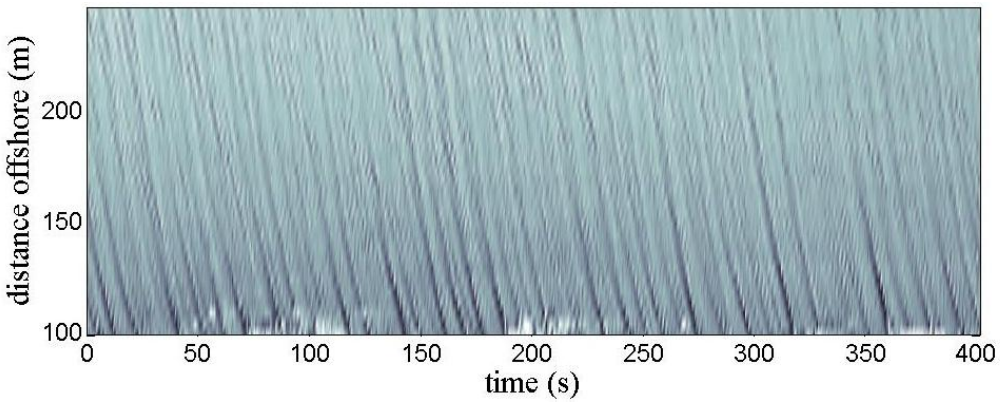

(a) Sept 30th, 2008

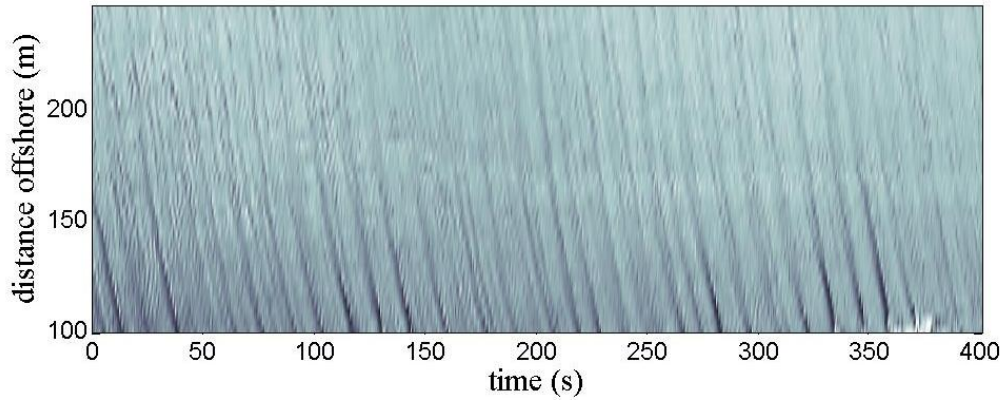

(b) Oct 1st, 2008

Figure 5.4: Examples of cross-shore time stacks from field tests.

Figures 5.5 and 5.6 for comparison. Figures 5.5 and 5.6 illustrate the ability of the video-base WDM directional spectrum estimator to calculate the distribution of wave energy in direction and frequency. The refraction of waves as they enter shallow water is evident in directional spectrum results because the wave energy shifts toward shore normal wave directions (90 degrees TN). A complete set of video-base WDM directional spectrum estimates for an hourly data set can be seen in Appendix B.

5.3 Performance of Video-Based WDM Depth Inversion

5.3.1 Definitions of Statistics Describing Performance

Hourly data from each test day were used to estimate the depth at each compact pixel array location. A computational difficulty arose because the real-world location of each pixel array is affected by the tide level. The cross-shore location of compact pixel array may shift as much as 5 meters depending on the tide. Therefore, in order to perform statistical analysis of the data each hourly profile was interpolated to a cross-shore grid with a cross-shore spacing of 1 meter. As a result at each cross-shore grid location there are up to 12 tide corrected water depth estimates, $h_i(y)$. For this study, any pixel intensity time stacks that contained poor data due to darkness, sun glitter, or cloud were removed from the data set. Figure 5.7 illustrates an example where clouds caused low frequency variations in the pixel intensity. In the future, quality control parameters should be defined to remove poor estimates resulting from poor image quality. For both days, 7-8 hourly data sets were used to calculate the daily beach profile. In this study the accuracy of determining the daily beach profile, $\hat{h}(y)$, from the median and mean were investigated.

A confidence interval for each cross-shore position can be defined based on the variance in the depth estimates at that location. Based on the central limit theorem, a 95% confidence interval, $E(y)$ can defined as

$$E(y) = \frac{1.96S(y)}{\sqrt{N}} \tag{5.1}$$

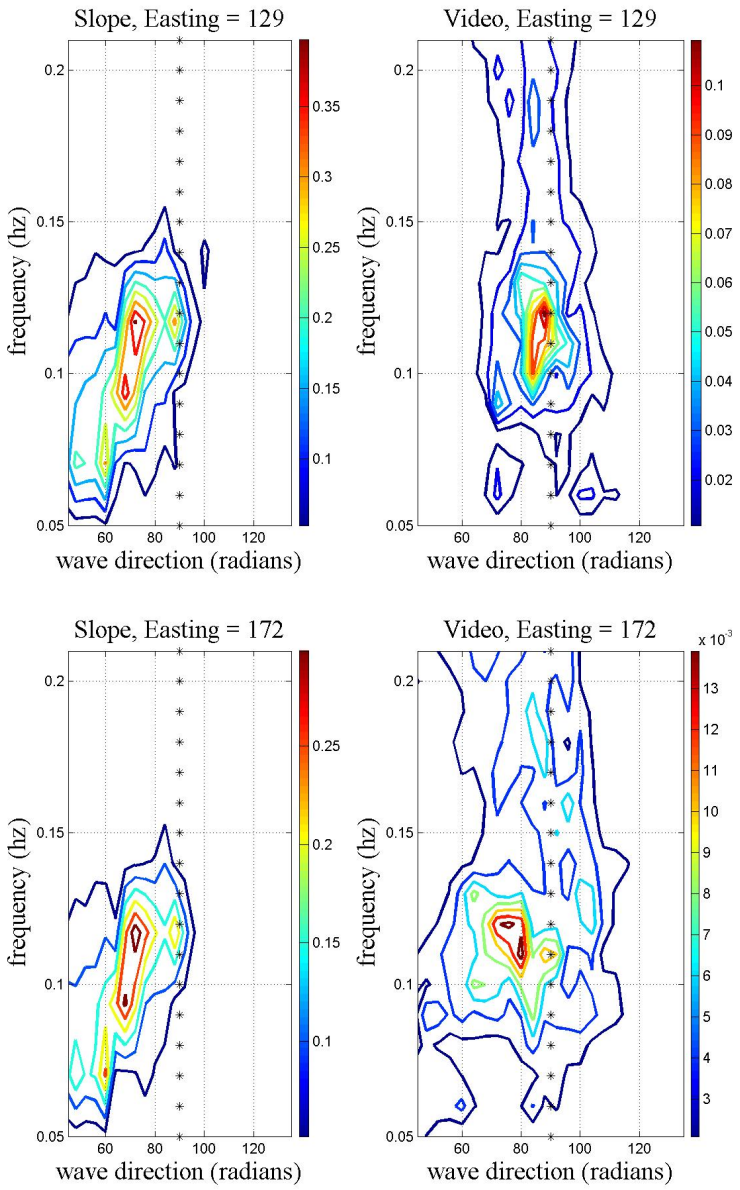

Figure 5.5: Comparison between directional spectrum estimates from the slope array and video images on Sept 30th, 2008, approximately 15:00 GMT. The slope array directional spectrum shown here was estimated with the WDM and has been refracted and shoaled to the same depth as the pixel array directional spectrum.

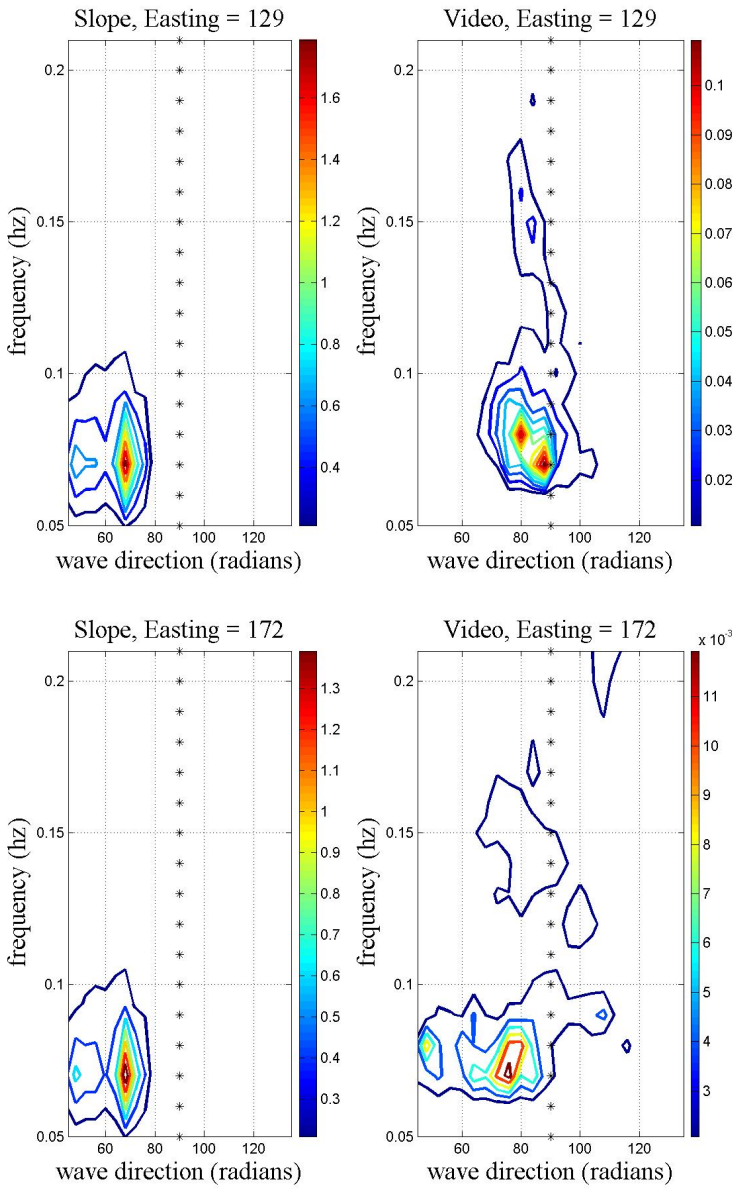

Figure 5.6: Comparison between directional spectrum estimates from the slope array and video images on Oct 1st, 2008, approximately 15:00 GMT. The slope array directional spectrum shown here was estimated with the WDM and has been refracted and shoaled to the same depth as the pixel array directional spectrum.

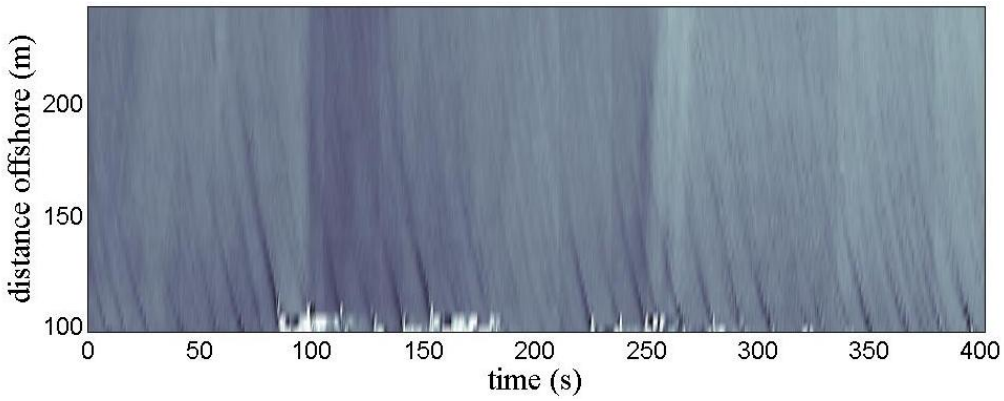

Figure 5.7: Example of cross-shore time stack in which the presence of clouds cause low-frequency variations in the pixel intensity. Taken on Oct 1st, 2008, 16:50 GMT

where S is the standard deviation of the depth estimates and N is the number of hourly estimates.

Once a daily bathymetry estimate is made, bulk statistics for the daily beach profiles can be evaluated. The performance of the depth inversion was measured by both the raw difference errors $D(y)$,

$$D(y) = \hat{h}(y) - h_t(y) \tag{5.2}$$

and the relative errors $R(y)$,

$$R(y) = \frac{\hat{h}(y) - h_t(y)}{h_t(y)} \tag{5.3}$$

where h_t is the actual bathymetry value as measure by the kayak surveyor. The mean difference error, $\bar{D}$,

$$\bar{D} = \frac{1}{N} \sum_{i=1}^{N} D(y_i) \tag{5.4}$$

and mean relative error, $\bar{E}$,

$$\bar{R} = \frac{1}{N}\sum_{i=1}^{N} R(y_i) \tag{5.5}$$

can be determined across the entire profile, where N is the number of estimates.

The last statistical error used to analyze the performance of the depth inversion is the root-mean-square (rms) of the raw differences, D_{rms},

$$D_{rms} = \sqrt{\frac{1}{N}\sum_{i=1}^{N} D(y_i)^2} \tag{5.6}$$

and the rms of the relative errors, R_{rms},

$$R_{rms} = \sqrt{\frac{1}{N}\sum_{i=1}^{N} R(y_i)^2} \tag{5.7}$$

The rms error is useful in determining the scatter of the mean errors across the entire profile.

5.3.2 Evaluation of Depth Inversion Results

Hourly depth estimates at each compact pixel array from Oct 1st, 2008 at 13:36 GMT and 20:53 GMT are shown in the top two panels of Figure 5.8. All of the depth estimates for the entire day are shown in the bottom panel of Figure 5.8. The depth estimates are shown in comparison to the beach profile taken with the kayak surveyor the same day, Oct 1st, 2008. It is evident from Figure 5.8 that the WDM depth inversion is predicting the general trend of the beach profile, with a scattering of depth estimates around the actual profile. The scattering appears to increase offshore. The depth inversion results from Sep 30th, 2008 (Figure 5.9) appear very similar to the Oct 1st results with similar amounts of scatter about the actual water depth.

The mean and median daily beach profiles, $\hat{h}$, calculated from the hourly depth estimates, h_i, from October 1st and September 30th are shown in Figure 5.10. In addition, the 95% confidance interval at each cross-shore location has been plotted in Figure 5.10.

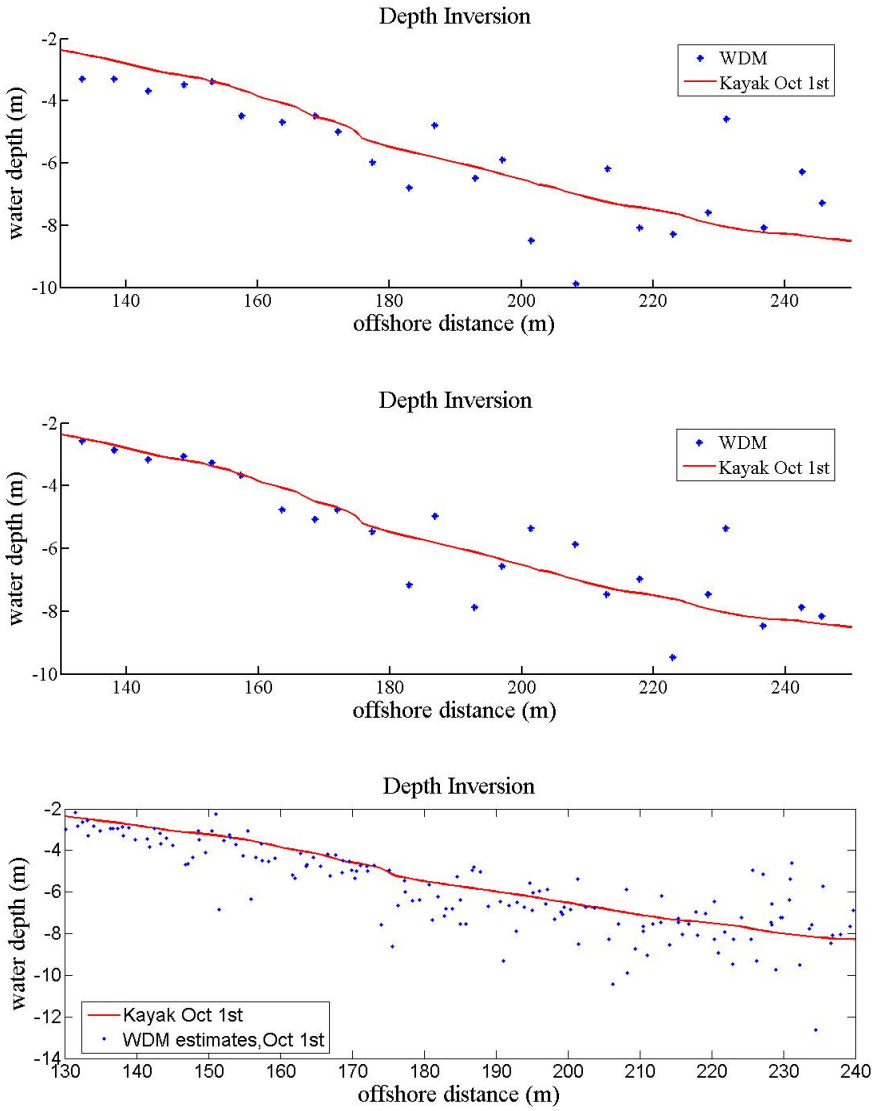

Figure 5.8: Comparison of hourly depth-inversion results from October 1st, 2008, to actual depths measured by the kayak surveyor. The top and middle panels show the depth inversion results from 13:36 GMT an 20:53 GMT respectively. The bottom panel shows all of the hourly depth estimates take during the day.

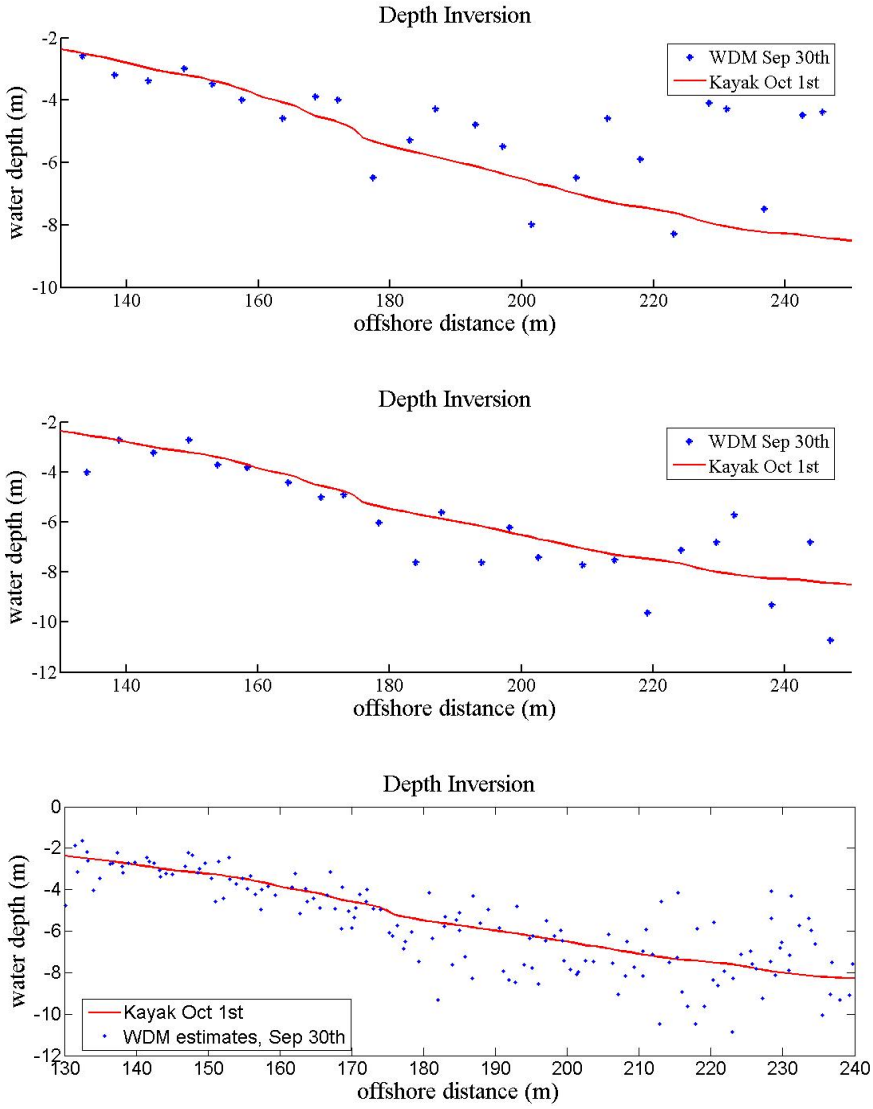

Figure 5.9: Comparison of hourly depth-inversion results from September 30th, 2008, to actual depths measured by the kayak surveyor. The top and middle panels show the depth inversion results from 13:36 GMT an 21:54 GMT respectively. The bottom panel shows all of the hourly depth estimates take during the day.

On both days, the mean and median beach profiles appear, in general, to slightly overpredict the water depth. It is also apparent from the confidence intervals that the accuracy of the inversion degrades offshore. An interesting feature present in the estimated beach profiles is the apparent but false sandbars. The actual survey show that these features are a result of the depth inversion algorithm, and may be related to the compact pixel array design.

The performance of the video-based mean and median daily beach profiles is best described by the bulk statistical properties outlined in Section 5.3. Table 5.1 lists the statistical results from Sept 30th and Oct 1st. The mean difference error $\bar{D}$ for all daily profiles ranges from -0.161 meters to -0.354 meters. This corresponds to a slight overprediction of the water depth in general. A study performed by *Grilli* (1998) found that errors from estimating the depth based solely on the linear dispersion relation can be as large as 50-70%. These errors are related to nonlinear wave affects, and currents, which if neglected cause an overprediction of the water depth.

Table 5.1: Accuracy of Depth Estimates for Sept 30th and Oct 1st

Test Date	Daily Statistical Method	Mean Difference Error $\bar{D}$, m	RMS Difference Error D_{rms}, m	Mean Relative Error $\bar{R}$	RMS Relative Error R_{rms}
Sep. 30th, 2008	Mean	-0.161	0.621	0.041	0.098
Sep. 30th, 2008	Medium	-0.195	0.587	0.043	0.098
Oct. 1st, 2008	Mean	-0.354	0.623	0.088	0.130
Oct. 1st, 2008	Medium	-0.269	0.572	0.072	0.117

The root-mean-square difference error, D_{rms}, ranged from 0.572 meters to 0.627 meters. The relative root-mean-square error, R_{rms}, ranged from 0.098 to 0.130. There appears to be a a negligible difference between the mean and median beach profiles. However, if the poor data files had not been removed from the data series then the median beach profile would have outperformed the mean profile and yielded a more stable and robust result. In addition, the performance of the depth inversion is comparable for the two days. This result is expected since the wave conditions were very similar on both

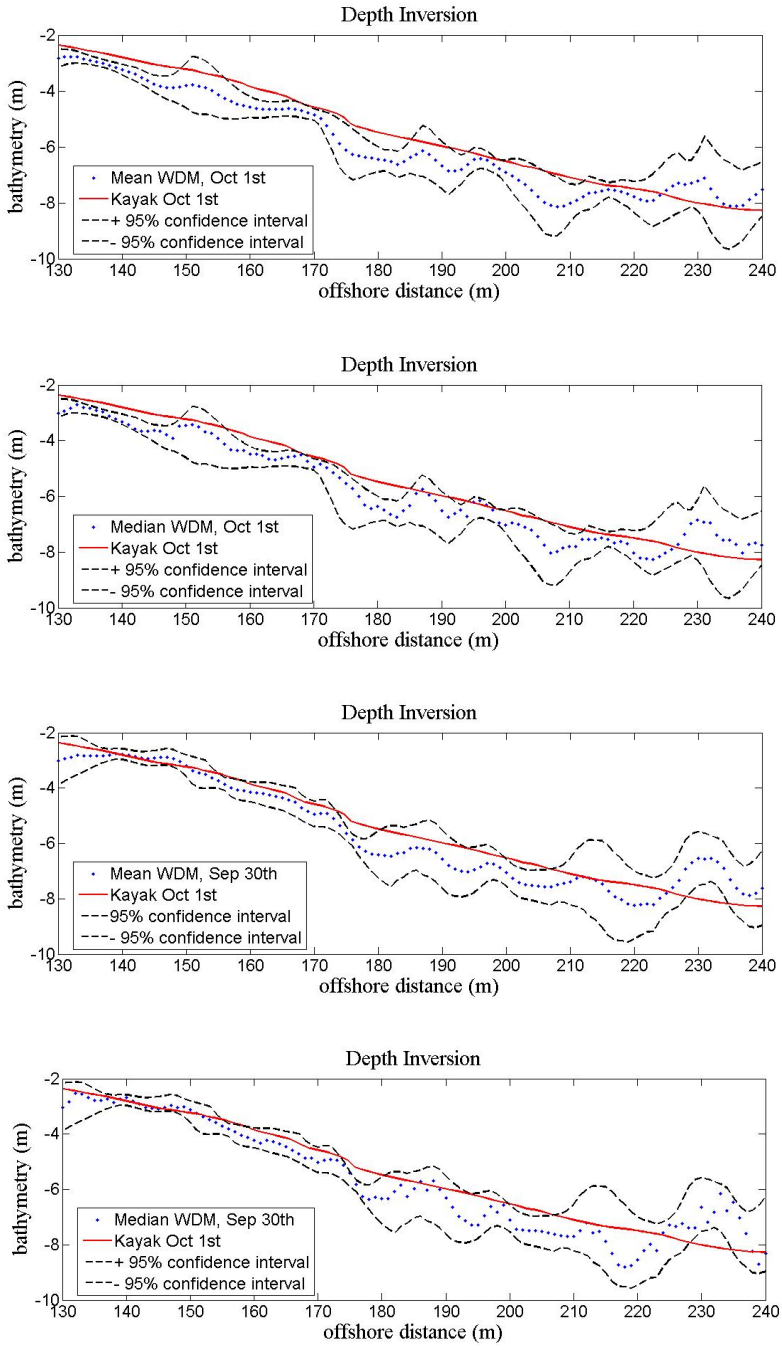

Figure 5.10: Comparison of the mean and median daily depth profiles from Oct 1st, 2008, and Sept 30th, 2008, to the actual water depth. The 95% confidence intervals are shown with dashed black lines.

days. It is reasonable to use the actual bathymetry on Oct 1st for comparison on Sept 30th, since the beach profile is not expected to change significantly over a non-energetic wave day.

In order to investigate whether or not there are any cross-shore or depth biases in the results, the root-mean-sqaure difference error and relative error at each cross-shore postion was calculate (top and middle panels of Figures 5.11 and 5.12. Both days show specific locations with large root-mean-sqaure errors. However, the location of large errors vary from September 30th to October 1st, suggesting that the biases are solely related to pixel locations of the compact arrays. The top and bottom panels of Figure 5.12 show that the error magnitude of the depth errors increase offshore. However, the middle panel shows that the relative error is independent of how far offshore the compact array is.

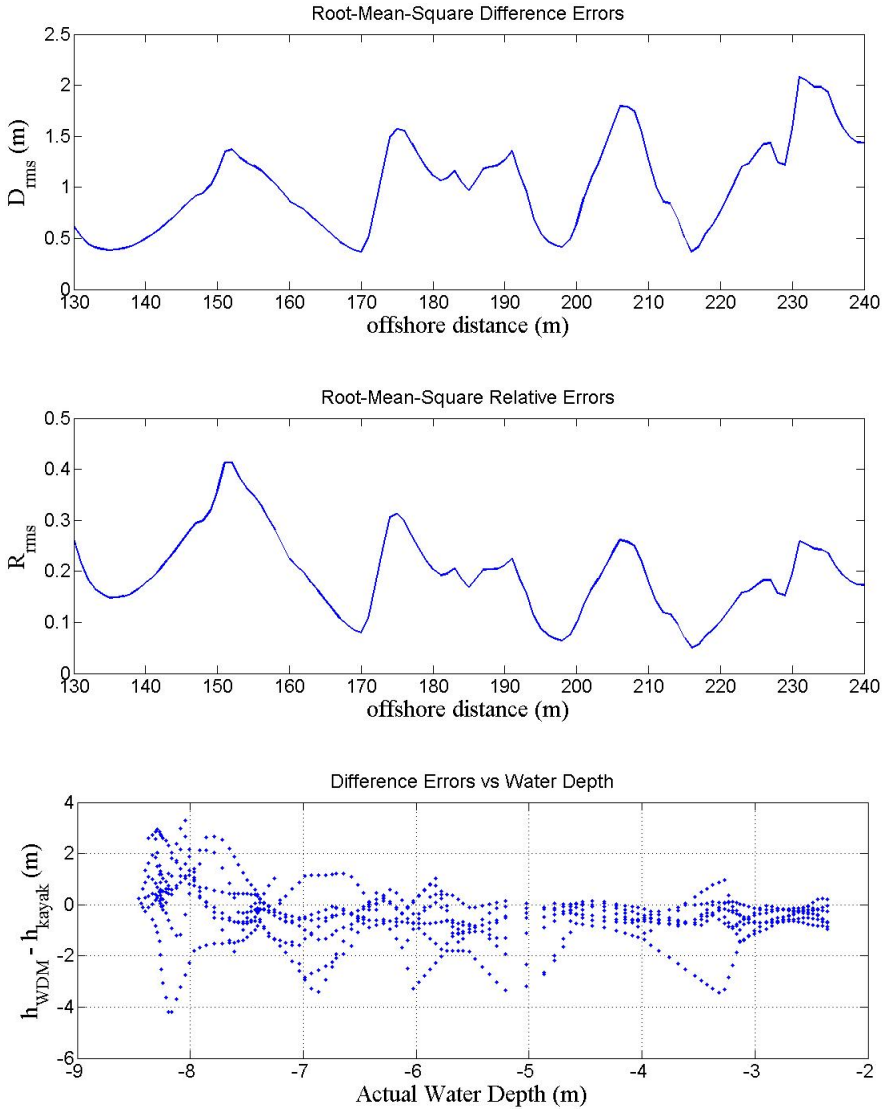

Figure 5.11: The top and middle panels show the root-mean-square difference errors and relative errors respectively for October 1st, 2008. The bottom panel shows the difference errors relative to the actual water depth

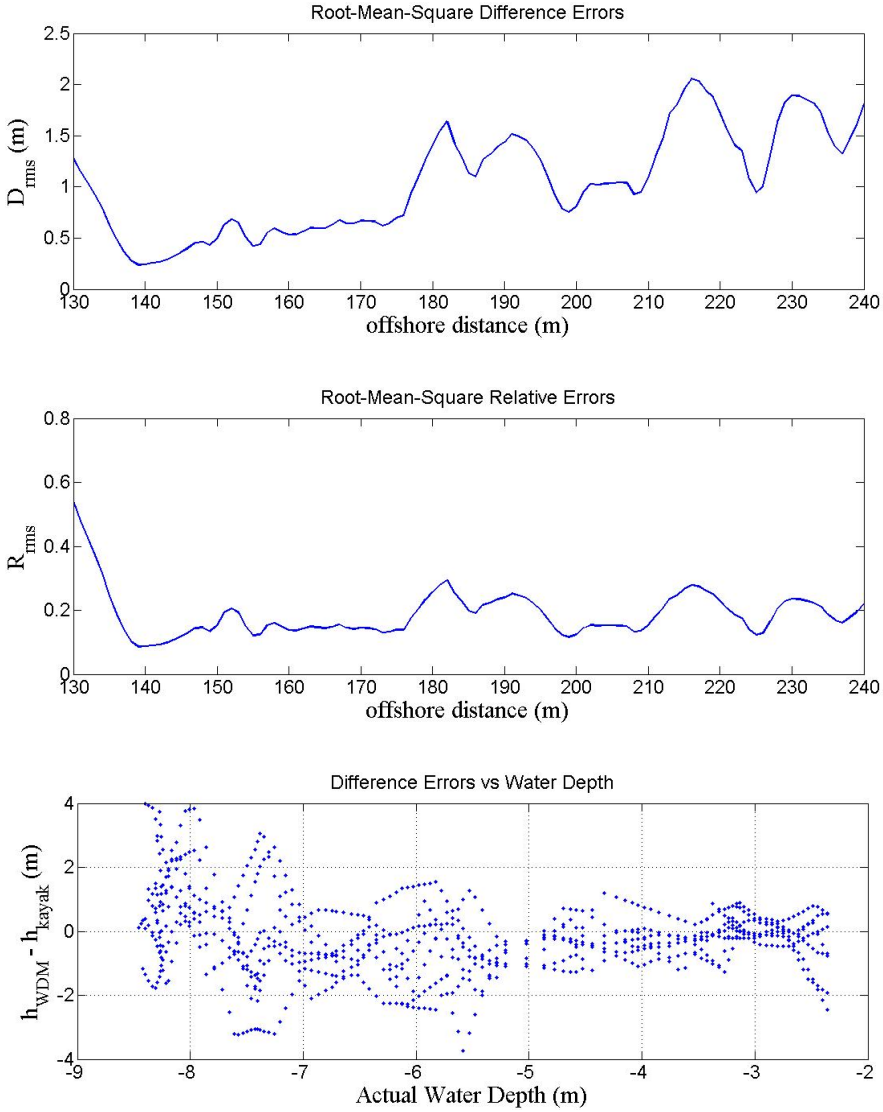

Figure 5.12: The top and middle panels show the root-mean-square difference errors and relative errors respectively for September 30th, 2008. The bottom panel shows the difference errors relative to the actual water depth

Chapter 6

CONCLUSIONS

A new technique has been developed for the estimation of nearshore water depths from video images. The new technique extends the WDM to compact arrays of pixel intensity time series. By extending the WDM, the directional spectrum and frequency-wavenumber spectrum can be estimated at each compact array. Unfortunately, the magnitude of the directional spectrum can not be determined solely from the pixel intensity time series. However, the directional and frequency spreading of wave energy can be determined. Estimates of the magnitude of the video-based directional spectrum could be obtained from comparison to a refracted and shoaled power spectrum of a nearby slope array or heave-pitch-roll buoy.

The water depth can be estimated by fitting the linear dispersion relation to the frequency-wavenumber spectrum at each compact pixel array location. The combination of the directional spectrum and water depth estimates at a series of compact arrays extending offshore allows for the transformation of waves from deep water to shallow water to be observed. Additionally, any variations in the directional spreading of wave energy from morphological features, could in theory, be estimated from the video-based directional sprectra.

Daily averaged profiles based on the mean and medium of hourly depth estimates were shown to yield good agreement with the actual bathymetry measured by the kayak surveyor. Root-mean-square errors (D_{rms}) as low as 0.57 meters were obtained from the daily average bathymetry profiles. The increase in root-mean-square errors offshore may

be attributable to the increase in the spatial footprint of a pixel. This shortens the distance between pixels in the raw image, making it more difficult to determine a statistically significant phase lag (*Stockdon and Holman*, 2000). In general, the depth inversion over predicts the water depth. Previous linear dispersion based depth inversions have also over predicted the water depth (*Stockdon and Holman*, 2000). Therefore, it is suggested that a nonlinear dispersion relation, such as Stokes 3rd order dispersion relation, be fitted to the frequency-wavenumber spectrum using the H_{mo} wave height from the slope array.

The WDM depth inversion procedure is affected by environmental conditions such as rain, fog, and sun glare that reduce the visibility of wave crests. A limitation of the WDM procedure is that during large storm conditions, resonant foam, and white caps distort the phase information contained in the pixel intensity values. Results from partly cloudy days, showed that the depth inversion procedure was adversely affected by sharp jumps in the pixel intensity time series resulting from shadows.

For future work, the performance of the WDM depth inversion should be compared to higher quality data, for example at the Argus station in Duck, NC. Additional future work needs to be performed to evaluate the performance of different pixel array shapes and determine if there are any biases present. More robust depth estimates could be obtained inside the surfzone by removing remnant foam (*Yoo et al.*, 2008). A field study should be performed for a longer duration to determine the suitability to applying the WDM depth inversion procedure in variety of wave conditions.

Bibliography

(2004), *Corpscon Version 6.x: Technical Documentation and Operating Instructions*, U.S. Army Corps of Engineers: Engineering Research and Development Center, Alexandria, Virginia.

Adler-Golden, S. M., P. K. Acharya, A. Berk, M. W. Mathher, and D. Gorodetzky (2005), Remote bathymetry of the littoral zone from aviris, lash, and quickbird imagery, *IEEE Transactions on Geoscience and Remote Sensing*, *43*(2), 337–347.

Antoine, J. P. (1998), The continuous wavelet transform in image processing.

Beach, R. A., R. A. Holman, and J. Stanley (), Measuring nearshore bathymetry on high energy beaches, American Geophysical Union Fall Meeting. San Francisco, 1994.

Bell, P. S. (1999), Shallow water bathymetry derived from an analysis of x-band marine radar images of waves, *Coastal Engineering*, *37*, 513–527.

Brissette, F. P., and I. K. Tsanis (1994), Estimation of wave directional spectra from pitch-roll buoy data, *Journal of Waterway, Port, Coastal, and Ocean Engineering*, *120*(1), 92–115.

Capon, J. (1960), High-resolution frequency-wavenumber spectrum analysis, in *Proceedings of the IEEE, 57*.

Dalrymple, R. A., A. B. Kennedy, J. T. Kirby, and Q. Chen (1998), Determining depth from remotely-sensed images, in *Coastal Engineering 1998: Proceedings of the 26th International Conference*, pp. 2,395–2,408.

Davis, R. E., and L. A. Regier (1977), Methods for estimating directional wave spectra from multi-element arrays, *Journal of Marine Research*, *35*(1534), 453–477.

Dean, R. G., and R. A. Dalrymple (1991), *Water Wave Mechanics for Engineers and Scientists*, World Scientific, Hackensack, NJ.

DeMunda, T. J. (2006), A system for video observation of nearshore processes, Master's thesis, University of Delaware, Newark.

Donelan, M. A., W. M. Drennan, and A. K. Magnusson (1996), Nonstationary analysis of the directional properties of propagating waves, *Journal of Physical Oceanography*, *26*, 1901–1914.

Dugan, J. P., K. C. Vierra, W. D. Morris, G. J. Farruggia, and D. C. Campion (1999), Unique vehicles used for bathymetry surveys in exposed coastal regions, in *Proceedings, U.S. Hydrographic Conference Society National Meeting*.

Dugan, J. P., C. C. Piotrowski, and J. Z. Williams (2000), Water depth and surface current retrievals from airborne optical measurements of surface gravity wave dispersion, *Journal of Geophysical Research*, *106*(C8), 16,903–16,915.

Farge, M. (1992), Wavelet transforms and their applications to turbulence, *Annual Review of Fluid Mechanics*, *24*, 395–457.

Greenberg, M. D. (1988), *Advanced Engineering Mathematics*, Prentice-Hall, Englewood Cliffs, NJ.

Grilli, S. T. (1998), Depth inversion in shallow water based on nonlinear properties of shoaling periodic waves, *Coastal Engineering*, *35*, 185–209.

Holland, K. T. (2001), Application of the linear dispersion relation with respect to depth inversion and remotely sensed imagery, *IEEE Transactions on Geoscience and Remote Sensing*, *39*(9), 2060–2072.

Holland, K. T., J. A. Puleo, and T. N. Kooney (2001), Quantification of swash flows using video-based particle image velocimetry, *Coastal Engineering*, *44*, 65–77.

Holland, T. K., R. A. Holman, T. C. Lippman, J. Stanley, and N. Plant (1997), Practical use of video imagery in nearshore oceanographic field studies, *IEEE Journal of Oceanic Engineering*, *22*(1), 81–92.

Holman, R. A., and J. Stanley (2007), The history and technical capabilities of argus, *Coastal Engineering*, *54*, 477–491.

Irish, J. L. (2005), Lidar applications for coastal engineering: Sea bottom mapping and water wave measurement, Ph.D. thesis, University of Delaware, Newark, Delaware 19716.

Isobe, M., K. Kondo, and K. Horikawa (1984), Extension of mlm for estimating directional wave spectrum, pp. 1–15, Symposium on Description and Modelling of Directional Seas, Tech. University, Denmark.

Kean, R. D., and R. J. Adrian (1992), Theory of cross-correlation analysis of piv images., *Applied Science Research*, *49*(191).

Krogstad, H. E., A. K. Magnusson, and M. A. Donelan (2006), Wavelet and local directional analysis of ocean waves, *International Journal of Offshore and Polar Engineering*, *16*(2), 97–103.

Kronland-Martinet, R., J. Morlet, and A. Grossmann (1987), Analysis of sound patterns through wavelet transforms, *International Journal of Pattern Analysis and Artificial Intelligence*, *1*(2), 273–302.

Lippmann, T. C., and R. A. Holman (1991), Phase speed and angle of breaking waves measured with video techniques, in *Proceedings Coastal Sediments'91*, pp. 542–556.

Liu, P. C. (1999), Wavelet transform and new perspective on coastal and ocean engineering data analysis, in *Advances in Costal and Ocean Engineering Vol. 3*, pp. 57–101, World Scientific.

Longuet-Higgins, M. S., D. E. Cartwright, and N. D. Smith (1962), Observations of the directional spectrum of sea waves using the motions of a floating buoy, in *Ocean Wave Spectra*, pp. 111–132, Prentice-Hall, Englewood Cliffs, N.J.

Lynch, D. K., and W. Livingston (2001), *Color and Light in Nature*, 2nd ed., Cambridge University Press, New York, New York.

Lyzenga, D. R., N. P. Malinas, and F. J. Tanis (2006), Multispectral bathymetry using a simple physically based algorithm, *IEEE Transactions on Geoscience and Remote Sensing*, *44*(8), 2251–2259.

MacMahan, J. (2001), Hydrographic surveying from personal watercraft, *Journal of Surveying Engineering*, *127*(1), 12–24.

McGregor, J. A., E. M. Poulter, and M. J. Smith (1998), S band doppler radar measurements of bathymetry, wave energy fluxes, and dissipation across an offshore bar, *Journal of Geophysical Research*, *103*(C9), 18,779–18,789.

Misra, S. K., A. B. Kennedy, and J. T. Kirby (2003), An approach to determining nearshore bathymetry using remotely sensed ocean surface dynamics, *Coastal Engineering*, *47*, 265–293.

Newland, D. E. (1993), *An Introduction to Random Vibrations, Spectral and Wavelet Analysis*, Dover Publications, Mineola, NY.

Oltman-Shay, J., and R. T. Guza (1984), A data-adaptive ocean wave directional-spectrum estimator for pitch and roll type measurements, *Journal of Physical Oceanography*, *14*, 1800–1810.

Plant, N. G., K. T. Holland, and M. C. Haller (2008), Ocean wavenumber estimation from wave-resolving time series imagery, *IEEE Transactions on Geoscience and Remote Sensing*, *46*(9), 1–16.

Saeki, M., and M. Hori (2006), Development of an accurate positioning system using low-cost l1 gps receivers, *Computer-Aided Civil and Infrastructure Engineering*, *21*, 258–267.

Stockdon, H. F., and R. A. Holman (2000), Estimation of wave phase speed and nearshore bathymetry from video imagery, *Journal of Geophysical Research*, *105*(C9), 22,015–22,033.

Walker, R. E. (1994), *Marine Light Field Statistics*, John Wiley and Sons, Inc., New York, NY.

Williams, W. W. (1946), The determination of gradients of enemyheld beaches, *Geographic Journal*, *107*, 76–93.

Wright, L. D., and A. D. Short (1984), Morphodynamic variability of surf zones and beaches: A synthesis, *Marine Geology*, *56*, 93–118.

Yoo, J. H., K. Haas, P. Work, and C. Barnes (2008), Estimation of breaking wave celerity via oblique digital nearshore videography, *Coastal Engineering*, (in review).

Appendix A

TIME SERIES ANALYSIS TECHNIQUES

A.1 Fourier Transform

The Fourier transform plays an essential role in so many time series analysis techniques used throughout this paper that an informal definition is given here. A rigorous derivation is provided by *Greenberg* (1988) and *Newland* (1993). The basic idea behind Fourier analysis is that any piecewise continuous signal can be decomposed into even and odd waves at a set of frequencies. The Fourier series of a periodic function is given as

$$f(t) = \sum_{n=0}^{\infty}(a_n \cos n\omega t + b_n \sin n\omega t) \tag{A.1}$$

$$a_0 = \frac{1}{T}\int_t^{t+T} f(t)dt \tag{A.2}$$

$$a_n = \frac{2}{T}\int_t^{t+T} f(t)\cos n\omega t dt, n = 1, 2, ..., \infty \tag{A.3}$$

$$b_n = \frac{2}{T}\int_t^{t+T} f(t)\sin n\omega t dt, n = 1, 2, ..., \infty \tag{A.4}$$

where T is the length of the periodic interval, $\omega = \frac{2\pi}{T}$, a_0 is the mean of the signal, a_n are the even components and b_n are the odd components at given frequency, $\frac{n}{T}$. Using Euler's identities, the Fourier transform pair can be defined as

$$f(t) = \sum_{n=-\infty}^{\infty} F(n)e^{in\omega t} \tag{A.5}$$

$$F(n) = \frac{1}{T}\int_t^{t+T} f(t)e^{-in\omega t}dt \tag{A.6}$$

The even and odd components of Fourier transform, $F(n)$, are given by

$$F(n) = \frac{a_n - ib_n}{2},\ n \geq 0 \tag{A.7}$$

$$F(n) = \frac{a_n + ib_n}{2},\ n < 0 \tag{A.8}$$

The phase ϵ_n of the signal at a given frequency can be determined from the relationship between the even and odd components as

$$\epsilon_n = \tan^{-1}(\frac{b_n}{a_n}) \tag{A.9}$$

In practice the Fourier transform is computed by taking advantage of Fast Fourier Transform (FFT) algorithms available.

A.2 Correlation and Covariance Function

The correlation function and covariance function are both essential tools in time series analysis and are used throughout this paper in the development of other time series techniques. The correlation function measures how similar two functions are or their total correlation at each time lag, τ. The correlation function, $X_{ij}(\tau)$, is the convolution of two signals, f_i and f_j and is given by

$$X_{ij}(\tau) = \frac{1}{T}\int_t^{t+T} f_i(t) f_j^*(t+\tau)dt \tag{A.10}$$

where T is the length of the time series. Alternatively the correlation function can be written in Fourier components and the phase as

$$X_{ij}(\tau) = \sum_{n=-\frac{N}{2}}^{\frac{N}{2}} F_j(n) F_i^*(n) e^{in\omega\tau} \tag{A.11}$$

$$X_{ij}(\tau) = \sum_{n=-\frac{N}{2}}^{\frac{N}{2}} |F_j(n)||F_i(n)| e^{i(\epsilon_j - \epsilon_i)} e^{in\omega\tau} \tag{A.12}$$

where $F_i(n)$ is the Fourier transform of $f_i(t)$ and N is the number of points in the time series. From the definitions above of $X_{ij}(\tau)$ it can be seen that the total correlation can be calculate on a frequency by frequency basis where the correlation is based on two parts: the magnitude of the Fourier coefficients and the relative phase difference of the Fourier components. Therefore, the correlation will be highest when the Fourier coefficients are in phase and high as well.

The description of the correlation function leads directly into the definition of the covariance function, which is defined as the Fourier transform of the correlation function. The covariance function is written as

$$\Phi_{ij}(n) = \frac{1}{T}\int_t^{t+T} X_{ij}(\tau)e^{-in\omega\tau}d\tau = F_i^*(n)F_j(n) \tag{A.13}$$

Since the Fourier transform decomposes a signal into amplitude and phase information at a range of frequencies the Covariance function contains the variance and phase difference between $f_i(t)$ and $f_j(t)$ at a given frequency as clearly shown in the equation above. The phase difference between to signals at a given frequency is given by

$$\Delta\epsilon(n) = \epsilon_j - \epsilon_i = \tan^{-1}(\frac{-Im\{\Phi_{ij}(n)\}}{Re\{\Phi_{ij}(n)\}}) \tag{A.14}$$

One practical use of the covariance function is that the auto-covariance of a signal is directly related to its power spectrum or energy spectrum as it is often called in ocean wave analysis. Here the auto-variance is given by

$$\Phi_{ii}(n) = F_i^*(n)F_i(n) = |F_i(n)|^2 \tag{A.15}$$

and the power spectrum is given as

$$S(\omega_n) = 2N\Delta t|F_i(w_n)|^2 \tag{A.16}$$

where the power spectrum has been folded over so that only positive radial frequencies, $\omega_n = \frac{2\pi n}{T} \geq 0$, are included. Additionally, the power spectrum is scaled so that its integral over all frequencies equals the total variance, ς^2, of the time series.

$$\int_0^\infty S(\omega) dw = \varsigma^2 \tag{A.17}$$

The reason why the power spectrum is called the energy spectrum is because the components of the power spectrum are squares of the wave amplitude at each frequency which are related to energy of wave because the energy of a wave is given by

$$E = \frac{1}{8}\rho g H^2 \tag{A.18}$$

where E is the average energy of a wave per unit surface area, ρ is the density of the water, g is gravity and H is the wave height.

A.3 Wavelet Analysis

The wavelet transform is a relatively new mathematical technique developed in the late 1980's to decompose arbitrary, nonstationary signals into both space and scale. Previous data analysis techniques such as the Fourier transform utilize space-filling trigonometric functions to decompose a signal into just scale. The wavelet transform uses time-localized functions called wavelets, which are dilated, contracted and translated before convolving with the signal. Different choices for the analyzing wavelets exist, however all the wavelets exhibit a oscillating function with a decaying amplitude away from the center of the wavelet. Therefore, unlike the Fourier transform, the wavelet transform is capable of showing localized scale information of a signal. This makes the wavelet transform a powerful technique for data analysis of any signal in which local properties are dominant (*Kronland-Martinet et al.*, 1987).

Since its development the wavelet transform has been used in signal processing of sound patterns (*Kronland-Martinet et al.*, 1987), turbulent flows *Farge* (1992), non

stationary analysis of propagating waves (*Donelan et al.*, 1996), and image detection (*Antoine*, 1998). Here, one-dimensional wavelets and their application to the analysis of non-stationary water surface time series will be investigated. The theoretical development of the wavelet transform shown here closely follows *Krogstad et al.* (2006). Assume $\eta(t)$ to be a water surface time series, then its wavelet transform, $W(a,\tau)$, is the convolution of $\eta(t)$ and the chosen wavelet, $\psi(\frac{t-\tau}{a})$, and is given by

$$W(a,\tau) = \frac{1}{\sqrt{a}} \int_t^{t+T} \eta(t)\psi^*(\frac{t-\tau}{a})dt \tag{A.19}$$

where a and τ, are the scale and phase shift of the wavelet. The wavelet transform calculates the correlation between the wavelet and time signal at various scales and phase shifts. The requirements for the analyzing wavelet are that it has a zero average

$$\int_{-\infty}^{\infty} \psi(t)dt = 0 \tag{A.20}$$

and that the wavelet has a constant norm

$$||\psi(t)|| = \int_{-\infty}^{\infty} |\psi(t)^2|dt = 1 \tag{A.21}$$

There are numerous choices for the analyzing wavelet. A common choice for ocean wave analysis is the Morlet wavelet because it provides a good compromise between time and frequency localization. The 1-D Morlet wavelet, $\psi(t)$, and its Fourier transform, $\hat{\psi}(\omega)$, are given by

$$\psi(t) = \frac{1}{\pi^{\frac{1}{4}}} \frac{1}{\sqrt{\sigma_0}} e^{it} e^{-\frac{t^2}{2\sigma_0^2}} \tag{A.22}$$

$$\hat{\psi}(\omega) = \pi^{\frac{1}{4}} \sqrt{2\sigma_0} e^{-\frac{\sigma_0^2}{2}(1-\omega)^2} \tag{A.23}$$

where σ_0 controls the number of oscillations in the wavelet before it decays.

The Morlet wavelet can be thought of as function that oscillates for a little while like a wave, but is then localized by damping as shown by Figure 2.4. As σ_0 approaches ∞

the wavelet looks like a plane wave and as σ_0 approaches zero the wavelet becomes a delta function. The choice of σ_0 controls the balance between time and frequency resolution. The Fourier transform of the wavelet, $\hat{\psi}(\omega)$, is centered in the frequency domain at the frequency corresponding to the scale of the wavelet. It can be seen in Figure 2.4 that there is significant spreading of $\hat{\psi}(\omega)$ around its scale frequency. This loss of resolution is related the Heisenberg uncertaintity principle, which states that sharp localizations in time and frequency are mutually exclusive (*Liu*, 1999). Therefore, wavelets provide time localization at the cost of of a loss of frequency resolution.

Throughout this paper the scaling of the wavelets will be done by specifying the scale frequency of the wavelet, v_0. The corresponding definition of the scaled morlet wavelet and its Fourier transform are given by

$$\psi(t-\tau, v_0) = \frac{\sqrt{2\pi|v_0|}}{\pi^{\frac{1}{4}}\sqrt{\sigma_0}} e^{i2\pi v_0(t-\tau)} e^{-\frac{(2\pi v_0(t-\tau))^2}{2\sigma_0^2}} \tag{A.24}$$

$$\hat{\psi}(\omega, v_0) = \frac{1}{\pi^{\frac{1}{4}}} \sqrt{\frac{\sigma_0}{|v_0|}} e^{-\frac{\sigma_0^2}{|v_0|}\frac{(\frac{\omega}{2\pi}-v_0)^2}{2}} \tag{A.25}$$

The wavelet transform corresponding to the these definitions of the Morlet wavelet are

$$W(v_0, \tau) = \int_t^{t+T} \eta(t)\psi^*(t-\tau, v_0)dt \tag{A.26}$$

$$W(v_0, \tau) = \int \hat{\eta}(\omega)\hat{\psi}^*(\omega, v_0)e^{iw\tau}d\tau \tag{A.27}$$

In practice it is significantly faster computationally to calculate the wavelet transform in the Fourier domain. Therefore, throughout this study the wavelet transform was computed in the Fourier domain.

A simple example of the usefulness of wavelets is given by applying the wavelet transform to a non-stationary time signal. The time signal for this example is chirp, shown in the top panel of Figure A.1, and given by

$$\eta(t) = \cos(wt^2) \tag{A.28}$$

where $w = 0.0063$ for this example. The dominant feature of the chirp time signal is the increase in the frequency of the time signal over time. The real-part of the wavelet transform (middle panel of Figure A.1) and modulus (bottom panel of Figure A.1) show the change in the frequency of the time signal over time. It is also evident that the phase information of the time signal is retained in the both the real and imaginary parts of the wavelet transform.

In essence the wavelet transform at a single scale contains the phase information of any waves present in the time series at the scale frequency of the wavelet. However, energetic waves at nearby frequencies can be leaked into the wavelet transform. This effect can be seen in Figure A.2, where the top panel shows the real and imaginary parts of the wavelet transform at a scale frequency of 0.2 Hz. The middle and bottom panel in Figure A.2 show the resulting phase of wavelet transform and the phase gradient. The phase gradient measures the actual frequency of the time signal retained in the wavelet transform.

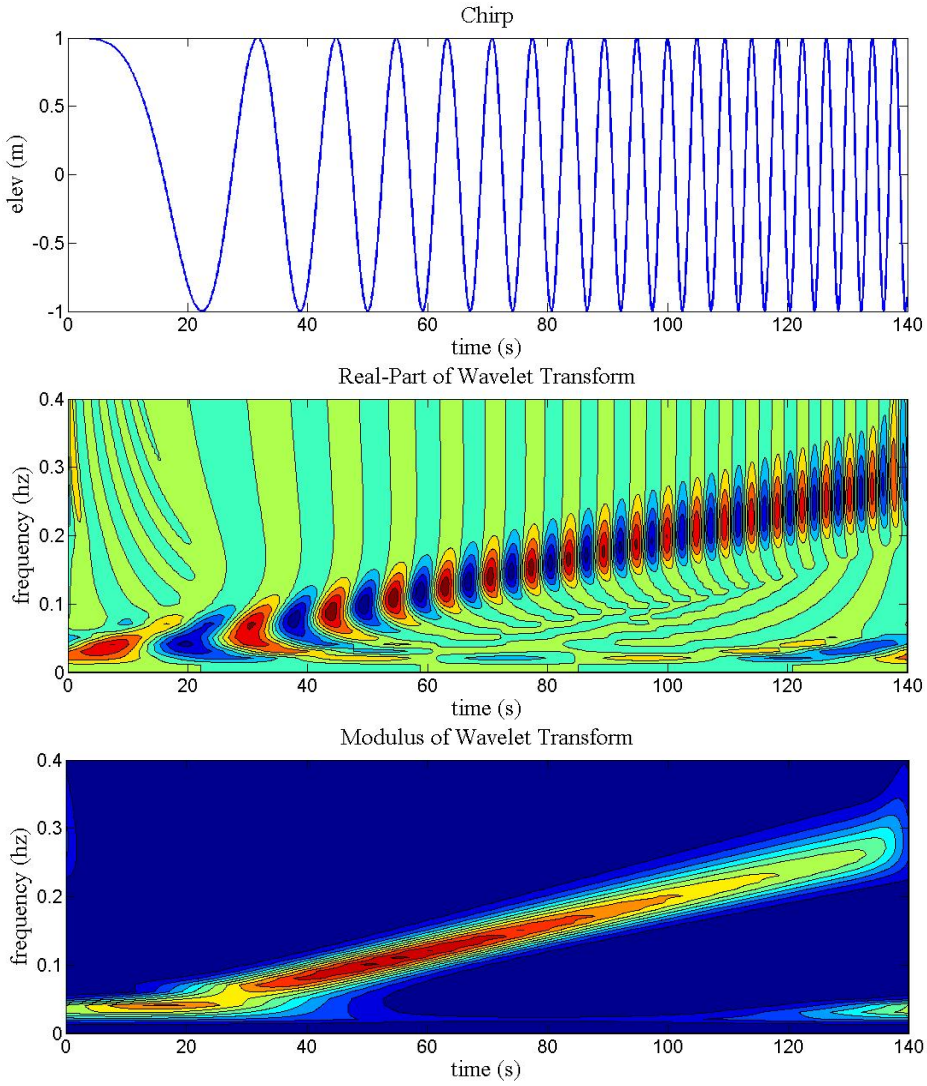

Figure A.1: The top panel shows the time signal of a chirp, where the it is evident that the frequency increase with time. The middle panel is the wavelet transform of the chirp signal. The bottom panel shows the modulus of the wavelet transform. It is evident from the wavelet transform and its modulus that the time signals frequency is increasing with time.

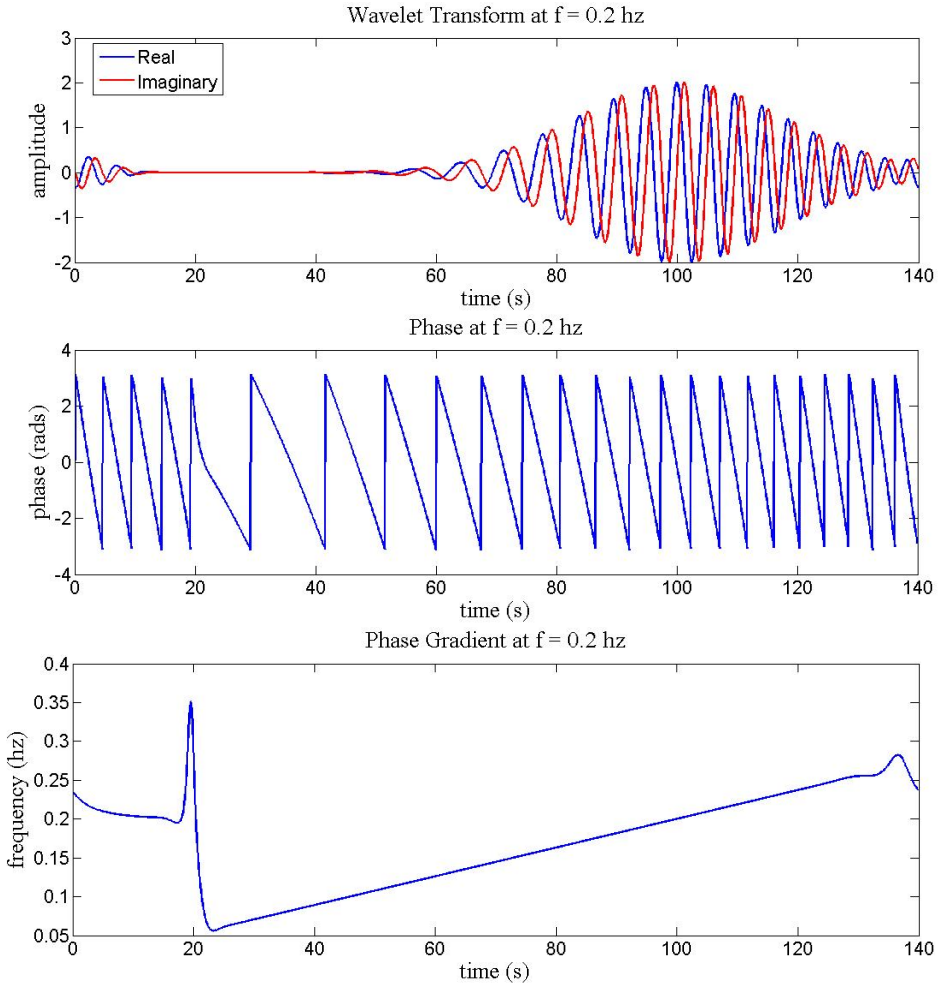

Figure A.2: The top panel shows the real and imaginary parts of the wavelet transform at single scale frequency (0.20 Hz). The middle panel shows the phase of the wavelet transform components. The bottom panel shows the gradient of the phase, which is the frequency of the wavelet transform filtered time signal.

Appendix B

DIRECTIONAL SPECTRUM RESULTS FROM PIXEL ARRAY

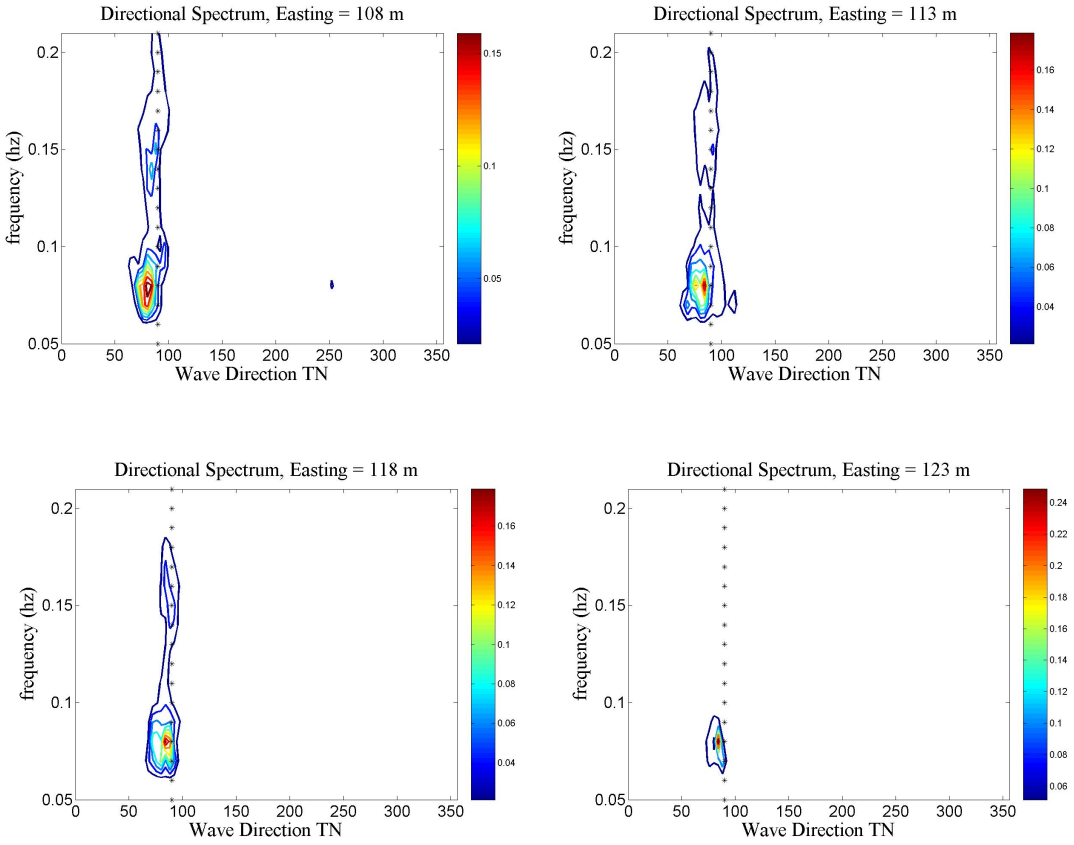

Figure B.1: Directional spectrum estimates from compact pixel arrays of easting 108m to 123m. Oct 1st, 2008, 13:36 GMT

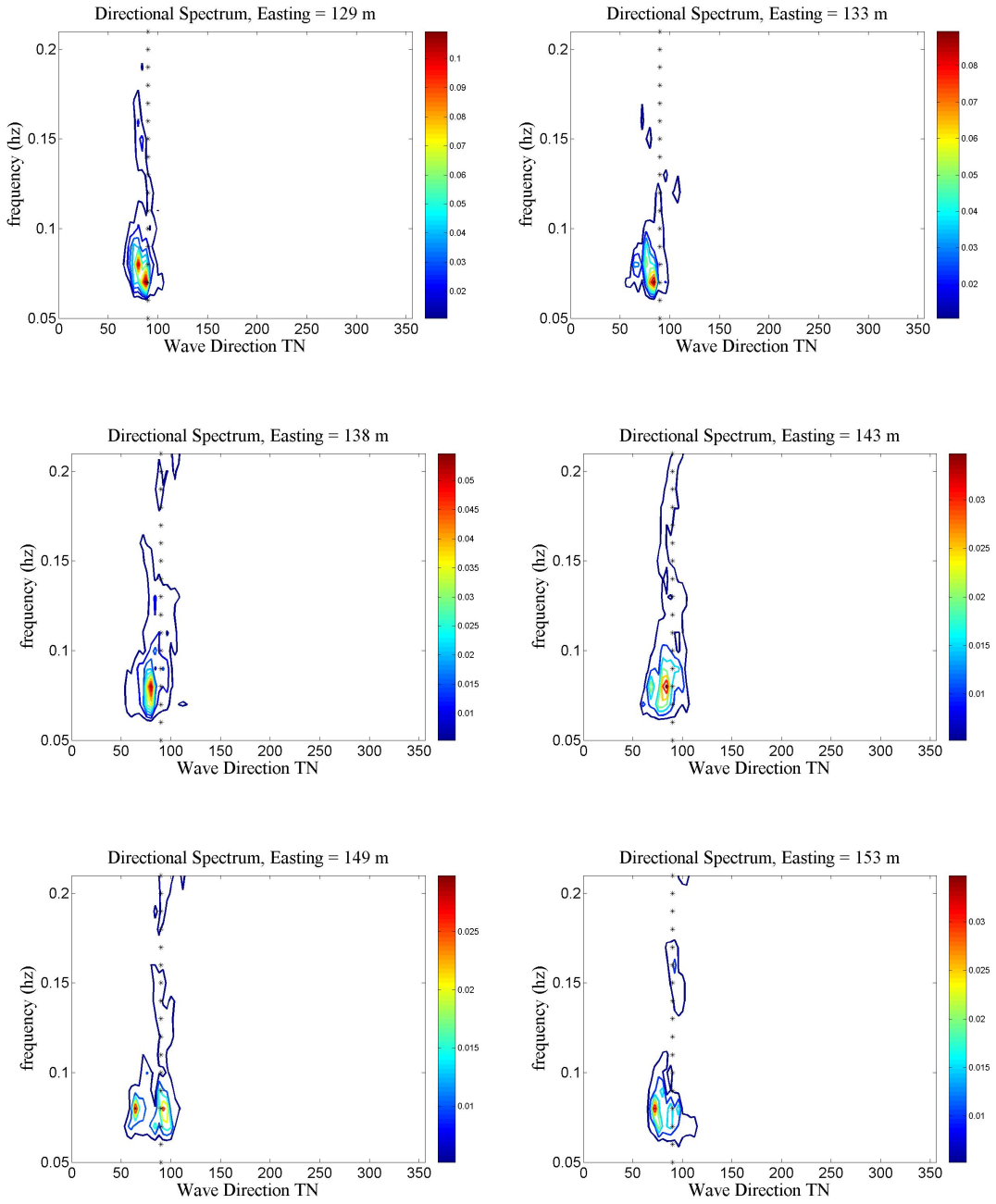

Figure B.2: Directional spectrum estimates from compact pixel arrays of easting 129m to 153m. Oct 1st, 2008, 13:36 GMT

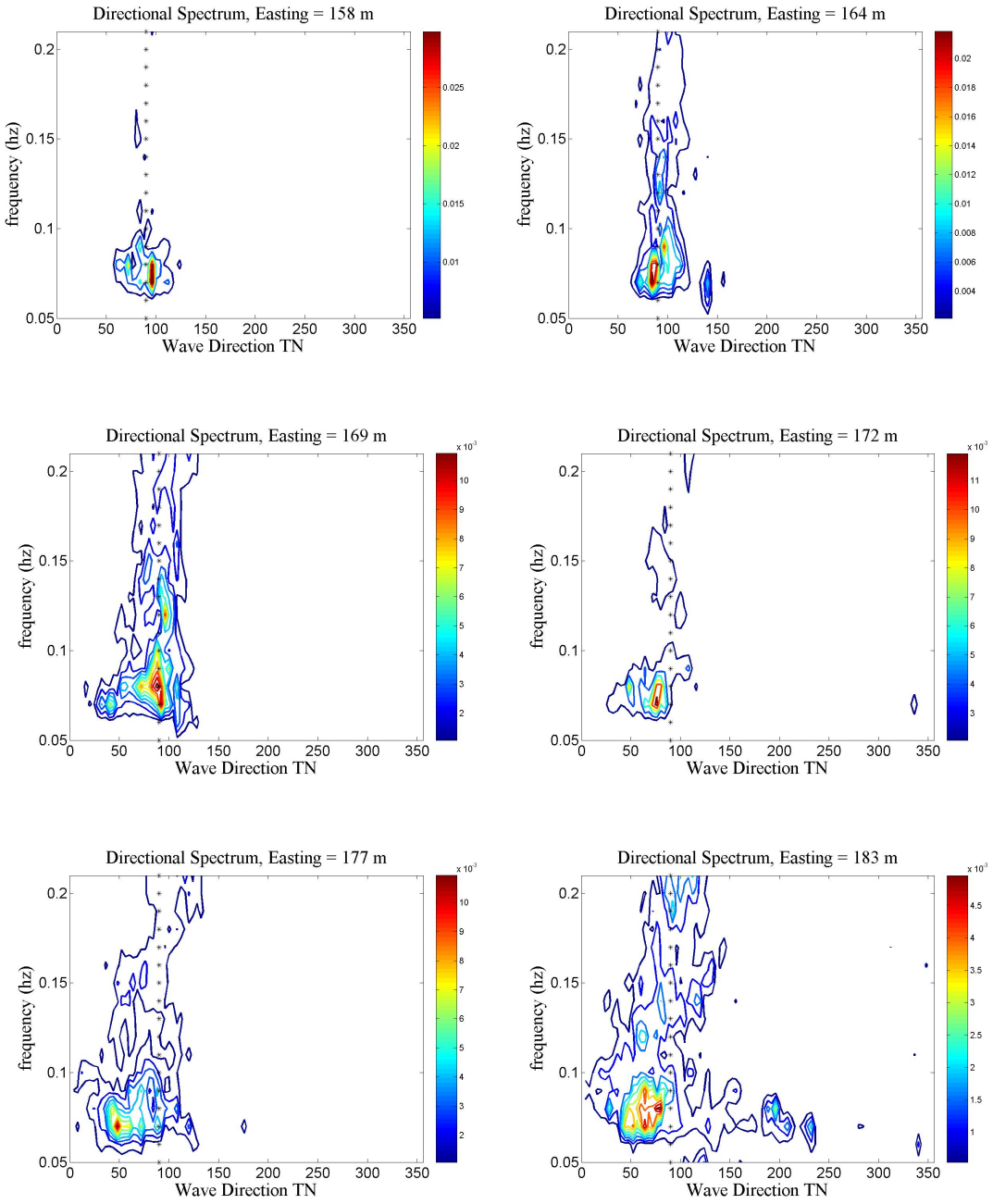

Figure B.3: Directional spectrum estimates from compact pixel arrays of easting 158m to 183m. Oct 1st, 2008, 13:36 GMT

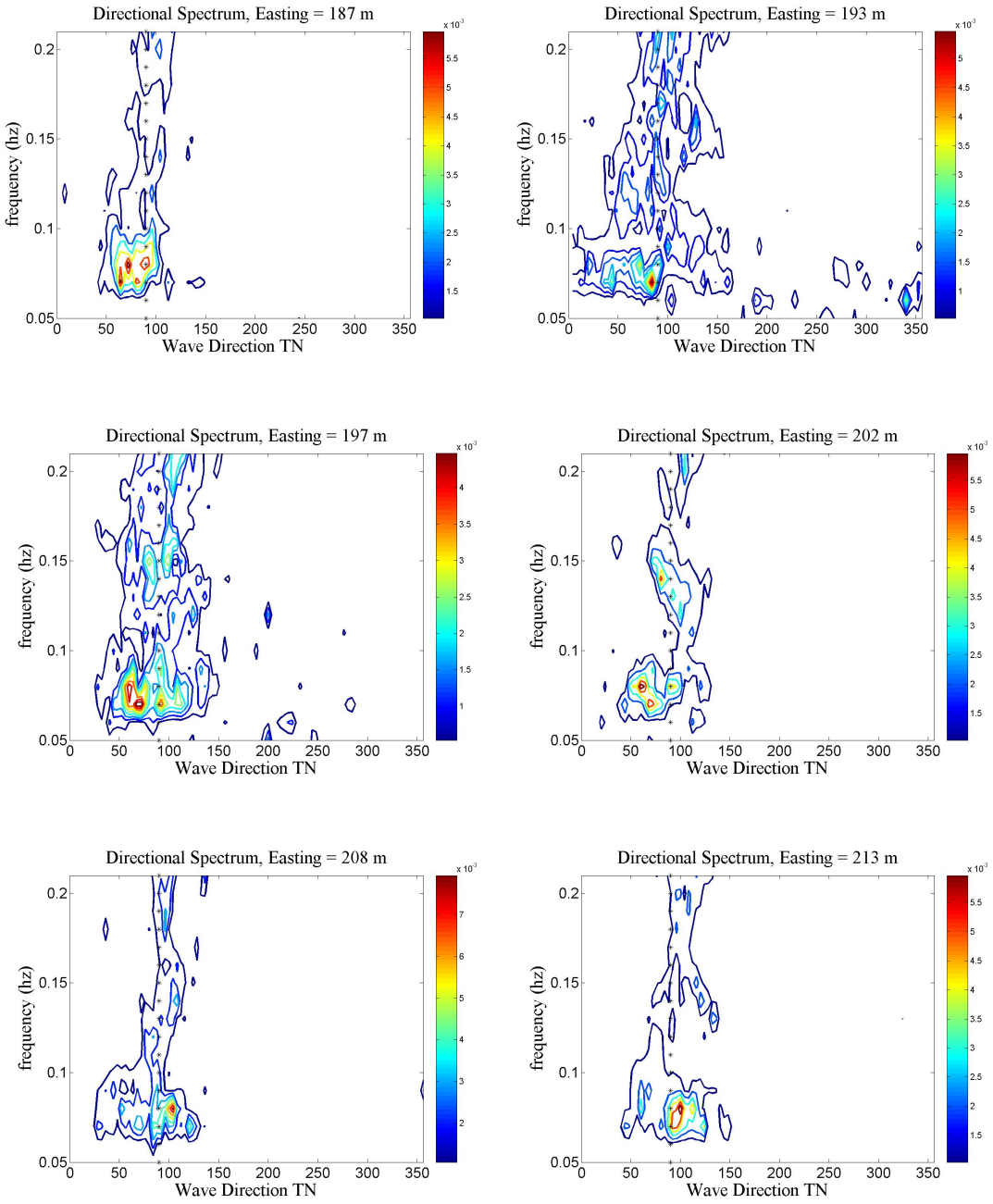

Figure B.4: Directional spectrum estimates from compact pixel arrays of easting 187m to 213m. Oct 1st, 2008, 13:36 GMT

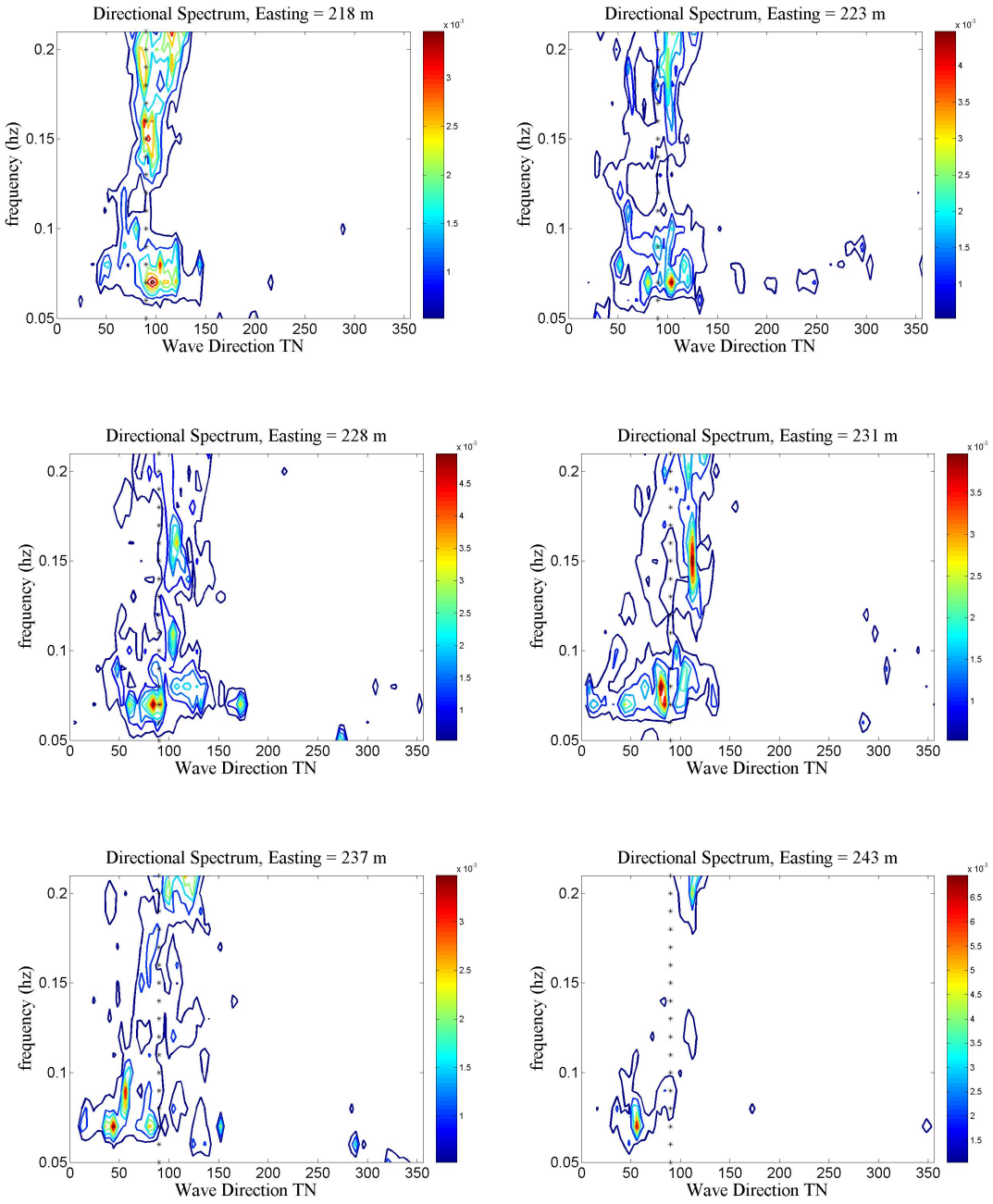

Figure B.5: Directional spectrum estimates from compact pixel arrays of easting 218m to 243m. Oct 1st, 2008, 13:36 GMT